

Machining of Elastomers

by

Jie Luo

A dissertation submitted in partial fulfillment
of the requirements for the degree of
Doctor of Philosophy
(Mechanical Engineering)
in The University of Michigan
2005

Doctoral Committee:

Associate Professor Albert J. Shih, Chair
Professor Shixin Jack Hu
Associate Professor David Martin
Assistant Professor Kevin Pipe

© Jie Luo
All Rights Reserved

2005

DEDICATION

To My Parents

ACKNOWLEDGEMENTS

I sincerely appreciate my advisor, Professor Albert Shih, for giving me the opportunity to explore this topic. I have learned and improved a lot with your encouragement, insightful advices, and guidance in last three years. Your suggestions, effort, time, and energy help me develop the ideas that made the research a success.

I would like to take this opportunity to thank my advisory committee members, Professor S. Jack Hu, Professor David Martin, and Professor Kevin Pipe for your guidance and help.

I thank Mark Lewis for his previous research work that helped shape the direction of this project. I am very grateful to Jeffrey Gapczynski at DaimlerChrysler Co. and Marquis Alfonso at Siemens for their technical help in my research.

I would also like to thank my parents as well as my sister and her family for their unfailing support and encouragement.

I would love to say thanks to my research colleges Hongtao Ding, Steve White, Scott Miller, Zhenhua Huang, and Rui Li for their help and suggestions. I thank my friends Jun Qu, Jian Kong, Chen-Chun Kao, and Qingqing Chen for the good time we have shared.

I would also like to thank the sponsors of this research, the National Science Foundation and Michelin Americas R&D Corp.

TABLE OF CONTENTS

DEDICATION	ii
ACKNOWLEDGEMENTS	iii
LIST OF TABLES	vii
LIST OF FIGURES	viii
LIST OF SYMBOLS	xi
ABSTRACT	xiv
CHAPTER 1. INTRODUCTION	1
1.1 Background of elastomers.....	1
1.2. Overview of methods for machining elastomers.....	2
1.2.1. Sharp tool machining of elastomers.....	2
1.2.2. Cryogenic machining of elastomers.....	3
1.2.3. Induction-heated tool machining of elastomers.....	4
1.3. Potential applications of machining of elastomers.....	4
1.3.1. Tire tread pattern milling.....	5
1.3.2 Tire rubber recycling.....	5
1.3.3. Footwear, vibration damper, and other elastomer products.....	5
1.4. Research issues.....	6
1.4.1. Chip formation.....	6
1.4.2. Inverse heat transfer solution of induction heating.....	6
1.4.3. Induction-heated tool for elastomer machining.....	6
1.4.4. Chip morphology, cutting forces, and machined surfaces in induction-heated tool machining of elastomers.....	7
1.4.5. Future work.....	7
References.....	8
CHAPTER 2. CHIP FORMATION	12
2.1 Introduction.....	12
2.2. Experiment.....	13
2.3. Chip size.....	15
2.4. Elastomer Chip Classification procedure.....	16
2.5. Seven types of elastomer Chips.....	16
2.6. Effects of groove cleanliness, spindle speed, and feed speed.....	18
2.7. Conclusions.....	19
References.....	20
CHAPTER 3. INVERSE HEAT TRANSFER SOLUTION OF INDUCTION HEATING	29

3.1. Induction heating	29
3.2. Mathematical modeling	31
3.2.1. Effect of the Biot number	31
3.2.2. Finite difference modeling of the workpiece with low cross-section Biot number	32
3.2.3. Inverse heat transfer modeling.....	35
3.3. Experiment.....	36
3.4. Results.....	37
3.4.1. Experimental temperature measurements	37
3.4.2. Calculated heat flux and finite difference modeling results	38
3.4.3. Comparison of experimental and modeling results	39
3.4.4. Measurement error analysis	40
3.5. Sensitivity analysis.....	41
3.5.1. Sensitivity to grid spacing.....	41
3.5.2. Sensitivity to thermocouple location	41
3.5.3. Sensitivity to thermophysical properties.....	42
3.6. Finite element verification	42
3.7. Conclusions.....	44
References.....	46
CHAPTER 4. DIFFERENCE THERMAL MODELING AND EXPERIMENTAL VALIDATION OF INDUCTION- HEATED TOOL	55
4.1. Introduction.....	55
4.2. Experimental setup and test procedure	56
4.2.1. Experiment A	56
4.2.2. Experiment B	57
4.2.3. Experiment C	58
4.3. Results of tool induction heating experiments.....	59
4.3.1. Results of Experiment A - calibration of contact thermocouple.....	59
4.3.2. Results of Experiment B - effect of tool rotation.....	59
4.3.3. Results of Experiment C – induction heating of a stationary tool	60
4.4. Finite difference thermal modeling of an induction-heated tool	61
4.4.1. Finite difference thermal model.....	61
4.4.2. Modeling results of the stationary tool	64
4.4.3. Comparison of the experimental and modeling results.....	65
4.5. Conclusions.....	67
References.....	68
CHAPTER 5. CHIP MORPHOLOGY, CUTTING FORCES, AND MACHINED SURFACES IN INDUCTION-HEATED TOOL MACHINING OF ELASTOMERS	75
5.1. Introduction.....	75
5.2. Experimental setup, test procedure, and data analysis.....	77
5.2.1. Machine setup	77
5.2.2. Experimental design.....	78

5.2.3. Surface inspection.....	78
5.2.4. Force analysis.....	79
5.3. Chip size and morphology	80
5.4. Cutting forces.....	81
5.5. Machined grooves.....	83
5.6. Machined surfaces	85
5.6.1. Distance between machining marks.....	85
5.6.2. Surface roughness	86
5.7. Conclusions.....	88
References.....	90
CHAPTER 6. CONCLUSIONS AND FUTURE WORK	103
6.1. Conclusions.....	103
6.2. Future works	105

LIST OF TABLES

Table 1.1. Comparison of the properties of elastomer and other materials [2–4].....	9
Table 1.2. Characteristics and applications of five commercial elastomers [8,9].	9
Table 2.1. Summary of seven end milling experiments.....	22
Table 2.2. Peripheral cutting speed and feed in Experiments I – VII.	22
Table 2.3. Peripheral speed of various end mills and corresponding maximum uncut chip thickness.....	22
Table 3.1. Measured peak temperature T_{peak} and corresponding time t_{peak} of thermocouple 1.....	48
Table 3.2. Calculated induction heat flux q''_{ind} (MW/m ²).....	48
Table 3.3. Influence of the uncertainties of B and ϵ on the heat flux q''_{ind} (MW/m ²)	48
Table 3.4. Comparison of finite difference nodal temperature and the finite element analyzed average temperature of the cross-section.....	49
Table 4.1. Process parameters for Experiment B.....	69
Table 5.1. Tool and workpiece temperatures in four end milling experiments.	92
Table 5.2. Peak frequency of F_y in elastomer end milling experiments.....	92
Table 5.3. Surface roughness R_a measured by the stylus and confocal microscopy.	92

LIST OF FIGURES

Fig. 1.1. Results of the preliminary elastomer end milling test that failed to make a clear-cut groove on an elastomer workpiece with steel cable reinforcement: (a) side view, and (b) front view.....	10
Fig. 1.2. An example of the mold used for tire tread pattern molding.....	10
Fig. 1.3. Up-, down-, and mixed-cut end mills: (a) down-cut end mill, (b) up-cut end mill, (c) mixed-cut end mill, (d) down-cut end milling setup, (e) up-cut end milling setup, and (f) mixed-cut end milling setup.....	10
Fig. 1.4. Examples of milled groove condition levels for an elastomer workpiece. (Level A: Clear groove; level B: Clear groove with residual burrs on the surface; Level C: Thin layer of elastomer on surface covering clear groove; Level D: Clogged groove).....	11
Fig. 1.5. Two new concepts for elastomer machining: (a) induction-heated tool machining of elastomers, and (b) machining of cryogenically cooled elastomers.....	11
Fig. 1.6. 1 kW radio-frequency induction heating power supply and heating coil.....	11
Fig. 2.1. Optical pictures of elastomer chip machined in Experiments I and III using tools #1 to #13.....	23
Fig. 2.1. (cont.) Optical pictures of elastomer chip machined in Experiments I and III using tools #1 to #13.....	24
Fig. 2.2. The four-step procedure used to categorize chip morphology for an end milled elastomer.....	25
Fig. 2.3. SEM micrographs of adiabatic shear band in the SFE type chip machined by Tool 8 in Experiment VII, 14.8 mm/s feed speed and 4200 rpm spindle speed: (a) overview of the chip, and (b) close-up view shear band in the box in (a)....	25
Fig. 2.4. SEM micrographs: (a) a curled, serrated SCE type chip with wavy marks machined by Tool 8 in Experiment III, and (b) a SFE type of chip with the wavy serration mark on the surface.....	26
Fig. 2.5. SEM micrographs of a RF type of chip machined by Tool 8 in Experiment I..	26
Fig. 2.6. SEM micrographs of SCM type curled chip machined by Tool 11: (a) in Experiment I, and (b) in Experiment III.....	27
Fig. 2.7. SEM micrographs: (a) The RC and B types of chips machined by Tool 4 with 2.12 mm/s feed speed and 5500 rpm, and (b) chip with burned edge, machined by Tool 2 in Experiment I.....	27
Fig. 2.8. SFM chip machined by Tool 4 at 5500 rpm and 14.8 mm/s feed speed.....	28
Fig. 2.9. Optical pictures of chip formation in the four corners of the test matrix in Experiment V, Tool 6 at: (a) 2900 rpm, 2.12 mm/s feed, (b) 2900 rpm, 14.8 mm/s feed, (c) 5500 rpm, 2.12 mm/s feed, and (d) 5500 rpm, 14.8 mm/s feed. (): Cleanliness index of end milled groove.....	28

Fig. 3.1. Configuration of the induction heating a long workpiece and the cross-section represented by a node m with area A_m and perimeter P_m .	50
Fig. 3.2. Finite difference model and nodal points in a half rod.	50
Fig. 3.3. Control volume at node m and the sources of heat flux.	50
Fig. 3.4. Setup of rod workpiece, water-cooled induction heating coil, and thermocouples.	51
Fig. 3.5. Configuration of the induction heating experiment of the rod workpiece and thermocouple locations.	51
Fig. 3.6. Experimentally measured temperatures at four thermocouples for $t_h = 25$ s and the selection of data points for inverse heating transfer solution of induction heat flux.	52
Fig. 3.7. Comparison of the measured and calculated temperature for $t_h = 25$ s.	52
Fig. 3.8. Effect of grid spacing on the surface heat flux q''_{ind} .	53
Fig. 3.9. FEM mesh and the three cross-sections.	53
Fig. 3.10. Comparison of the finite element and finite difference analysis results for $t_h = 25$ s at three cross-sections.	54
Fig. 4.1. (a) Induction-heated tool machining of elastomers and (b) the double-flute down-cut end mill and titanium thermal insulator.	70
Fig. 4.2. Configuration of end mill, thermal insulator, water-cooled induction heating coil, and thermocouple.	70
Fig. 4.3. Tool tip and thermocouple locations: (a) view of tool tip with two symmetric Surfaces 1 and 2, and (b) tool tip with the cement-on thermocouple attached to Surface 1 and the position for the contact thermocouple.	71
Fig. 4.4. Setup of tool, water-cooled induction heating coil, and thermocouples in Experiment C.	71
Fig. 4.5. Configuration of the induction heating in Experiment C.	72
Fig. 4.6. Calibration for the contact thermocouple probe based on cement-on thermocouple.	72
Fig. 4.7. Effect of tool rotation on the tool temperature (25 s duration of induction heating).	73
Fig. 4.8. Comparison of the measured and calculated temperature for heating duration as 10 s.	74
Fig. 4.9. Heat exchange between adjacent nodes in the tool and thermal insulator: (a) at node m in the heating region, (b) at node m in the insulation region, and (c) at node m_s in the insulation region.	74
Fig. 5.1. (a) Experimental setup of elastomer end milling with tool induction heating, (b) fixture base and top plate with grooves, and (c) top view of the fixture with the elastomer workpiece in place.	93
Fig. 5.2. Height profile of machined surface generated in Experiment XI at 2400 rpm: (a) the original height profile, and (b) the height profile with high-frequency noises filtered.	94
Fig. 5.3. End milling force components.	94
Fig. 5.4. Optical micrographs of elastomer chips.	95
Fig. 5.5. Experiment IX (no workpiece cooling, tool heating, 1100 rpm): (a) three end milling force components vs. time, and (b) frequency domain analysis.	96

Fig. 5.6. Experiment XI (workpiece cooling, tool heating, 2400 rpm): (a) three end milling force components vs. time, and (b) frequency domain analysis.	97
Fig. 5.7. Averaged peak values of end milling forces vs. spindle speeds.	98
Fig. 5.8. Optical pictures of machined surface. (W is the groove width. the upper surface is the entry surface, and the lower side surface is the exit surface.).....	99
Fig. 5.9. Top view of the groove machined in Exp. VIII at 2400 rpm: (a) picture of the hole generated by retracting end milling tool, and (b) relative size of the tool, hole, and maximum and minimum groove width.	100
Fig. 5.10. Relationship between the groove width W and cutting force F_y	100
Fig. 5.11. SEM micrographs of machined surface. (R_a is measured by the contact stylus profilometer).	101
Fig. 5.12. Frequency domain analysis of machined elastomer surfaces.	102

LIST OF SYMBOLS

A_b	area of the cross-section in the insulation region and cooling region 1 and 2
A_m	area of the cross-section at node m
A_{ms}	area of the cross-section at node m_s in the thermal insulator
A_t	area of the cross-section in the cooling region 4
B	coefficient for calculation of convection heat flux q''_{conv}
Bi	Biot number
e_{RMS}	root mean square error
c	specific heat
c_s	specific heat of the thermal insulator
F_x	force component in X -axis
F_y	force component in Y -axis
F_z	force component in Z -axis
h	convection coefficient
k	thermal conductivity
k_s	thermal conductivity of the thermal insulator
L	half length of the workpiece (steel rod)
L_c	characteristic dimension of the workpiece
L_{cj}	width of the cooling region j of the tool
L_h	width of the heating region in finite difference modeling
L_{ins}	width of the insulation region of the tool
m	node number
m_1	number of nodes in the heating region of half length rod
m_2	number of nodes in the cooling region of half length rod
m_s	node number in the thermal insulator
N	number of measurements
n_1	number of time instants
n_2	number of thermocouples
P_b	perimeter of the cross-section in the insulation region and cooling region 1 and 2
P_m	perimeter of the cross-section at node m
P_{ms}	outer perimeter of the cross-section at node m_s in the thermal insulator
P_t	perimeter of the cross-section in the cooling region 4

p	time step
$q''_{ca,m\pm 1}$	conduction rate from adjacent node $m \pm 1$ to node m along axial direction
$q''_{ca,m_s\pm 1}$	conduction rate from adjacent node $m_s \pm 1$ to node m_s along axial direction
$q''_{cr,m}$	conduction rate from node m to adjacent node m_s along radial direction
q''_{cr,m_s}	conduction rate from node m_s to surrounding environment along radial direction
q''_{conv}	convection heat flux
q''_{ind}	surface heat flux generated by induction in the heating region
q''_{rad}	radiation heat flux
r	radius
T_c	reading of cement-on thermocouple
T_h	reading of contact thermocouple probe
T_{peak}	peak temperature
T_m^p	nodal temperature at node m and time step p
$T_{m_s}^p$	nodal temperature at node m_s and time step p
T_{sp}	initial temperature of the machine spindle
$T_{x_j}^{t_i} _{est}$	temperatures estimated by finite difference model
$T_{x_j}^{t_i} _{exp}$	experimentally measured temperatures
T_∞	ambient temperature
t	time
Δt	time increment
t_i	time instant of an experimental measurement
t_h	duration of heating
t_{peak}	instant for peak temperature
V_m	volume of the control volume at node m
V_{m_s}	volume of the control volume at node m_s
W	width of grooves machined on elastomer workpiece
w	thickness of the thermal insulator
x_j	location of thermocouple j from the origin of the axis
x_{IC}	location of the induction coil from the origin of the axis
Δx	width of the control volume
Δx_h	spacing between two adjacent nodes in the heating region
Δx_c	spacing between two adjacent nodes in the cooling region
ε	emissivity
η	perturbation

ρ	density
ρ_s	density of the thermal insulator
σ_s	Stefan-Boltzmann constant

ABSTRACT

The research investigates the use of sharp tools, cryogenic cooling of workpiece, and induction heating of the tool for machining of elastomers. The chip formation, inverse heat transfer solution of induction heating, induction-heated tool for elastomer machining, forces in end milling of elastomers, and machined grooves and surfaces are studied.

A classification system that identifies elastomer chips based on their size and morphology is described. A four-step examination procedure is developed to specify seven types of chips. Serrated chip formation with apparent adiabatic shear bands, possibly due to the low thermal conductivity of elastomer, is observed for one end milling condition. Another type of serrated chip is found with surface wavy marks due to the workpiece vibration.

The explicit finite difference formulation of an inverse heat transfer model to calculate the induction heat flux is developed for a workpiece with low cross-section Biot number. Compared to measured temperatures, the accuracy and limitation of proposed method is demonstrated. Finite element analysis results validate the assumption to use the uniform temperature in a cross-section for the inverse heat transfer solution of induction heat flux.

The induction heating is applied to raise the temperature of an end milling tool for machining of elastomers. Experiments and finite difference thermal modeling of the induction-heated tool for elastomer end milling are investigated. The thermal model of a stationary tool can be expanded to predict the temperature distribution of an induction-heated rotary tool within a specific spindle speed range. Experimental measurements validate that the thermal model can accurately predict tool tip peak temperature.

The induction-heated tool and cryogenically cooled workpiece are investigated for elastomer end milling to generate desirable shape and surface roughness. At high

cutting speed, smoke is generated and becomes an environmental hazard. At the low cutting speed, induction-heated tool demonstrates to be beneficial for the precision elastomer machining with better surface roughness and dimensional control. Frequency analysis of cutting forces shows that the low frequency vibration of soft elastomer workpiece is correlated to the surface machining mark generation. The correlation between the machined groove width and cutting force reveals the importance of the workpiece compliance to precision machining of elastomer. The use of both contact profilometer and non-contact confocal microscope to measure the roughness of machined elastomer surfaces is explored. The comparison of measurement results shows the advantages and limitations of both measurement methods.

CHAPTER 1.

INTRODUCTION

1.1 Background of elastomers

Elastomers, also known as rubbers, are the long-chain polymers that exhibit many unique material properties. According to ASTM D 1566-00 [1], rubber is a material that is capable of recovering from large deformations quickly and forcibly, and can be, or already is, modified to a state in which it is essentially insoluble (but can swell) in boiling solvent. Elastomer materials are a popular choice for shock and vibration absorption, sealing, flexible and stretchable uses, and electrical and thermal insulation. Table 1.1 illustrates the unique mechanical and thermal properties of elastomers, compared to other engineering materials.

Elastomers have very low thermal conductivity. Under cyclic loading, elastomers exhibit significant hysteresis, which contributes to their energy absorption capability. Elastomers also have a very low elastic modulus and high percentage of elongation before fracture, which makes the machining of elastomers a challenge. A milling test was conducted to understand these difficulties. In this test, a 4.76 mm diameter high-speed steel double-flute end mill was used to cut a groove in an elastomer tire segment with the spindle speed of 3600 rpm (53.8 m/min peripheral cutting speed), feed speed of 0.42 mm/s (3.5 $\mu\text{m}/\text{flute}$ feed), and depth of cut of 6.35 mm at room temperature. Fig. 1.1 shows the elastomer workpiece with several machined grooves. As shown in this figure, the resulting machined surface is very rough with burr-type debris attached to the workpiece.

Most elastomer parts are manufactured using the molding rather than machining process. In the molding process, raw polymeric materials are mixed with other additives and then heated, melted, and pressed into a mold. Inside the mold, the polymer material

is subjected to a controlled temperature-pressure-time cycle. The material is cured, vulcanized, and cooled to produce the desired properties and geometry. To manufacture elastomer parts with complicated shapes, such as tire and footwear tread patterns, a set of molds must first be produced.

Manufacturing these molds is expensive and time-consuming. An example of the mold for a car tire is shown in Fig. 1.2. Molds for elastomers are usually made of aluminum or steel because they need to have an intricate shape and must subject to repetitive temperature and pressure cycles during the molding process. These molds are usually expensive and time-consuming to manufacture. For example, it costs about \$50,000 to \$80,000 to make a set of car tire molds and takes over 4 weeks. There are some recent advancements in rapid mold manufacturing technologies, such as the high-speed CNC milling of hardened tool steels, 3D layer printing and sintering, and fast graphite electrode machining for die sinking EDM, etc. However, for the size, strength, and precision required for the tire tread mold, these methods are still not technologically or economically feasible. For these reasons, machining offers an attractive alternative for manufacturing custom or prototype elastomer components.

1.2. Overview of methods for machining elastomers

To enable the effectively machining of elastomers, three new methods of end milling of elastomers are studied. The first method uses the sharp, down-cut wood working tool to machine elastomers at room temperature. The second method cryogenically cools the elastomer with solid carbon dioxide (dry ice) to $-78.6\text{ }^{\circ}\text{C}$ before machining. The third method applies induction heating to raise the tool temperature and machine elastomers with the heated tool. These three methods are introduced in following sections.

1.2.1. Sharp tool machining of elastomers

For elastomers, the stress-strain curves are usually nonlinear and can exhibit a large range of strain, such as 600%, before fracture. The stress-strain curves are also sensitive to the strain-rate. High speed machining increases the strain-rate in the deformation zones, reduces the average chip thickness, and enables more efficient and

precise machining of elastomers. This has been illustrated by the most notable elastomer machining research which was conducted by Jin and Murakawa [5]. They used several carbide end mills of various sizes and helix angles to cut grooves on three types of elastomers, H-NBR, Norbornone rubber, and silicone rubber, at various speeds. Better surface finishes and lower forces were observed for machining at high speeds with high helix angle cutters.

An end milling of elastomers using sharp woodworking router bits was studied by Shih et al. [6]. Such sharp tools are very different from conventional metal working tools, which commonly have the small rake angle and clearance angle to withstand high cutting forces. High rake angle tools are commonly used in the woodworking industry. End mills in the metalworking industry are called router tools in the woodworking industry. A set of 13 different tools with various diameters, materials, number of flutes, and up- and down-cutting configurations, as defined in Figs. 1.3(a), 1.3(b), 1.3(d), and 1.3(e), were tested on room temperature and solid carbon dioxide cooled elastomers. The surface appearance and cleanliness of the milled cut was recorded using an optical camera with close-up lens and then categorized into four levels as shown in Fig. 1.4. It was found that the sharp, down-cut tool configuration and stiffness of the elastomer workpiece are the two most important variables that influence the effectiveness in end milling to remove elastomer work-material and generate a clean groove. With proper selection of end mill geometry, process parameters, and fixture stiffness, clean grooves can be machined on the elastomer workpiece. It is also confirmed that higher spindle speed is beneficial for machining a clean groove in elastomers.

1.2.2. Cryogenic machining of elastomers

Both the low elastic modulus and high elongation of elastomers, as shown in Table 1.1, make the elastomer machining difficult. At low temperature, however, the elastic modulus increases, the elongation (to fracture) decreases, and elastomers transform to a brittle, glassy phase. This can make the machining process more efficient.

The configuration of the cryogenic elastomer machining method is illustrated in Fig. 1.5(b). The elastomer workpiece is clamped on an insulated container filled with either solid carbon dioxide (dry ice) or, possibly, liquid nitrogen. The temperature of dry

ice is about -78.5°C and liquid nitrogen is about -196°C . At the steady-state heat transfer condition, the temperature on the outside surface of the elastomer workpiece will reach a specific level, which is dependent on the thermal conductivity, k , and thickness, t , of the elastomer material and thermal convection coefficient, h , of the surrounding air.

To recycle rubber tires into pellets for further processing, White [7] showed that grinding elastomers at cryogenic conditions helped reduce the pellet size and improve surface finish. The investigation conducted by Shih et al. [6] shows that cryogenic cooling of the elastomer workpiece can help enhance the performance of end mills that do not perform well on machining room temperature elastomer workpiece.

1.2.3. Induction-heated tool machining of elastomers

Another method, induction-heated tool machining of elastomers, is shown in Fig. 1.5(a). This idea originates from the current practice of manually carving of the tire tread. A resistance-heated, sharp grooving tool is used for this operation. Heating the tool is critical. If the tool is not heated to a certain temperature, the carver won't be able to cut grooves on the tire. The heat softens the elastomer materials ahead of the tool and allows the tool to efficiently penetrating into the workpiece.

As shown in Fig. 1.5(a), the non-contact induction heating is applied to provide a fast, consistent heat source at a precise location on the machine tool. A 1 kW radio-frequency induction heating power supply and coil, as shown in Fig. 1.6, is used in this research. The power supply generates alternating current through the water-cooled coil, which generates a magnetic field. When the milling tool is placed in the coil and enters the magnetic field, eddy currents are induced on the tool surface. The alternating eddy currents generate localized heat without the physical contact between the coil and workpiece.

1.3. Potential applications of machining of elastomers

Table 1.2 lists five major commercial elastomer materials and their applications. Elastomers are used for tire, shoe, hose, film, wire, cable, dampers, etc. Among all these possible applications, this research targets the following potential applications.

1.3.1. Tire tread pattern milling

As discussed in the previous section, the manufacture of tire molds is usually expensive and time-consuming. For tire manufacturers, the need to produce just a few tires for test and performance evaluation or for the specialty market is carried out by manually carving the tire tread pattern with sharp, heated blade grooving tools. The job requires some physical strength and is usually labor intensive. The new elastomer machining methods could lead to a process using a CNC machine to mill tire tread patterns. It would replace manual carving and help reduce the cost and throughput-time in prototype tire tread manufacturing. In auto racing, the manual carving of tire tread has been used to alter the tire performance for different weather and track conditions. Clayton [10] has proposed an apparatus for tire tread milling. However, due to the lack of a feasible elastomer machining process, this concept has not been implemented. The new elastomer machining can be used not only for prototype and racing tire but also for small-batch and customized tire tread pattern generation, which could be a new business opportunity for tire manufacturers.

1.3.2 Tire rubber recycling

Technologies developed can also be applied for recycling the tire rubber, which is a thermosetting polymer. By cooling the tire to liquid nitrogen temperatures, the tire elastomer material does not get damaged; however, the bond between the elastomer and steel cable in the tire is weakened considerably. Such de-bonding characteristics have been used in cryogenic tire recycling [7] to separate the steel and rubber using a magnet. The cryogenic machining of elastomers can be applied to investigate the chip formation and the mechanics of generating small and consistently sized rubber pellets for tire recycling. Recycled tire rubber pellets can be blended with tar to make rubberized asphalt for more durable road pavements. A small percentage, about 5 to 10%, of the recycled rubber pellets can be mixed with virgin rubber to make new tires.

1.3.3. Footwear, vibration damper, and other elastomer products

The footwear industry also uses elastomer materials extensively. Similar to the tire, small-batch, custom-made footwear products are not popular due to the high cost and

long lead-time to fabricate the molds. The elastomer machining methods may facilitate and promote a niche market in customized footwear products. Other potential applications of elastomer machining include customized vibration isolators, dampers, couplings, golf grips, etc. In summary, molds with very simple geometry will be used to make blank elastomer parts for the subsequent machining operation to generate the intricate shape.

1.4. Research issues

The objective of this dissertation is to investigate the machining methods for elastomers. Following research issues are studied in this dissertation.

1.4.1. Chip formation

Chip formation is investigated in Chapter 2. Various chips are generated in the end milling of elastomers. A classification system that identifies elastomer chips based on their size and morphology is described. Optical pictures and Scanning Electron Microscopy (SEM) micrographs were used to examine and classify chips. A examination procedure is developed to specify chips.

1.4.2. Inverse heat transfer solution of induction heating

Chapter 3 develops a method to experimentally determine the heat generation and transfer in an induction-heated workpiece. The explicit finite difference formulation of an inverse heat transfer model to calculate the heat flux generated by induction is developed. The experimentally measured temperature data is used as the input for the inverse heat transfer model. This model is particularly suitable for a workpiece with low cross-section Biot number. The accuracy and limitation of proposed method is demonstrated.

1.4.3. Induction-heated tool for elastomer machining

Experiments and finite difference thermal modeling of the induction-heated tool for end milling of elastomers are investigated in Chapter 4. Three sets of experiments, designed to calibrate the contact thermocouple for the tool tip temperature measurement,

study the effect of tool rotational speed on induction heat generation and convective heat transfer, and measure the tool temperature distribution for finite difference inverse heat transfer solution and validation of modeling results, are conducted. The complete finite difference thermal model of the tool and insulator is developed to predict the distribution of tool temperature.

1.4.4. Chip morphology, cutting forces, and machined surfaces in induction-heated tool machining of elastomers

The induction-heated tool and cryogenically cooled workpiece are investigated for end milling of elastomers to generate desirable shape and surface roughness. Elastomer end milling experiments are conducted to study effects of the cutting speed, tool heating, and workpiece cooling on the chip formation, cutting forces, groove width, and surface roughness. The use of both contact profilometer and non-contact confocal microscope to measure the roughness of machined elastomer surfaces is also explored.

1.4.5. Future work

The future work of this research in four areas is described in Chapter 6.

References

- [1] ASTM D1566-00, 2000, *Standard Terminology Relating to Rubber*, American Society for Testing of Materials.
- [2] Harper, C. (Ed.), 1975, *Handbook of Plastics and Elastomers*, McGraw-Hill.
- [3] Gere, J. M., and Timoshenko, S. P., 1997, *Mechanics of Materials*, 4th Ed., PWS Pub.
- [4] Incopera, F. P., and DeWitt, D. P., 1996, *Fundamentals of Heat and Mass Transfer*, 4th Ed., Wiley.
- [5] Jin, M., and Murakawa, M., 1998, "High-Speed Milling of Rubber (1st Report) - Fundamental Experiments and Considerations for Improvement of Work Accuracy," *Journal of the Japan Society for Precision Engineering*, Vol. 64, No. 6, pp. 897-901.
- [6] Shih, A. J., Lewis, M. A., and Strenkowski, J. S., 2004, "End Milling of Elastomers – Fixture Design and Tool Effectiveness for Material Removal," *ASME Journal of Manufacturing Science and Engineering*, Vol. 126, No. 1, pp. 115-123.
- [7] White, L., 1995, "Recycling Rubber- Technologies Add Value to Scrap," *European Rubber Journal*, Vol. 177, No. 2, pp. 24-25.
- [8] Callister, C., 1997, *Materials Science and Engineering*, 4th Ed., Wiley.
- [9] Haper, C. (Ed.), 1975, *Handbook of Plastics and Elastomers*, McGraw-Hill.
- [10] Clayton, A. R., 1982, *Tire Tread Grooving Apparatus and Method*, US Patent No. 4,311,182.

Table 1.1. Comparison of the properties of elastomer and other materials [2–4].

Material	Elastic modulus (GPa)	Poisson's ratio	Ultimate stress (MPa)	% of elongation to fracture	Thermal conductivity (W/m K)
Elastomers	0.0007 – 0.004	0.47 – 0.5	7 – 20	100 – 800	0.13 – 0.16
Aluminum alloys	70 – 79	0.33	100 – 550	1 – 45	177 – 237
Steel, high-strength	190 – 210	0.27 – 0.3	550 – 1200	5 – 25	35 – 60
Titanium alloys	100 – 120	0.33	900 – 1200	10	7 – 7.5
Plastic, Nylon	2.1 – 3.4	0.4	40 – 80	20 – 100	0.3
Plastic, Polyethylene	0.7 – 1.4	0.4	7 – 28	15 – 300	0.4

Table 1.2. Characteristics and applications of five commercial elastomers [8,9].

Chemical type	Trade name	Elongation (%)	Major Characteristics	Typical Applications
Natural polyisoprene	Natural rubber (NR)	500—760	Excellent physical properties; good resistance to cutting, gouging, and abrasion; low heat, ozone, and oil resistance; good electrical insulator	Pneumatic tires and tubes; heels and soles; gaskets
Styrene – butadiene copolymer	GRS, Buna S (SBR)	450—500	Good physical properties; excellent abrasion resistance; not oil, ozone, or weather resistant	Same as natural rubber
Acrylonitrile – butadiene copolymer	Buna A, Nitrile (NBR)	400—600	Excellent resistance to vegetable, animal, and petroleum oils; poor low-temperature properties	Gasoline, chemical, and oil hose; seals and O-rings, heels and soles
Chloroprene	Neoprene (CR)	100—800	Excellent ozone, heat, oil, and weathering, flame resistance	Wire, cable, belts, hoses, seals, chemical tank linings, and gaskets
Polysiloxane	Silicone (VMQ)	100—800	Excellent resistance to high and low temperatures; low strength, excellent electrical insulator	High- and low-temperature insulation; seals; diaphragms; tubing for food and medical uses

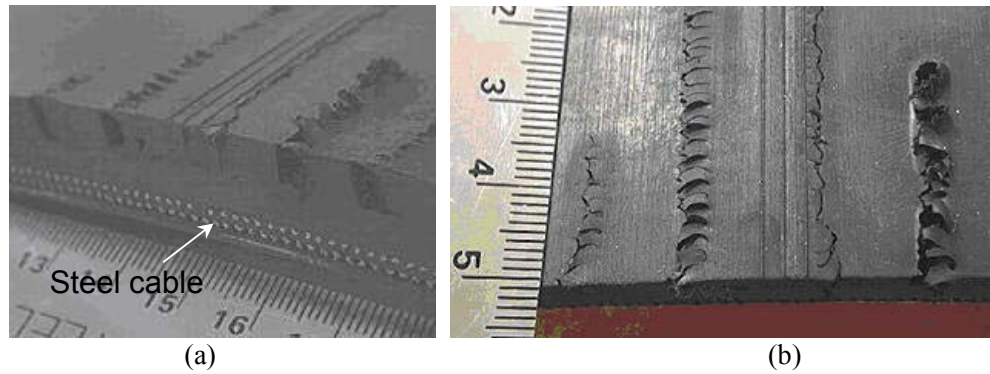


Fig. 1.1. Results of the preliminary elastomer end milling test that failed to make a clear-cut groove on an elastomer workpiece with steel cable reinforcement: (a) side view, and (b) front view.



Fig. 1.2. An example of the mold used for tire tread pattern molding.

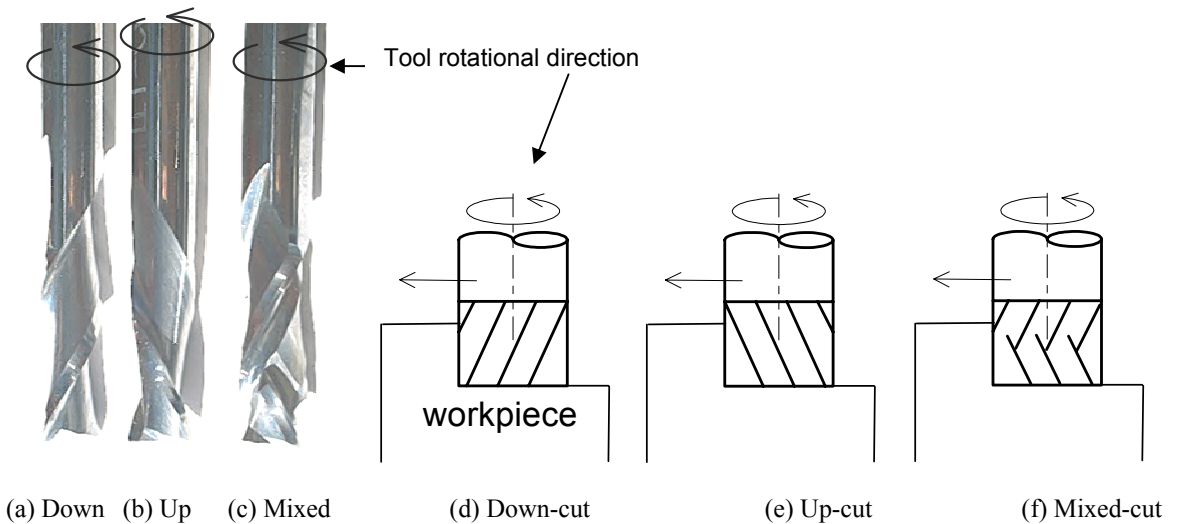


Fig. 1.3. Up-, down-, and mixed-cut end mills: (a) down-cut end mill, (b) up-cut end mill, (c) mixed-cut end mill, (d) down-cut end milling setup, (e) up-cut end milling setup, and (f) mixed-cut end milling setup.

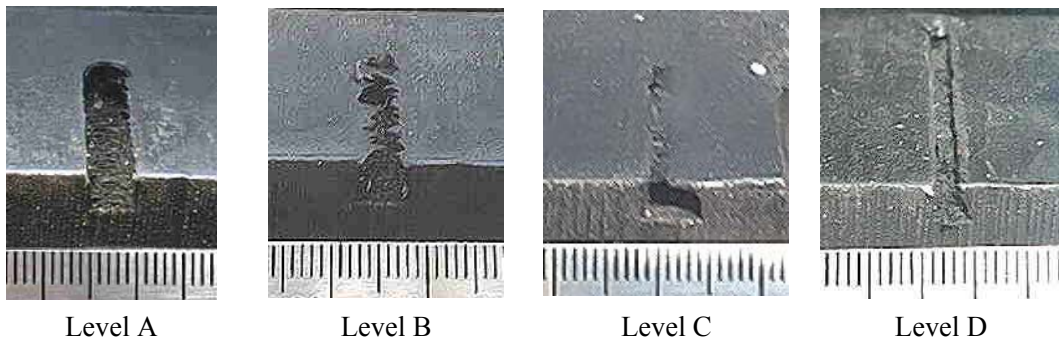


Fig. 1.4. Examples of milled groove condition levels for an elastomer workpiece. (Level A: Clear groove; level B: Clear groove with residual burrs on the surface; Level C: Thin layer of elastomer on surface covering clear groove; Level D: Clogged groove)

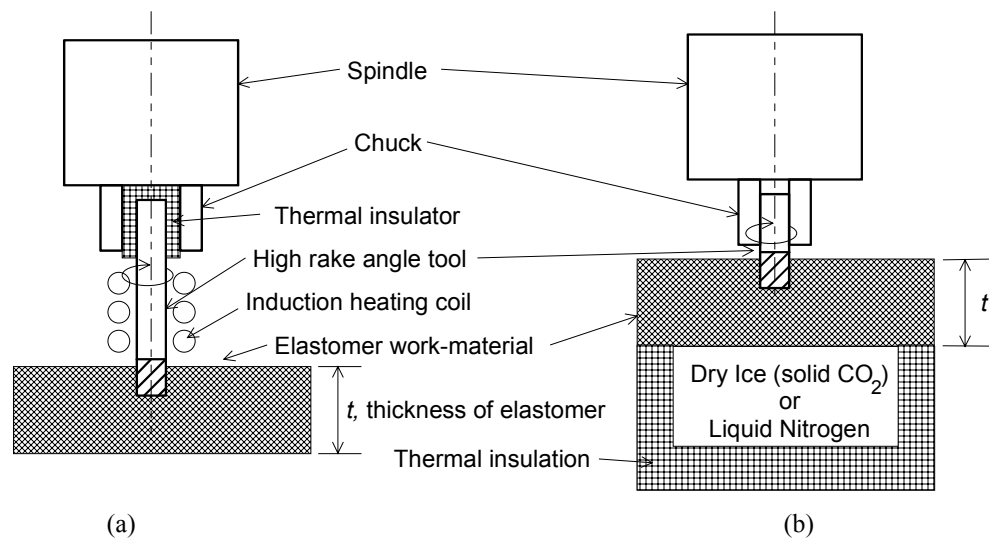


Fig. 1.5. Two new concepts for elastomer machining: (a) induction-heated tool machining of elastomers, and (b) machining of cryogenically cooled elastomers.



Fig. 1.6. 1 kW radio-frequency induction heating power supply and heating coil.

CHAPTER 2.

CHIP FORMATION

2.1 Introduction

Machining is a chip generation process, in which the unwanted work-material is removed by a tool to become chip. Chip formation processes in metal cutting, particularly in turning and drilling, have been studied extensively [1–10]. Elbestawi, et al. [11], Ng, et al., [12], and Becze, et al. [13] have investigated chip formation and tool wear in high speed end milling of hardened steels. Ning, et al. [14] have classified the chips observed from ball end milling of H13 hardened steel into four types: complete, unstable, critical, and severe chips. Kobayahsi [15] have discussed the mechanics and chip morphology in turning and drilling of plastics. The unique mechanical properties of elastomers, particularly the large elongation to fracture and low thermal conductivity, can greatly affect the chip formation during machining.

In general, chip formation in machining can be categorized as forming continuous, discontinuous, or serrated chips [9,10]. The serrated chip with accompanying adiabatic shear band is commonly observed in machining materials that exhibit poor thermal properties with either low thermal conductivity or low specific heat. For materials with such poor thermal properties, the heat generated in the shear zone does not have time to escape. This raises the temperature in the shear zone and leads to thermal softening and adiabatic shear band formation. Titanium is an example material that exhibits such thermal characteristics. The thermal conductivity of titanium alloys is low, about 7 W/mK, as compared to that of 35–40 W/mK for steels. The adiabatic shear band formation occurs in machining of titanium alloys under a wide range of cutting conditions [7–10, 16–20].

Elastomers have even lower thermal conductivity, about 0.15 W/mK, than titanium and may also promote adiabatic shear band formation in a chip. Furthermore, the low modulus of elasticity and low stiffness of an elastomer can trigger workpiece vibration during end milling and create wavy serration marks on the chip surface.

Most elastomer parts are manufactured using the molding process. The machining process is studied for the low-volume, prototype manufacturing of elastomer parts to avoid making the mold with complicated shape. In this chapter, the chip formation is reported for several elastomer end milling experiments. Optical pictures and SEM micrographs of various elastomer chips are presented and a classification procedure, based on chip size and morphology, is introduced and applied.

2.2. Experiment

Seven sets of elastomer milling tests were conducted on a HAAS VF1 CNC vertical machining center by Shih et al. [21]. All machining tests were conducted dry without any coolant. The depth of cut was set at 3.81 mm for all end milling tests. The material is a blend of KM rubber, which is a mixture of synthetic and natural elastomers for tire tread applications, and is provided prepared by Michelin.

Thirteen end mills, which are woodworking router bits manufactured by Onsrud Cutter LP, were studied. These tools, denoted as Tool 1 to 13, represent a wide range of sizes (3.18, 6.35, and 12.7 mm diameter), tool materials (high speed steel and carbide), cutting directions (up-cut and down-cut), number of flutes (single and double-flute), and cutting edge geometry. Detailed basic tool parameters have been documented in Ref. [21].

Several of these thirteen end mills are belong to three series. Tools in a series have the same basic geometry but different diameters. The tools in each series are as follows:

Series 1: Tools 1 (3.18 mm) and 6 (6.35 mm)

Series 2: Tools 2 (3.18 mm), 4 (6.35 mm), and 12 (12.7 mm)

Series 3: Tools 7 (6.35 mm) and 13 (12.7 mm)

where the number in parentheses represents the tool diameter. The performance of each series of tools was compared to provide insight into elastomer machining based upon basic tool geometry within each series.

Seven sets of milling experiments were conducted. The process parameters of these experiments are summarized in Table 2.1. Table 2.2 summarizes the peripheral cutting speeds and feeds for tests conducted in Experiments I–VII. In Experiment I, thirteen end mills were used to machine a groove in an elastomer workpiece at room temperature. Experiments II and III were conducted under identical conditions, but under reduced temperature conditions. Based on favorable milled groove surfaces achieved in Experiment I for Tool 6 (a double-flute, down-cut, carbide end mill), twelve additional tests were conducted with this tool for three rotational speeds (2900, 4200, and 5500 rpm) and four feed speeds (2.12, 6.35, 10.6, and 14.8 mm/s) as Experiment IV. In Experiment V, the same additional twelve tests were conducted with an elastomer temperature of -78.6°C (solid carbon dioxide cooled). Two final series of tests were conducted with an up-cut tool (Tool 8) for a room temperature and solid carbon dioxide cooled elastomer. The same end milling conditions as in Experiment IV and V were repeated in Experiments VI and VII using a double-flute, up-cut, carbide end mill (Tool 8). Additional experiments were conducted using Tool 4 with the same end milling conditions as in Experiments VI and VII. For each test, cleanliness of the machined groove was recorded, and elastomer chips were collected and analyzed.

The elastomer chips were black in color and did not reflect light. This characteristic hindered the ability to generate high quality optical camera or microscope pictures. However, light reflection is not a requirement for good imaging with a SEM, which can also achieve high magnification and reveal detailed features of an elastomer chip. Some elastomer chips were large (5 mm+). SEM has a limitation on the lowest level of magnification. It is difficult to get an overall evaluation of the morphology for a large size chip. Therefore, in this study, a digital camera with close-up lens was used in cooperation with a Hitachi S-4700 SEM, which can achieve a low 25X magnification.

2.3. Chip size

The elastomer chips generated in Experiments I–VII were collected and examined. Diameters of end mills used in the test are 3.18, 6.35, and 12.7 mm. The half-circle uncut chips are 4.99, 9.97, 19.9 mm long for end milling with 3.18, 6.35, and 12.7 mm diameter tools, respectively. However, the actual size of most of the observed chips was much smaller, which indicates that chip breakage occurs frequently during end milling of elastomers. The tool peripheral speed and maximum uncut chip thickness for a double-flute end mill are shown in Table 2.3. These data will be used later as a reference to understand chip size and the chip formation process.

Optical pictures of elastomer chips as machined by Tools 1 to 13 in Experiments I and III are shown in Fig. 2.1. The distance between two adjacent marks on the scale shown in this figure is 1 mm. The chips are categorized by both size and morphology. First, as shown in Fig. 2.1, the chips are classified into five size categories: 1) 1–2 mm, 2) 2–3 mm, 3) 3–4 mm, 4) 4–5 mm, and 5) 5+ mm. Note that various sizes of chip can be generated in one end-milling test. For example, the 1–2 and 3–4 mm chips are generated by Tool 1 in Experiment I. In contrast, some end milling conditions generate small, powder-like elastomer chip, such as Tool 2 in Experiment I. For some applications such as cutting scrap tires to produce recycled crumb rubber, these chips are preferred. Other end milling tests, such as Tools 8 and 9 in Experiment III, generated large-sized chips. The length of an uncut chip as cut by the 6.35 mm diameter Tool 8 was 9.97 mm. The 7 mm chip length generated by Tool 8 in Experiment III indicates that, compared to metal cutting, significant elastic recovery occurs during elastomer chip formation processes. The two large diameter tools (12 and 13) did not generate very large-sized chips as expected.

The end milling tests of Experiments I and III were conducted at the same 12.7 mm/s feed speed and 4200 rpm. As compared to the large chip generated by Tool 8 in Experiment III, frequent chip breakage must occur during the elastomer end milling. In general, it was found that cooling the elastomer workpiece to cryogenic conditions (Experiment III) created slightly larger chip sizes. The cutting edge geometry of router tools for wood machining is complicated. Based on results in Fig. 2.1, it is difficult to find a correlation between the effect of tool geometry and chip morphology.

2.4. Elastomer Chip Classification procedure

Different chip shapes were observed, as shown in Fig. 2.1. Some chips are curled, and others are flat. Some chips have serration marks on the surface, and others have a smooth surface. Some chips are small and cannot be examined clearly using an optical camera with close-up lens. The combination of optical pictures and SEM micrographs were used to classify the chip morphology using the following four-step procedure:

Step 1. Examine if the chip has been burned or melted.

Step 2. Observe if the chip has rough or straight edges in the cutting direction.

Step 3. Inspect if the chip is curled.

Step 4. Look for the serration marks on chip surface.

The procedure is illustrated in Fig. 2.2. Based on these four steps, the chips can be categorized into seven different types: B, RC, RF, SCE, SCM, SFE, and SFM. The types of chip generated in Experiments I and III are indicated in pictures in Fig. 2.1. It is possible that two or three types of chip can be generated for the same cutting condition. For example, both B and RC chip types were observed as generated by Tool 1 in Experiment I.

2.5. Seven types of elastomer Chips

The more detailed view of these seven types of chip morphology can be obtained with a SEM. SEM micrographs and discussions of the seven types of chips are summarized in the following:

- *SFE chip*: An adiabatic shear band shown in Fig. 2.3 was observed for Experiment VII at 4200 rpm and 14.8 mm/s feed speed using Tool 8 for end milling a solid carbon dioxide cooled elastomer. A detailed view of the chip surface and the adiabatic shear bands are shown in Fig. 2.3(b). The spacing between two adjacent shear bands is about 0.4 mm. The shear band shown in Fig. 2.3(b) is very narrow,

- about 10 μm wide. The low thermal conductivity of the elastomer is likely the cause for shear band formation. Among all 87 tests conducted, this is the only one that exhibits adiabatic shear band formation. The end milling conditions for inception of such adiabatic shear bands is not clear. This test is on the edge of an experiment matrix with four feed speeds and three spindle speeds [21]. End milling with the same feed speed but higher (5500 rpm) and lower (2900 rpm) spindle speeds did not generate any chips with similar adiabatic shear bands.
- *SCE chip*: A curled and serrated chip with wavy serration marks on the surface was observed for some chips as machined by Tool 8 in Experiment III. The optical picture in Fig. 1 also reveals serration marks on the surface. SEM micrographs in Fig. 2.4(a) show the wavy form on a curled SCE chip. These wavy marks were most likely created by vibration of the elastomer workpiece during machining. Although elastomers are known for their good vibration damping capability, the force created during end milling can still cause the workpiece to vibrate and generate the wavy marks observed on the chip surface. Both the flat SFE and curled SCE chips were observed in this test (Tool 8, Exp. III). Figure 2.4(b) shows the SEM micrograph of a flat SFE chip with wavy marks on the surface.
 - *RF chip*: Fig. 2.5 shows a sample RF chip with a rough edge and flat surface as generated by Tool 6 in Experiment I (room temperature). Edges along the cutting direction are not straight in the RF type chip.
 - *SCM and RC chip*: These represent are two other types of curled chips in addition to the SCE chip shown in Fig. 2.4(a). Figures 2.6(a) and 2.6(b) show the SCM chips machined by Tool 11 in Experiments I and III. Both chips have smooth surfaces and straight edges in the cutting direction. The RC type of curled chip, as shown in Fig. 2.7(a), was machined by Tool 4 with 2.12 mm/s feed speed and 5500 rpm. This was not one of the standard tests in Experiments I–VII. This chip has rough edges on all sides. Some of type B burned chips can also be seen in Fig. 2.7(a).
 - *B chip*: Smoke could be observed during some of these end milling tests. This indicates that heat generated during end milling was sufficiently high to burn and melt the elastomer material. At high temperature and atmospheric pressure, an elastomer sublimates to a gaseous phase. The gasification of an elastomer could

- leave a burned surface or edge on the residual chip that did not get totally burned. Figures 2.7(a) and 2.7(b) shows SEM micrographs of a burned chip. As shown in Fig. 2.7(a), a burned chip can be small, less than 100 μm , and lumped together. As shown in Fig 2.7(b), edge burning on a chip was also observed.
- *SFM chip*: As shown in Fig. 2.8, the SFM type of chip which has a straight edge in the cutting direction and a flat and smooth surface was observed at 5500 rpm and 14.8 mm/s feed speed using Tool 4 for end milling a solid carbon dioxide cooled elastomer.

2.6. Effects of groove cleanliness, spindle speed, and feed speed

Inside the parenthesis for each picture in Fig. 2.1, the cleanliness index of the groove machined by the specific end milling condition was presented [21]. Level A corresponds to a burr-free and clean groove. Level B has some residual burrs on the groove surface. Level C displays a thin layer of residual elastomer covering the groove. And, level D is a clogged groove. Note that a burned chip is always associated with grooves with a clogged or a level D cleanliness groove. Therefore, poor cutting action occurred in the clogged groove with chip burning. The two large 12.7 mm diameter tools (Tools 12 and 13) did not generate larger size chips as expected. Even when the workpiece was more fully constrained and clean (level A) grooves were generated, the chips produced by Tools 12 and 13 were still very small, in the 2 to 4 mm range. In Fig. 2.1, some small size chip flakes can also be seen among the chips collected for Tools 12 and 13. For the cutting conditions that generated large size chips, such as, Tools 8 and 10 in Experiment III, the cleanliness of the groove was in the partially-cleaned B and C levels. Both observations further indicate that the size of the chip does not correlate well with the cleanliness of the groove and the complexity of the chip formation process.

The effect of spindle and feed speeds on chip morphology is illustrated in Fig. 2.9. Chips corresponding to the four corners of the test matrix in Experiment V (2900 and 5500 rpm and 2.12 and 14.8 mm/s feed) were examined. These four end milling conditions have the same length of uncut chip (9.97 mm) and, as shown in Table 2.3, different maximum uncut chip thickness. End milling at 2900 rpm and 14.8 mm/s feed speed generates a larger chip. This is also the end milling condition that has the largest

maximum uncut chip thickness of 153.1 μm . Many small size chips (1–2 mm) were mixed in all four end milling conditions. This further demonstrates the frequency of chip breakage and the random chip sizes in end milling elastomers.

2.7. Conclusions

Chip formation observations collected in the 87 elastomer end milling tests were analyzed in this study. Methods to take high quality optical pictures and low magnification SEM micrographs were developed to examine the elastomer chip. A four-step procedure was developed and applied to classify the seven types of elastomer chip morphology. The adiabatic shear band and wavy serration mark have both been observed on elastomer chip under specific end milling conditions.

References

- [1] Nakayama, K., and Ogawa, M., 1978, "Basic Rules on the Form of Chip in Metal Cutting," *Annals of CIRP*, Vol. 27, No. 1, pp. 17-21.
- [2] Nakayama, K., and Arai, M., 1992, "Comprehensive Chip Form Classification Based on the Cutting Mechanism," *Annals of CIRP*, Vol. 41, No. 1, pp. 71-74.
- [3] Jawahir, I. S., and von Luttervelt, C. A., 1993, "Recent Development in Chip Control Research and Applications," *CIRP Annals*, Vol. 42/2, pp. 659-685.
- [4] Venkatesh, V. C., Zhou, D. Q., Xue, W., Quinto, D. T., 1993, "A Study of Chip Surface Characteristics During the Machining of Steel," *CIRP Annals*, Vol. 42/1, pp. 631-636.
- [5] Batzer, S. A., Haan, D. M., Rao, P. D., Olson, W. W., and Sutherland, J. W., 1998, "Chip Morphology and Hole Surface Texture in the Drilling of Cast Aluminum Alloys," *Journal of Materials Processing Technology*, Vol. 79, pp. 72-78.
- [6] Jawahir, I. S., and Balaji, A.K., 2000, "Predictive Modeling and Optimization of Turning Operations with Complex Grooved Cutting Tools for Curled Chip Formation and Chip Breaking," *Machining Science and Technology*, Vol. 4, No. 3, pp. 399-443.
- [7] Trent, E. M., and Wright, P. K., 2001, *Metal Cutting*, 4th Ed., Butterworth-Heinemann.
- [8] Shaw, M. C., 1986, *Metal Cutting Principles*, Oxford.
- [9] Komanduri, R., and Brown, R. H., 1981, "On the Mechanics of Chip Segmentation in Machining," *Journal of Engineering for Industry*, Vol. 103, pp. 33-51.
- [10] Komanduri, R., and von Turkovich, B. F., 1981, "New Observations on the Mechanism of Chip Formation when Machining Titanium Alloys," *Wear*, Vol. 69, pp. 179-188.
- [11] Elbestawi, M.A., Chen, L., Becze, C. E., and El-Wardany, T. I., 1997, "High-Speed Milling of Dies and Molds in Their Hardened State," *CIRP Annals*, Vol. 46/1, pp. 57-62.
- [12] Ng, E. G., Lee, D. W., Sharman, A. R. C., Dewes, R. C., and Aspinwall, D. K., 2000, "High Speed Ball Nose End Milling of Inconel 718," *CIRP Annals*, Vol. 49/1, pp. 41-46.
- [13] Becze, C. E., Clayton, P., Chen, L., El-Wardany, T. I., and Elbestawi, M. A., 2000, "High-speed Five-axis Milling of Hardened Tool Steel," *International Journal of Machine Tool Design and Manufacture*, Vol. 40, No. 6, pp. 869-885.
- [14] Ning, Y., Rahman, M., and Wong, Y. S., 2001, "Investigation of Chip Formation in High Speed End Milling," *Journal of Materials processing Technology*, Vol. 113, pp. 360-367.
- [15] Kobayashi, A., 1981, *Plastics cutting*, Krieger.

- [16] Recht, R. F., 1964, "Catastrophic Thermoplastic Shear," *Journal of Applied Mechanics*, Vol. 31, pp. 189-193.
- [17] Sheikh-Ahmad, J., and Bailey, J. A., 1997, "Flow Instability in the Orthogonal Machining of CP Titanium," *Journal of Manufacturing Science and Engineering*, Vol. 119, pp. 307-313.
- [18] Yang, X., and Liu, C. R., 1999, "Machining Titanium and its Alloys," *Machining Science and Technology*, Vol. 3, No. 1, pp. 107-139.
- [19] Xie, J. Q., Bayoumi, A. E., and Zbib, H.M., 1996, "A Study on Shear Banding in Chip Formation of Orthogonal Machining," *International Journal of Machine Tool and Manufacture*, Vol. 36, No. 7, pp. 835-847.
- [20] von Turkovich, B. F., and Durham, D. R., 1982, "Machining Titanium and its Alloys," D. F. Hasson and C. H. Hamilton (Ed.), *Advanced Processing Methods for Titanium*, pp. 257-274, Metallurgical Society of AIME.
- [21] Shih, A. J., Lewis, M. A., and Strenkowski, J. S., 2004, "End Milling of Elastomers – Fixture Design and Tool Effectiveness for Material Removal," *ASME Journal of Manufacturing Science and Engineering*, Vol. 126, No. 1, pp. 115-123.

Table 2.1. Summary of seven end milling experiments.

Experiment Number	Tools	Workpiece Temperature (°C)	Feed speed (mm/s)	Spindle speed (rpm)
I	1–13	23.0	12.7	4200
II	1–13	0	12.7	4200
III	1–13	-78.6	12.7	4200
IV	6	23.0	2.12, 6.35, 10.6, 14.8	2900, 4200, 5500
V	6	-78.6	2.12, 6.35, 10.6, 14.8	2900, 4200, 5500
VI	8	23.0	2.12, 6.35, 10.6, 14.8	2900, 4200, 5500
VII	8	-78.6	2.12, 6.35, 10.6, 14.8	2900, 4200, 5500

Table 2.2. Peripheral cutting speed and feed in Experiments I – VII.

Spindle (rpm)	End mill peripheral cutting speed (m/min)			Feed ($\mu\text{m}/\text{flute}$) for a double flute end mill {single flute}				
	Tool diameter (mm)			Feed speed (mm/s)				
	3.18	6.35	12.7	2.12	6.35	10.6	12.7	14.8
2900	29.0	57.9	115.7	21.9 {43.9}	65.7 {131.4}	109.7 {219.3}	131.4 {262.8}	153.1 {306.2}
4200	42.0	83.8	167.6	15.1 {30.3}	45.4 {90.7}	75.7 {151.4}	90.7 {181.4}	105.7 {211.4}
5500	55.0	109.7	219.4	11.5 {23.1}	34.6 {69.3}	57.8 {115.6}	69.3 {138.5}	80.7 {161.5}

Table 2.3. Peripheral speed of various end mills and corresponding maximum uncut chip thickness.

Spindle (rpm)	Peripheral speed of the end mill (m/s)			Maximum uncut chip thickness (μm) (for double-flute end milling tools)				
	Tool diameter (mm)			Feed speed (mm/s)				
	3.18	6.35	12.7	2.12	6.35	10.6	12.7	14.8
2900	0.482	0.964	1.928	21.9	65.7	109.7	131.4	153.1
4200	0.698	1.396	2.793	15.1	45.4	75.7	90.7	105.7
5500	0.914	1.829	3.657	11.5	34.6	57.8	69.3	80.7

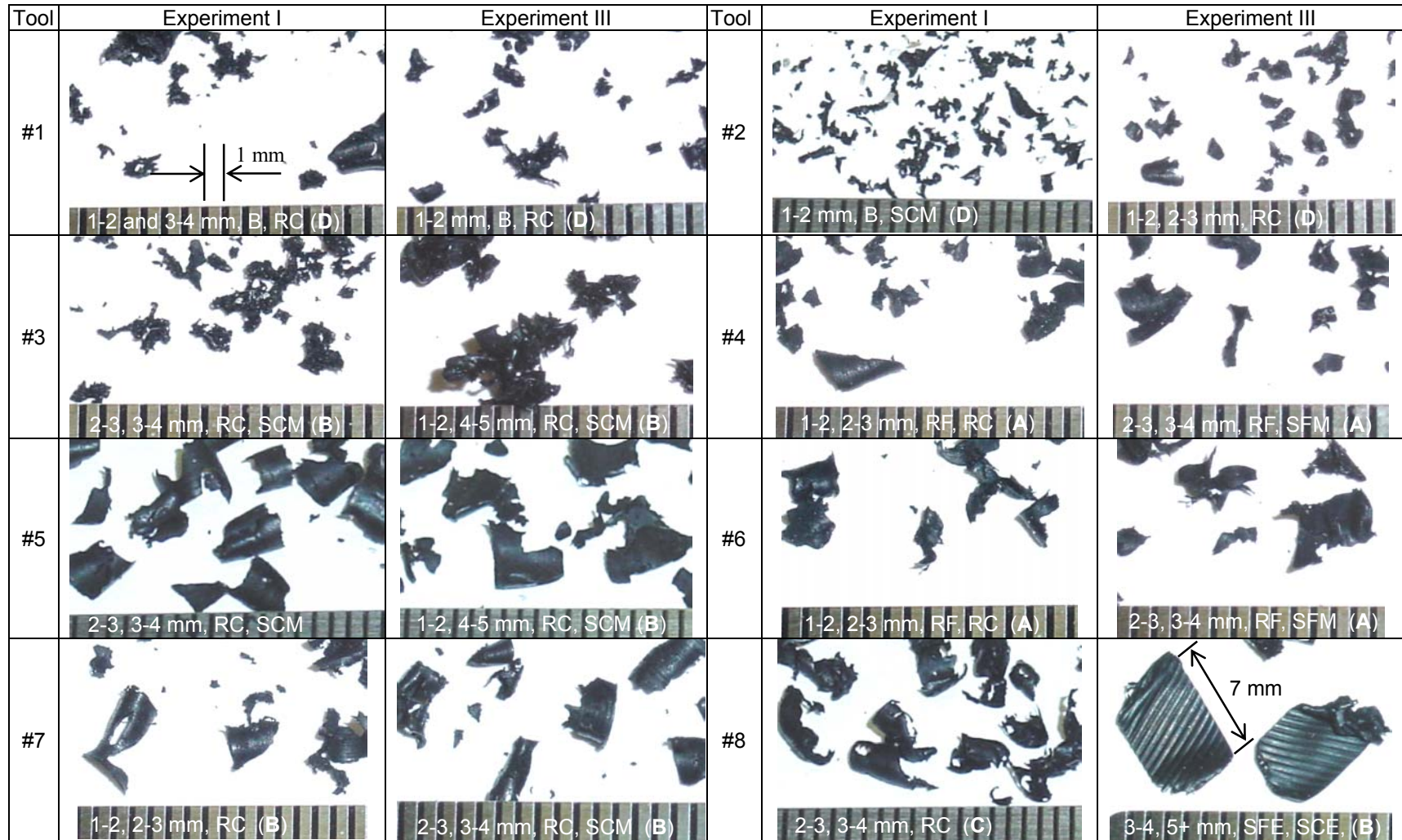
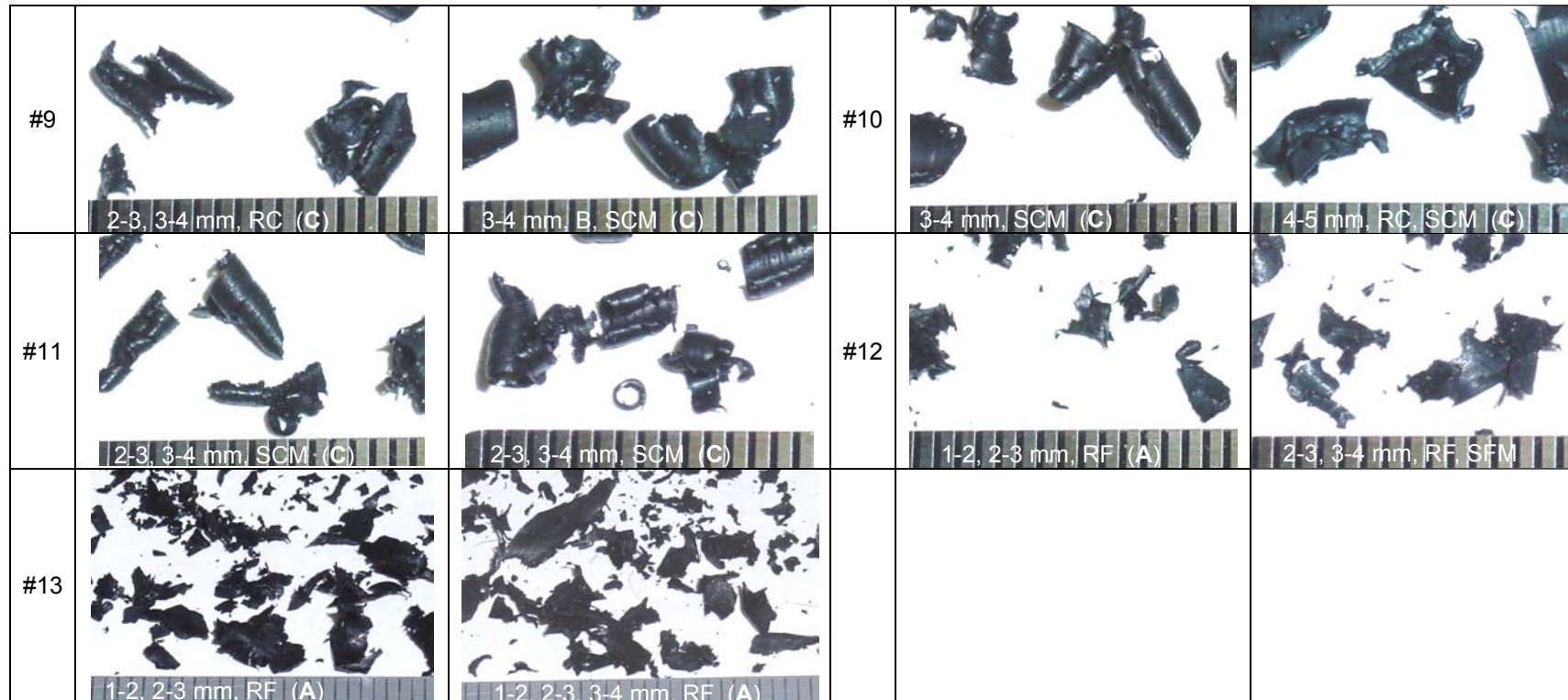


Fig. 2.1. Optical pictures of elastomer chip machined in Experiments I and III using tools #1 to #13.



(): Cleanliness index of end milled groove

Fig. 2.1. (cont.) Optical pictures of elastomer chip machined in Experiments I and III using tools #1 to #13.

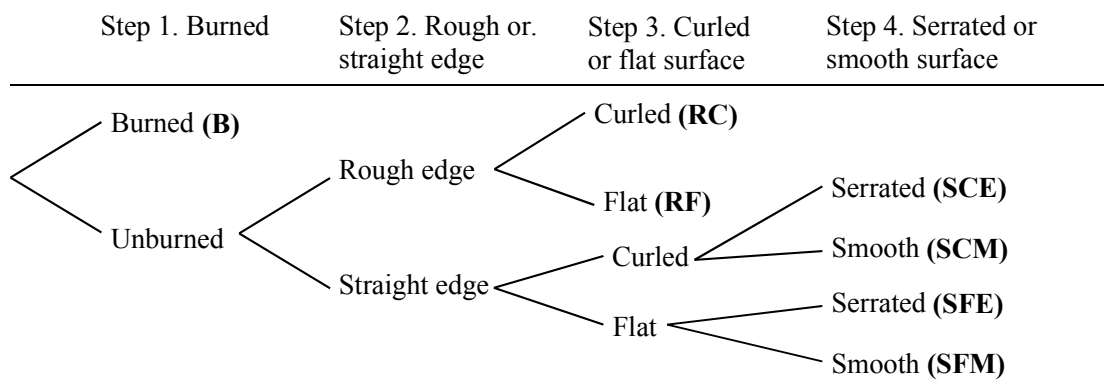


Fig. 2.2. The four-step procedure used to categorize chip morphology for an end milled elastomer.

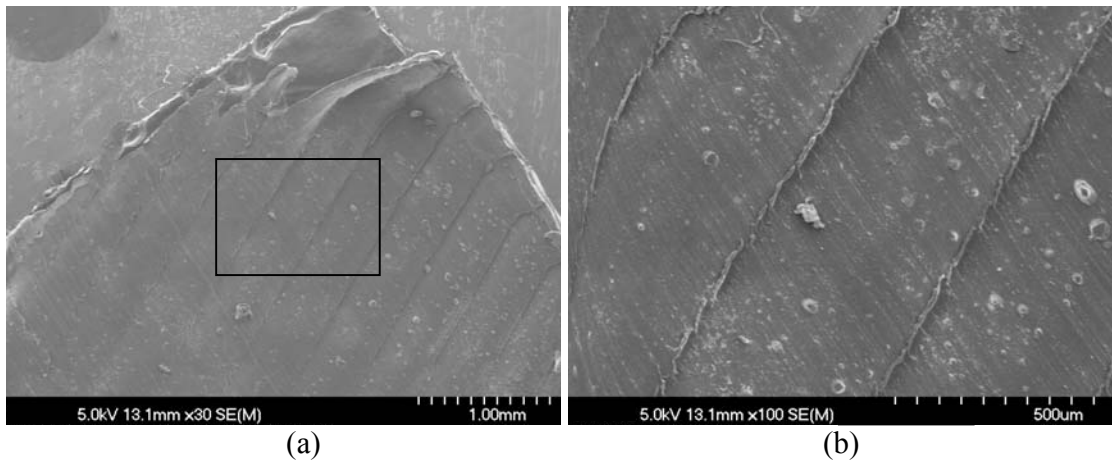


Fig. 2.3. SEM micrographs of adiabatic shear band in the SFE type chip machined by Tool 8 in Experiment VII, 14.8 mm/s feed speed and 4200 rpm spindle speed: (a) overview of the chip, and (b) close-up view shear band in the box in (a).

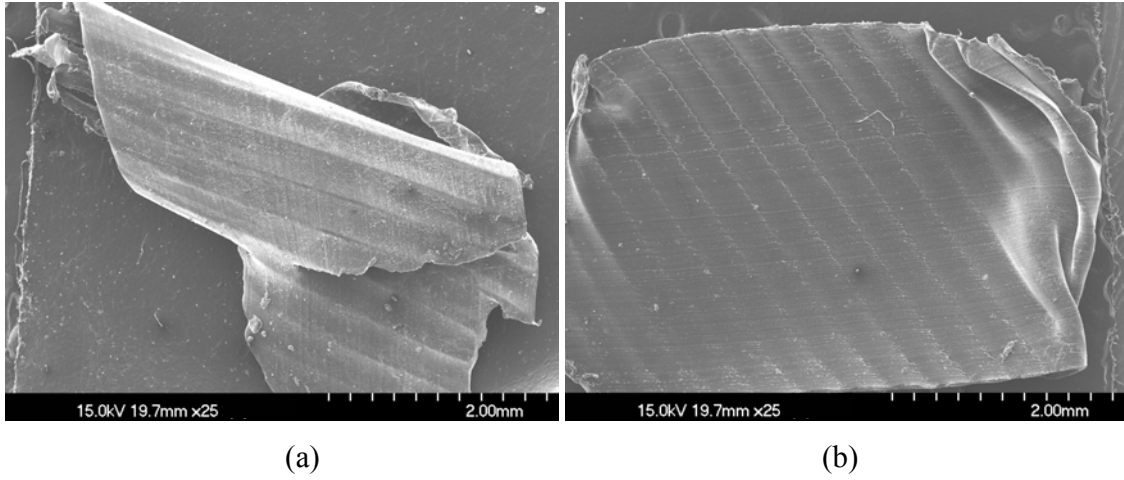


Fig. 2.4. SEM micrographs: (a) a curled, serrated SCE type chip with wavy marks machined by Tool 8 in Experiment III, and (b) a SFE type of chip with the wavy serration mark on the surface.

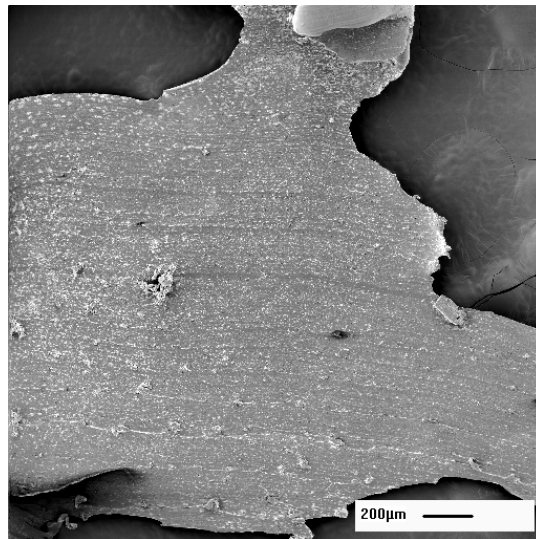


Fig. 2.5. SEM micrographs of a RF type of chip machined by Tool 8 in Experiment I.

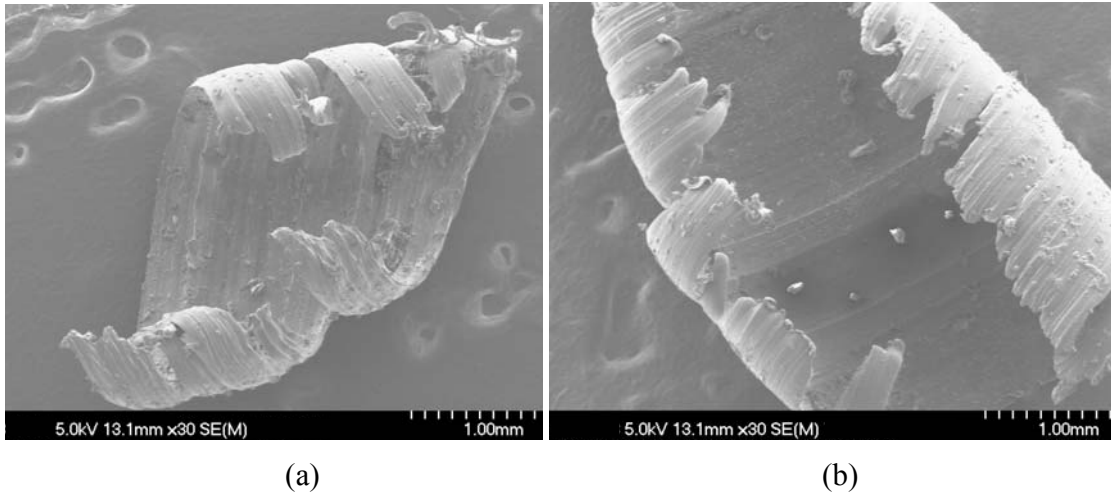


Fig. 2.6. SEM micrographs of SCM type curled chip machined by Tool 11: (a) in Experiment I, and (b) in Experiment III.

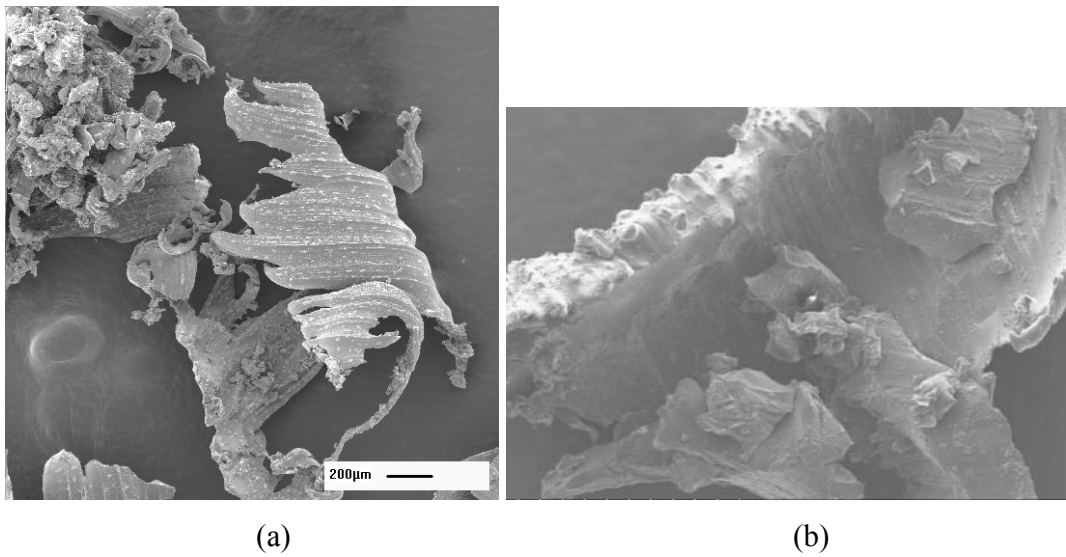


Fig. 2.7. SEM micrographs: (a) The RC and B types of chips machined by Tool 4 with 2.12 mm/s feed speed and 5500 rpm, and (b) chip with burned edge, machined by Tool 2 in Experiment I.

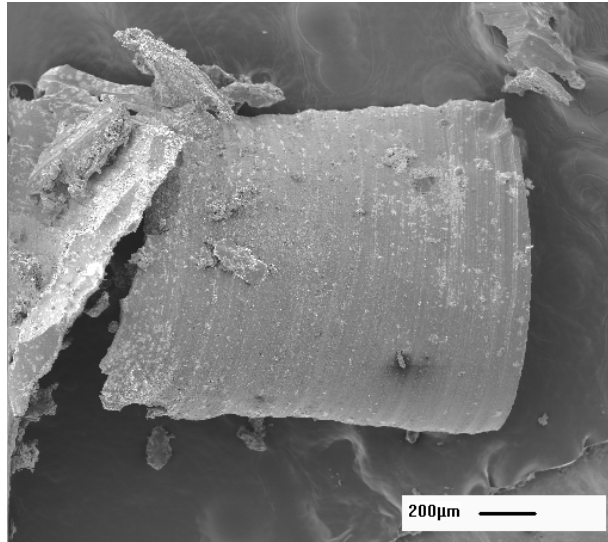


Fig. 2.8. SFM chip machined by Tool 4 at 5500 rpm and 14.8 mm/s feed speed.

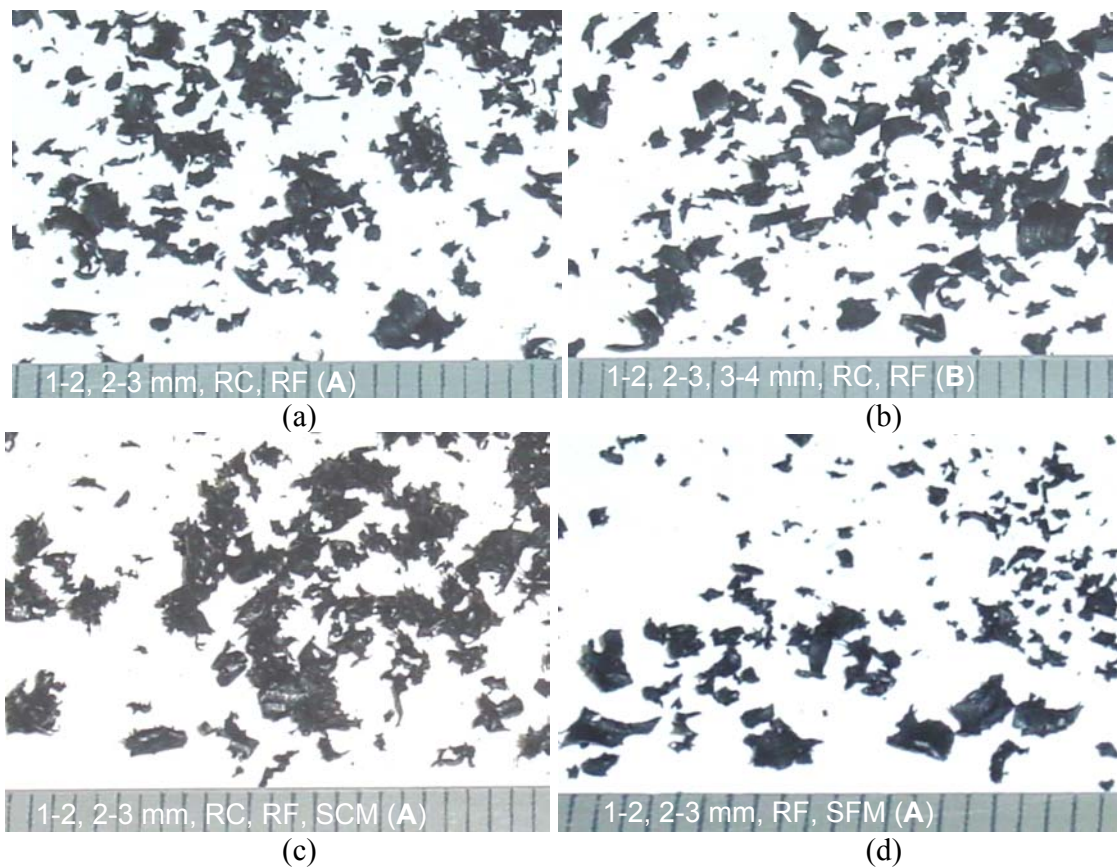


Fig. 2.9. Optical pictures of chip formation in the four corners of the test matrix in Experiment V, Tool 6 at: (a) 2900 rpm, 2.12 mm/s feed, (b) 2900 rpm, 14.8 mm/s feed, (c) 5500 rpm, 2.12 mm/s feed, and (d) 5500 rpm, 14.8 mm/s feed. (A): Cleanliness index of end milled groove.

CHAPTER 3.

INVERSE HEAT TRANSFER SOLUTION OF INDUCTION HEATING

The non-contact induction heating is applied to provide a fast, consistent heat source at a precise location on the tool for machining of elastomers. The tool tip temperature is a key parameter in the machining process. The heat flux generated by induction on the tool is critical to determine the temperature profile and history on a rotating tool. With the heat flux due to induction heating determined, the heating strategy can be designed and the tool tip temperature can be controlled for the machining process. In this chapter, a semi-experimental method is developed to determine the surface heat flux generated by induction.

3.1. Induction heating

Induction heating is a process involving the interaction of both electromagnetic and thermal transport. An eddy current is generated in the workpiece by the varying electromagnetic field produced by the alternating electrical current passing through the water-cooled induction coils. The majority of heat generated by the eddy current due to the Joule heating effect is concentrated in a surface layer of the workpiece. The thickness of this layer, called penetration depth, depends on the electromagnetic field frequency and material properties and is usually very small. The heat generated by induction can be modeled as the workpiece surface heat flux [1]. For electrically conductive work-materials, the induction heating can quickly and accurately produce a desired temperature profile at selected locations. It is a convenient, non-contact heating method widely used in industry for applications such as the heat treatment (hardening, tempering, and annealing), melting, welding, and joining [2–5].

The design of induction heating systems needs to determine the heat generation and the resulting temperature profile in the workpiece. The rate of heat generated in the workpiece is determined by the magnetic and thermal properties of the work-material, electrical current through the induction coil, geometry, position and shape of the coil around the workpiece, as well as many other factors. Numerical modeling, which includes the magnetic and thermal analysis, has been applied to design the induction heating system [2]. The finite element [6–13] and finite difference [14–17] methods have been applied to analyze the electromagnetic field generated by the coil for induction heating. The magnetic vector potential is calculated from the Maxwell's equations and applied to solve the induction heat generation rate or heat flux in the workpiece [6–8,16].

The magnetic permeability of the work-material is a key, but difficult to be accurately determined, parameter to solve the Maxwell's equations. The magnitude of magnetic permeability varies due to the change of magnetic field, temperature, as well as the alloy composition, impurities, and heat treatment of the work-material [13]. Wang et al. [6–8] and Maten and Melissen [9] include the transition of magnetic permeability at Curie temperature and assume that the magnetic permeability is independent of magnetic field. More comprehensive magnetic permeability models, which consider the influence of temperature [10], magnetic intensity [11,12,15,17], or the combination of both temperature and magnetic intensity [14,16], have been developed to study the induction heating process. For newly developed materials, the comprehensive model of the magnetic permeability is also lacking. This has limited the capability to use numerical methods to determine the induction heat flux and the subsequent workpiece thermal modeling.

The goal of this research is to develop a method to experimentally determine the heat flux generated by induction without the information of the magnetic permeability and modeling of the magnetic field. The inverse heat transfer method [18] is applied. The temperature data measured by a thermocouple located near the induction-heated region is used to estimate the heat flux generated on workpiece surface. This method is suitable for a workpiece, such as the shaft and rod, with small variation of temperature across the cross-section, when a single value can represent the temperature in the cross-section. Based on this approach, an explicit finite difference model is developed to solve

the inverse heat transfer problem and to find the induction heat flux based on experimental measurement.

The mathematical modeling is summarized in the following section. Setup of the induction heating experiments and configuration for temperature measurement are then presented. Experimental results and validation of heat flux estimated using the inverse heat transfer model are discussed in Sec. 3.4. Sensitivity to the grid spacing, thermocouple location, and thermophysical properties is investigated in Sec. 3.5. Finally, an example using the estimated heat flux as the input for finite element thermal analysis of induction heating is analyzed and results are compared with the finite difference prediction.

3.2. Mathematical modeling

The finite difference method is developed to solve the inverse heat transfer problem to estimate the surface heat flux generated by induction. The mathematical model developed in this study is targeted for the induction heating of a long and slender shape workpiece, as shown in Fig. 3.1, with low cross-section Biot number (Bi). The effect of Biot number, explicit finite difference modeling, and inverse heat transfer solution of heat flux generated in induction heating are discussed in the following three sections.

3.2.1. Effect of the Biot number

The Biot number is defined as [18]:

$$Bi = \frac{hL_c}{k} \quad (3.1)$$

where h is the convection coefficient, k is the thermal conductivity, and L_c is characteristic dimension of the cross-section, which is the largest span in the cross-section area to represent the worst possible condition of temperature variation. For Bi less than 0.1 [19], the temperature of the cross-section can be represented by a single value at the node in finite difference analysis.

An example is used to demonstrate the size of a carbon steel cross-section that meets the $Bi = 0.1$ criterion. Using the room temperature $k = 52 \text{ W/m}\cdot\text{K}$ for carbon steel workpiece, under the free (natural) convection with $h = 10 \text{ W/m}^2\cdot\text{K}$, L_c is 520 mm. This indicates that, for a cross-section with characteristic dimension less than 520 mm, regardless of the shape of the cross-section, the temperature distribution in the workpiece can be represented by the nodal temperature of a series of connected nodes. Under forced convection with $h = 200 \text{ W/m}^2\cdot\text{K}$, L_c is 26 mm. The high convection coefficient creates larger temperature gradient between the surface and inside of the workpiece and limits the L_c of the cross-section area suitable to be represented by a single temperature.

This example illustrates that, for the metallic material with reasonably high thermal conductivity, a wide range of workpiece cross-section size is applicable using the proposed method. The temperature gradient in the cross-section of the workpiece with low Bi number will be further analyzed by using the finite element method later in Sec. 3.6.

3.2.2. Finite difference modeling of the workpiece with low cross-section Biot number

The induction heating coils generate a heating region in the workpiece. The area without heating is referred as the cooling region. Assuming the workpiece is symmetry in the middle of the heating region, an adiabatic boundary condition exists in the middle of the heating region. The origin of the x axis locates on this adiabatic boundary surface. As shown in Fig. 3.2, half of the workpiece is represented by nodes in both heating and cooling regions. The average temperature of the cross-section in the adiabatic boundary surface is denoted as node 1. There are m_1 nodes in the heating region and m_2 nodes in the cooling region. The spacing between two adjacent nodes in the heating and cooling region is Δx_h and Δx_c , respectively. The length of the workpiece is $2L$ and the width of the heating region is $2L_h$. Therefore, $\Delta x_h = L_h/(m_1-1)$ and $\Delta x_c = (L-L_h)/m_2$. The perimeter and area of cross-section at node m is denoted P_m and A_m , respectively. The control volume at node m , as shown in Fig. 3.3, is V_m . Induction heating starts from time $t = 0$ and ends when $t = t_h$. The heat flux generated in the heating region during heating stage

($0 \leq t \leq t_h$) is assumed uniform. When $t > t_h$, heating stops and the whole workpiece is cooled under the convection and radiation.

Based on the energy balance method, explicit finite difference equations are derived for the heating and cooling stages.

3.2.2.1. Heating stage, $0 \leq t \leq t_h$

As shown in Fig. 3.3, the energy exchange in the control volume at node m is influenced by the conduction between the node m and adjacent nodes $m-1$ and $m+1$ and the convection, radiation, and induction heat generation on the peripheral surface $P_m \Delta x$, Δx is the width of the control volume. The conduction rate from node $m-1$ to m and from node $m+1$ to m is represented by heat flux $q''_{cond,m-1}$ and $q''_{cond,m+1}$, respectively. The heat flux due to convection and radiation on the peripheral surface of the control volume at node m is q''_{conv} and q''_{rad} , respectively. A uniform heat flux q''_{ind} is applied on the surface of the peripheral heating region. Based on the finite difference method, the energy balance of the control volume at node m can be derived as:

$$(q''_{cond,m-1} + q''_{cond,m+1}) \cdot A_m + (q''_{ind} - q''_{conv} - q''_{rad}) \cdot P_m \cdot \Delta x = \rho c \cdot A_m \Delta x \cdot \frac{T_m^{p+1} - T_m^p}{\Delta t} \quad (3.2)$$

where ρ is the density, c is the specific heat, Δt is the time increment, and T_m^p is the nodal temperature at node m and time step p .

All the nodes fall into the following three categories: nodes in the heating region, nodes in the cooling region, and boundary nodes.

(i) Nodes in the heating region ($2 \leq m \leq m_1-1$)

The energy balance in the control volume at node m in the heating region during the heating stage can be expressed as:

$$k \cdot A_m \cdot \frac{T_{m+1}^p + T_{m-1}^p - 2T_m^p}{\Delta x_h} + (q''_{ind} - q''_{conv} - q''_{rad}) \cdot P_m \cdot \Delta x_h = \rho c \cdot A_m \Delta x_h \cdot \frac{T_m^{p+1} - T_m^p}{\Delta t} \quad (3.3)$$

(ii) Nodes in the cooling region ($m_1+1 \leq m \leq m_1+m_2-1$)

For nodes in the cooling region, Eq. (3.3) with $q''_{ind} = 0$ is the energy balance equation.

(iii) Boundary nodes (1, m_1 , m_1+m_2)

Three boundary nodes exist on the adiabatic boundary surface (node 1), at the interface between the heating and cooling regions (node m_1), and at the end of cooling region (node m_1+m_2). To determine the thermal conditions more accurately, the half-width control volumes are assigned to the corresponding boundary nodes.

The energy balance of the control volume at node 1 is

$$k \cdot A_1 \cdot \frac{T_2^p - T_1^p}{\Delta x_h} + (q''_{ind} - q''_{conv} - q''_{rad}) \cdot P_1 \frac{\Delta x_h}{2} = \rho c \cdot A_1 \frac{\Delta x_h}{2} \cdot \frac{T_1^{p+1} - T_1^p}{\Delta t} \quad (3.4)$$

The energy balance of the control volume at boundary node m_1 is

$$\begin{aligned} k \cdot A_{m_1} \cdot \left(\frac{T_{m_1+1}^p - T_{m_1}^p}{\Delta x_c} + \frac{T_{m_1-1}^p - T_{m_1}^p}{\Delta x_h} \right) + q''_{ind} \cdot P_{m_1} \frac{\Delta x_h}{2} - (q''_{conv} + q''_{rad}) \cdot P_{m_1} \left(\frac{\Delta x_h}{2} + \frac{\Delta x_c}{2} \right) \\ = \rho c \cdot A_{m_1} \frac{(\Delta x_h + \Delta x_c)}{2} \cdot \frac{T_{m_1}^{p+1} - T_{m_1}^p}{\Delta t} \end{aligned} \quad (3.5)$$

The energy balance of the control volume at boundary node m_1+m_2 is

$$\begin{aligned} k \cdot A_{m_1+m_2} \cdot \frac{T_{m_1+m_2-1}^p - T_{m_1+m_2}^p}{\Delta x_c} - (q''_{conv} + q''_{rad}) \cdot (P_{m_1+m_2} \frac{\Delta x_c}{2} + A_{m_1+m_2}) \\ = \rho c \cdot A_{m_1+m_2} \frac{\Delta x_c}{2} \cdot \frac{T_{m_1+m_2}^{p+1} - T_{m_1+m_2}^p}{\Delta t} \end{aligned} \quad (3.6)$$

3.2.2.2. Cooling stage, $t > t_h$

No heat flux is generated by induction during the cooling stage. Eqs. (3.3)-(3.6) with $q''_{ind} = 0$ can be used as the finite difference representation of energy balance at all nodes.

3.2.2.3. Convection and radiation heat flux

A good approximation of the heat flux of a vertical wall due to free convection in air can be expressed using the following equation [4]

$$q''_{conv} = B(T_m^p - T_\infty)^{1.25} \text{ [W/m}^2\text{]} \quad (3.7)$$

where $B = 1.8 \text{ W/m}^2\cdot\text{K}^{1.25}$ for vertical walls, $1.3 \text{ W/m}^2\cdot\text{K}^{1.25}$ for downward inclining horizontal walls, and $1.5 \text{ W/m}^2\cdot\text{K}^{1.25}$ for upward inclining horizontal walls, and T_∞ is the ambient temperature.

The radiation heat flux can be expressed as

$$q''_{rad} = \sigma_s \varepsilon ((T_m^p + 273)^4 - (T_\infty + 273)^4) \text{ [W/m}^2\text{]} \quad (3.8)$$

where ε is the emissivity of the work-material and σ_s is the Stefan-Boltzmann constant ($\sigma_s = 5.67 \times 10^{-8} \text{ W/m}^2\cdot\text{K}^4$).

3.2.3. Inverse heat transfer modeling

The only unknown in the finite difference model presented in Sec. 3.2.2 to solve the spatial and temporal temperature distribution is the heat flux q''_{ind} in the heating region. The inverse heat transfer method is applied to solve q''_{ind} by using the experimentally measured temperatures at given locations on the workpiece. The measured temperature at the location x_j of thermocouple j and time t_i is denoted as

$$T_{x_j}^{t_i}|_{\text{exp}}$$

Based on finite difference equations in Sec. 3.2.2, the nodal temperature T_m^{p+1} at node m and time step $p+1$ can be expressed as a function of temperatures T_{m-1}^p , T_m^p , and T_{m+1}^p at prior time step p . The actual value of q_{ind}'' is an unknown. Using an estimated value of q_{ind}'' and the initial temperature of the workpiece T_m^0 at time step $p = 0$, the temperature $T_{x_j|est}^{t_i}$ at location x_j and time t_i can be calculated. The discrepancy between the experimentally measured $T_{x_j|exp}^{t_i}$ and finite difference model estimated $T_{x_j|est}^{t_i}$ depends on the q_{ind}'' . An objective function as the summation of the squares of the temperature discrepancy is defined as:

$$Obj(q_{ind}'') = \sum_{i=1}^{n_1} \sum_{j=1}^{n_2} (T_{x_j|exp}^{t_i} - T_{x_j|est}^{t_i})^2 \quad (3.9)$$

where n_1 is the number of time instants applied in the estimation algorithm, and n_2 is the number of thermocouples applied in the estimation algorithm.

By minimizing $Obj(q_{ind}'')$, the value of q_{ind}'' can be obtained. The golden section search method [20] is applied to find q_{ind}'' that minimizes $Obj(q_{ind}'')$. A search range for q_{ind}'' needs to be determined using the golden section search method. The lower bound of q_{ind}'' is 0, which represents that no heat flux is generated during the induction heating. The upper bound is determined by dividing the peak power output of the induction heating power supply and the peripheral surface area of the heating region. The correct value of q_{ind}'' that minimizes $Obj(q_{ind}'')$ lies between the upper and lower bounds and can be solved using the golden section search method.

3.3. Experiment

As shown in Fig. 3.4, the induction heating experiment was conducted on a vertically suspended AISI 1020 low carbon steel rod, 1140 mm in length ($2L$) and 6.35 mm in radius (r). The water-cooled induction coil, 4 mm in outside diameter, is located

in the middle of the rod and creates a 11.3 mm wide ($2L_h$) heating region. An Ameritherm NOVA 1.0 induction heating unit is used to generate the alternating current in the coil, which produces the eddy current and the surface heating of the workpiece. The induction heating system automatically scans the operating frequency range from 50 to 450 kHz and selects the optimum operating frequency based on the coil and load combination. For the rod and coil combination shown in Fig. 3.4, the operating frequency was 270 kHz and the power output was set at 0.8 kW.

Four type K thermocouples (Omega CO1-K) with butt bonded junction, tip size of 2.5 mm by 3.0 mm, and 10 to 20 ms response time are attached to the steel rod. As illustrated in the configuration of the induction heating experimental setup in Fig. 3.5, the location of thermocouple 1 through 4 is marked as x_1 to x_4 , respectively. In this study, $x_1 = 28.6$ mm, $x_2 = 35.8$ mm, $x_3 = 68.6$ mm, and $x_4 = 129.0$ mm. Voltage signals from thermocouples are acquired using a 4-channel PC-based data acquisition system with the 250 Hz sampling rate. During the heating stage, the electromagnetic interference generates noise in the thermocouple voltage output and prohibits the temperature measurement. The measured temperature data is averaged and recorded every 0.5 s.

Three experiments are carried out with the duration of heating t_h set at 15, 20, and 25 s. Each experiment is repeated three times to verify its repeatability.

3.4. Results

The experimental temperature measurements, calculated induction heat flux and finite difference modeling results, comparison of the experimental and modeling results, and measurement error analysis are discussed in the following sections.

3.4.1. Experimental temperature measurements

Fig. 3.6 shows an example of the measured temperature during the cooling stage at four thermocouples with $t_h = 25$ s. For a specific thermocouple, the temperature peaked at time t_{peak} . The magnitude of the peak temperature is denoted as T_{peak} . Since the heat generated by induction transfers like a thermal wave from the heating region toward both ends of the rod, the thermocouple closer to the heating region has the higher T_{peak} and lower t_{peak} . The thermal energy is transferred via conduction through the rod.

In the meantime, the thermal energy is also dissipated from the peripheral surface by convection and radiation and stored in the rod due to the increase in workpiece temperature and heat capacity, ρc . The loss and storage energy result the reduction in peak temperature T_{peak} for thermocouples away from heating region.

The t_{peak} and T_{peak} at thermocouple 1 for the three repeated tests conducted at $t_h = 15, 20, \text{ and } 25$ s are listed in Table 3.1. Longer duration of heating t_h delivers more energy to the rod and generates higher temperature T_{peak} . Longer t_h also delays the time t_{peak} for the thermocouple to reach the peak temperature. Three repeated tests show good agreement in T_{peak} with less than 2% discrepancy. However, the maximum discrepancy of t_{peak} is about 11%. This is due to the relatively flat temperature response near the peak. As shown later in the Sec. 3.4.2, such discrepancy does not significantly change the calculated heat flux.

3.4.2. Calculated heat flux and finite difference modeling results

The finite difference model and inverse heat transfer method presented in Sec. 3.2 are applied to solve q''_{ind} . The grid with number of node in the heating region $m_1 = 3$ and number of node in the cooling region $m_2 = 201$ is applied in the modeling. The experimentally measured temperature, thermocouple location, and material properties are the required input. For the AISI 1020 steel, $\rho = 7870 \text{ kg/m}^3$, and temperature-dependent properties is obtained by linear interpolation or extrapolation with $c = 486 \text{ J/kg}^2\cdot\text{K}$ and $k = 51.9 \text{ W/m}\cdot\text{K}$ at 20°C and $c = 519 \text{ J/kg}^2\cdot\text{K}$ and $k = 48.9 \text{ W/m}\cdot\text{K}$ at 200°C [21]. Eq. (3.7) is used to estimate the convection heat flux with $B = 1.8 \text{ W/m}^2\cdot\text{K}^{1.25}$. The convection coefficient varies from 0 to $6.8 \text{ W/m}^2\cdot\text{K}$ with $T_m^p - T_\infty$ varying from 0 to 200°C , which corresponds to Bi from 0 to 0.00167. The low Bi confirms that the assumption of uniform temperature in the cross-section is suitable for this study. The ambient temperature T_∞ and initial temperature of the rod at $t = 0$ are both 21.4°C . The emissivity for thermal radiation heat flux in Eq. (3.8) is 0.7 [2].

Many options for selecting experimental data points of measured temperature for minimizing the objective function in Eq. (3.9) are possible. It can be one point, typically the peak temperature, such as E_2 (48.5 s, 228.0°C) in Fig. 3.6. Or, it can be the

combination of several points, such as the E₁ (28.5 s, 181.6°C), E₂, and E₃ (78.5 s, 212.0°C). When only one data point is used, if the peak temperature is not selected, the modeling usually cannot accurately predict q''_{ind} .

An example is used to illustrate the effect of data points selection. If one data point E₂ in Fig. 3.6 is used, the calculated q''_{ind} is 1.103 MW/m². If E₁, E₂, and E₃ are used, $q''_{ind} = 1.122$ MW/m². This demonstrates that one peak temperature data point can provide accurate estimation of q''_{ind} .

Using the T_{peak} and corresponding t_{peak} of the four thermocouples in three repeated tests (Tests I, II, and III) of three experiments with $t_h = 15, 20,$ and 25 s, results of the 36 (=3×3×4) estimated q''_{ind} are summarized in Table 3.2. For three repeated tests, the calculated q''_{ind} is very repeatable, less than 3.0% discrepancy, at thermocouples 1, 2, and 3. The slight difference may be caused by inconsistent induction power output at the beginning of the operation, which was observed during the experiments. Relatively high discrepancy, from 2.4 to 10.2%, can be seen in repeated tests conducted using the temperature data of thermocouple 4. The relatively low temperature, flat peaks of temperature profile, and the long distance from the heating region all contribute to the discrepancy in repeated test results. Also seen in the last three rows of Table 3.2, for experiments at the same t_h , the average q''_{ind} estimated by the peak temperature at four thermocouples has some, but not significant, discrepancy. In summary, Table 3.2 demonstrates the feasibility of the proposed method to use a single measured temperature data point to estimate the q''_{ind} and the consistency of the induction heating tests.

3.4.3. Comparison of experimental and modeling results

Based on the calculated induction heat flux q''_{ind} , the temporal and spatial distribution of temperature on the rod can be analyzed using the finite difference method. The T_{peak} and t_{peak} at thermocouple 1 was used to calculate heat flux q''_{ind} . Using this q''_{ind} , the finite difference modeling was used to calculate the temperature. Results of the finite difference modeling (open symbols) and experimental measurement (lines) at four

thermocouple locations are illustrated and compared in Fig. 3.7. Good match can be seen at point E_2 , the location of T_{peak} and t_{peak} of thermocouple 1.

The root mean square (RMS) error, e_{RMS} , is defined as following [18],

$$e_{RMS} = \sqrt{\frac{1}{N} \sum_{i=1}^N (T_{x_j|exp}^{t_i} - T_{x_j|est}^{t_i})^2} \quad (3.10)$$

where N is the number of measurements.

The e_{RMS} is calculated at each thermocouple to quantify the discrepancy between the experimental and modeling temperature results.

As shown in Fig. 3.7, temperatures at four thermocouples were measured when $28 < t < 400$ s. At each thermocouple, a total of 744 measurements were conducted. The e_{RMS} of thermocouple 1, 2, 3, and 4 is equal to 2.6, 3.7, 2.9, and 1.0°C, which is 1.13%, 2.02%, 2.85%, and 1.82% of its corresponding T_{peak} s, respectively. The e_{RMS} is due to the measurement errors and approximation of temperature-dependent thermophysical properties. The effect of measurement errors is discussed in the next section.

It is noted that, since the q''_{ind} is calculated using the data of T_{peak} and t_{peak} of thermocouple 1, the error at thermocouple 1 is the lowest. Also, the finite difference modeling is able to predict the workpiece temperature during the heating stage ($0 < t < 25$ s), as the information not available in thermocouple-based experimental measurement. This is shown by the open symbols in Fig. 3.7.

3.4.4. Measurement error analysis

Four measurement errors and uncertainties have been identified as the key parameters that affect the estimated heat flux q''_{ind} . These four parameters are: 1. the error of measured peak temperature T_{peak} , 2. the error of ambient temperature T_{∞} , 3. the uncertainty of thermocouple location x_j , and 4. the uncertainty of the instant for peak temperature t_{peak} . Based on experimental data, the 95% confidence interval of the temperature reading is $\pm 0.8^\circ\text{C}$. This is used as the error of T_{peak} and T_{∞} . The uncertainty

of t_{peak} is assumed as ± 0.25 s (the interval of temperature data reading) and the uncertainty of x_j is assumed as ± 1.5 mm (the tip size of the thermocouple).

Higher T_{peak} , t_{peak} , and x_j and lower T_∞ result larger q''_{ind} . The upper bound and lower bound of the heat flux q''_{ind} can then be calculated. Result shows that the variance for the worst case of q''_{ind} due to the extreme case of four measurement errors and uncertainties is less than $\pm 0.04 q''_{ind}$ at thermocouple 1. This demonstrates the insignificant influence of the measurement errors and uncertainties on the heat flux q''_{ind} .

3.5. Sensitivity analysis

The grid spacing, thermocouple location, and thermophysical properties used in the finite difference modeling all contribute to the variation of q''_{ind} . The sensitivity to these factors to the inverse heat transfer solution of q''_{ind} is studied.

3.5.1. Sensitivity to grid spacing

The selection of the number of nodes is a compromise of computational time and accuracy of modeling results. A test matrix with the number of nodes in the heating region $m_1 = 3, 5,$ and 9 and the number of nodes in the cooling region $m_2 = 101, 201, 401,$ and 801 is selected to analyze the influence of grid spacing on q''_{ind} . Results of q''_{ind} are shown in Fig. 3.8.

With the finest grid spacing of $m_1 = 9$ and $m_2 = 801$, q''_{ind} is 1.1157 MW/m². This is the baseline to study the influence of grid spacing. There is a significant drop of q''_{ind} from 1.1223 to 1.1173 MW/m² when m_2 is increased from 101 to 201 . The influence of m_1 on q''_{ind} is negligible when $m_2 < 201$. For $m_2 \geq 201$, the discrepancy of q''_{ind} with $m_1 = 3$ and $m_2 = 801$ to the baseline result is very small, less than 0.08% . This indicates that the choice of $m_1 = 3$ and $m_2 = 201$ in Sec. 3.4.2 is good for both computational efficiency and accuracy.

3.5.2. Sensitivity to thermocouple location

The sensitivity coefficient of the heat flux is defined as

$$\frac{\partial T(x_j, t_i, q)}{\partial q} \approx \frac{T(x_j, t_i, (1+\eta)q) - T(x_j, t_i, (1-\eta)q)}{2\eta q} \quad (3.11)$$

where η is a perturbation.

Higher sensitivity coefficient represents that the inverse problem is less sensitive to the measurement errors and more accurate estimates of parameters can be obtained [18]. The sensitivity coefficient of the heat flux for different thermocouples at their own t_{peak} is calculated and compared with each other. When $q''_{ind} = 1.103 \text{ MW/m}^2$ and $\eta = 10^{-6}$, the thermocouple 1 through 4 exhibits peak temperature at 48.2, 63.7, 159.2, and 401.1 s and has 1.817×10^{-4} , 1.456×10^{-4} , 0.691×10^{-4} , and $0.276 \times 10^{-4} \text{ K}\cdot\text{m}^2/\text{W}$ sensitivity coefficient of the heat flux, respectively. Thermocouple 1 has the largest sensitivity coefficient and is the best location, among four thermocouples, to calculate the heat flux. This is also the thermocouple selected for inverse heat transfer analysis in this study.

3.5.3. Sensitivity to thermophysical properties

In Eqs. (3.7) and (3.8), $B = 1.8 \text{ W/m}^2\cdot\text{K}^{1.25}$ and $\varepsilon = 0.7$ are used to calculate the heat flux due to the convection and radiation in the finite difference modeling. The influence of uncertainties of these two coefficients on q''_{ind} is investigated by changing the nominal values of B and ε separately. When the B is varied by $0.9 \text{ W/m}^2\cdot\text{K}^{1.25}$ from its nominal value of $1.8 \text{ W/m}^2\cdot\text{K}^{1.25}$ and ε is varied by 0.3 from the nominal 0.7, results of the nine estimated q''_{ind} as well as the discrepancy to the nominal value of q''_{ind} (with $B = 1.8 \text{ W/m}^2\cdot\text{K}^{1.25}$ and $\varepsilon = 0.7$) are listed in Table 3.3. The maximal discrepancy is less than 3.6%, which shows that the uncertainties of B and ε have some but not significant effect on q''_{ind} .

3.6. Finite element verification

The accuracy of finite difference model using a single nodal temperature value to represent the temperature distribution of the entire cross-section is studied using the finite element method. The actual temperature distribution varies in the radial direction of the

workpiece. In the heating region during the heating stage, the temperature difference between the center and surface of the workpiece can be large. Such temperature distribution is quantified using the finite element method. Results from the ANSYS finite element analysis are applied to validate the uniform temperature assumption and accuracy of finite difference modeling.

The AISI 1020 steel rod used in the previous sections for the induction heating experiment and finite difference modeling is meshed using the four-node, four degree-of-freedom quadrilateral axisymmetric elements. The mesh is shown in Fig. 3.9. Ten elements (eleven nodes) across the radial direction and a total of 1260 elements are used in the $0 \leq x \leq 80.01$ mm area. These elements are 0.635 mm by 0.635 mm square shape. In the region of $x > 80.01$ mm, the mesh with 1919 elements is automatically generated by the ANSYS. Mesh in this region has less effect of the simulation results and does not need to be as dense as in the $0 \leq x \leq 80.01$ mm area.

Along the center axis and in the symmetric plane of the rod ($x = 0$), as shown in Fig. 3.10, the boundary condition is adiabatic. The heat flux due to radiation and convection, calculated by the same equations as in the finite difference modeling (Sec. 3.2), is applied on the outer surface. Based on Sec. 3.4, a constant induction heat flux of 1.200 MW/m^2 is applied on the peripheral surface of the heating region. The induction heating time $t_h = 25$ s.

Results of the finite element analysis at $t = 15.0, 20.0,$ and 25.0 s and cross-sections at $x = 0$ mm (middle of the heating region), $x = 5.6$ mm (the interface of the heating and cooling regions) and $x = 30$ mm (location of thermocouple 1) are shown in Fig. 3.10 (marked as FEM). For mutual comparison, the nodal temperature at corresponding positions and time instants are also obtained using the finite difference model (marked as FD model) and plotted as the horizontal dash lines in Fig. 3.10.

The finite element method is used to calculate the eleven nodal temperatures in the same cross-section. At the cross-section $x = 0$ mm when $t = 15.0$ s, the rod center and peripheral temperature is 492.2 and 571.3°C , respectively. The temperature difference in the cross-section is about 80°C , which is significantly different from the constant cross-section temperature assumption used in the finite difference modeling. The finite difference method estimates that the temperature of the cross-section is 538.2°C . The

average of eleven nodal temperatures solved by finite element method is 532.1°C, which has only 1.1% discrepancy with the finite difference modeling. Similarly, for the cross-section at $x = 0$ mm when $t = 20.0$ and 25.0 s, although the difference in temperature between the center and peripheral of the rod is about 80°C, the nodal temperature obtained from the finite difference method, 635.2 and 720.1°C, respectively, is also very close to the average temperatures solved using the finite element method at the eleven nodes of the same cross-section.

The comparison of results obtained from finite difference method (nodal temperature) and finite element method (average cross-section temperature) at three cross-sections ($x = 0, 5.6,$ and 30 mm) and three time instants ($t = 15.0, 20.0,$ and 25.0 s) is summarized in Table 3.4. Very good agreement, less than 2.0 % discrepancy, can be seen in the cross-sections $x = 0$ and 5.6 mm.

In the cross-section away from the heating region, the temperature difference between the center and peripheral of the rod becomes smaller. As shown in Fig. 3.10, at $x = 5.6$ mm, the temperature difference is about 40°C. At $x = 30$ mm, the temperature distribution is almost constant with less than 0.2°C ($t = 25.0$ s) difference from the center to the peripheral surface. This validates the use of a single value to represent the temperature of the cross-section in the finite difference formulation to solve the induction heat flux.

3.7. Conclusions

The explicit finite difference and inverse heat transfer modeling was developed to solve the surface heat flux generated by induction of a long workpiece with low cross-section Biot number. Experiments of induction heating of a carbon steel rod were carried out. Measured temperature data provided not only the input for inverse heat transfer solution but also the validation of the finite difference model. The sensitivity to the grid spacing, thermocouple location, and thermophysical properties was discussed. The finite element analysis showed significant difference in temperature variation in the cross-section during heating and also demonstrated the feasibility to use a single nodal temperature to represent the average cross-section temperature in finite difference modeling.

This study demonstrates the application of inverse heat transfer method to design and analyze the manufacturing process. The finite difference method presented in this study can be enhanced using the implicit formulation, which is expected to improve the computational time.

The temperature data from a thermocouple or infrared sensor can be used as the input for the inverse heating transfer solution of induction heat flux. This heat flux can be the input for induction heating of moving parts with complicated shape to further estimate the temperature profile on the tool.

References

- [1] Brown, G. H., Hoyler, C. N., and Bierwirth, R. A., 1947, *Theory and Application of Radio-Frequency Heating*, D. Van Nostrand Company, New York.
- [2] Rudnev, V., Loveless, D., Cook, R., and Black, M., 2003, *Handbook of Induction Heating*, Marcel Dekker, New York.
- [3] Simpson, P. G., 1960, *Induction Heating*, McGraw-Hill, New York.
- [4] Orfueil, M., 1987, *Electric Process Heating*, Battelle Press, Ohio.
- [5] Semiatin, S. L., 1986, *Induction Heat Treatment of Steel*, American Society for Metals, Ohio.
- [6] Wang, K. F., Chandrasekar, S., and Yang, H. T., 1992, "Finite Element Simulation of Induction Heat Treatment and Quenching of Steel," Transactions of the North American Manufacturing Research Institution of SME, **20**, pp. 83-90.
- [7] Wang, K. F., Chandrasekar, S., and Yang, H. T., 1995, "Finite Element Simulation of Moving Induction Heat Treatment," Journal of Materials Engineering and Performance, **4**(4), pp. 460-473.
- [8] Wang, K. F., Chandrasekar, S., and Yang, H. T., 1992, "Finite Element Simulation of Induction Heat Treatment," Journal of Materials Engineering and Performance, **1**(1), pp. 97-112.
- [9] ter Maten, E. J. W., and Melissen, J. B. M., 1992, "Simulation of Inductive Heating," IEEE Transactions on Magnetics, **28**(2), pp. 1287-1290.
- [10] Chaboudez, C., Clain, S., Glardon, R., Mari, D., Rappaz, J., and Swierkosz, M., 1997, "Numerical Modeling in Induction Heating for Axisymmetric Geometries," IEEE Transactions on Magnetics, **33**(1), pp. 739-745.
- [11] Chaboudez, C., Clain, S., Glardon, R., Rappaz, J., Swierkosz, M., and Touzani, R., 1994, "Numerical Modeling of Induction Heating of Long Workpieces," IEEE Transactions on Magnetics, **30**(6), pp. 5028-5037.
- [12] Melander, M., 1985, "Computer Predictions of Progressive Induction Hardening of Cylindrical Components," Materials Science and Technology, **1**(10), pp. 877-882.
- [13] Kurek, K., Przulucki, R., and Ulrych, B., 1996, "Nonstationary Thermal Field in the Induction Heating System with Axial Symmetry," Acta Technica CSAV (Ceskoslovensk Akademie Ved), **41**(4), pp. 405-417.
- [14] Skoczkowski, T. P., and Kalus, M. F., 1989, "The Mathematical Model of Induction Heating of Ferromagnetic Pipes," IEEE Transactions on Magnetics, **25**(3), pp. 2745-2750.
- [15] Labridis, D., and Dokopoulos, P., 1989, "Calculation of Eddy Current Losses in Nonlinear Ferromagnetic Materials," IEEE Transactions on Magnetics, **25**(3), pp. 2665-2669.
- [16] El-Kaddah, N., Craen, R., and Loue, W., 1998, "Mathematical Model of Induction Heating of Thixoformable Aluminum Billets," Light Metals, Proceedings of the

Technical Sessions Presented by the TMS Aluminum Committee at the 127th TMS Annual Meeting, San Antonio, Texas, February 15-19, pp. 1097-1102.

- [17] Kunshchikov, V. G., 1998, "Mathematical Model of Induction Heating of a Cylinder for Computer-Aided Manufacturing (CAM)," *Journal of Engineering Physics and Thermophysics*, **71**(3), pp. 546-550.
- [18] Ozisik, M. N., and Orlande, H. R. B., 2000, *Inverse Heat Transfer*, Taylor & Francis, New York.
- [19] Incropera, F. P., and Dewitt, D. P., 2002, *Fundamentals of Heat and Mass Transfer*, John Wiley & Sons, New York.
- [20] Himmelblau, D. M., 1972, *Applied Nonlinear Programming*, McGraw-Hill, New York.
- [21] Bringas, E. R., Wayman, M. L., Wayman, M., 2000, *The Metals Black Book*, 4th Ed., Casti Publishing Inc, Edmonton, Canada.

Table 3.1. Measured peak temperature T_{peak} and corresponding time t_{peak} of thermocouple 1.

	t_h (s)	T_{peak} (°C)	t_{peak} (s)
15	Test I	145.3	41.5
	Test II	144.7	41.5
	Test III	141.7	46.0
	Discrepancy (%)	2.54%	10.80%
20	Test I	187.7	42.0
	Test II	190.0	45.5
	Test III	187.3	46.0
	Discrepancy (%)	1.44%	9.52%
25	Test I	228.0	48.5
	Test II	229.5	53.0
	Test III	232.4	47.5
	Discrepancy (%)	1.93%	11.60%

Table 3.2. Calculated induction heat flux q''_{ind} (MW/m²)

	t_h (s)	Test I	Test II	Test III	Average	Discrepancy (%)
Thermocouple 1	25	1.120	1.107	1.132	1.120	2.29%
	20	1.098	1.112	1.099	1.103	1.32%
	15	1.058	1.076	1.081	1.071	2.14%
Thermocouple 2	25	1.155	1.146	1.171	1.157	2.14%
	20	1.139	1.144	1.135	1.139	0.84%
	15	1.094	1.101	1.117	1.104	2.07%
Thermocouple 3	25	1.089	1.102	1.123	1.105	3.12%
	20	1.047	1.072	1.070	1.063	2.34%
	15	1.034	1.063	1.033	1.043	2.97%
Thermocouple 4	25	1.120	1.148	1.134	1.134	2.49%
	20	1.071	1.085	1.060	1.072	2.40%
	15	1.028	1.120	1.016	1.055	10.23%
Discrepancy of average induction heat flux	25				4.71%	
	20				7.15%	
	15				5.85%	

Table 3.3. Influence of the uncertainties of B and ϵ on the heat flux q''_{ind} (MW/m²)

	$B = 0.9 \text{ W/m}^2 \cdot \text{K}^{1.25}$		$B = 1.8 \text{ W/m}^2 \cdot \text{K}^{1.25}$		$B = 2.7 \text{ W/m}^2 \cdot \text{K}^{1.25}$	
	q''_{ind}	Discrepancy*	q''_{ind}	Discrepancy*	q''_{ind}	Discrepancy*
$\epsilon = 0.4$	1.100	-1.54%	1.100	-1.54%	1.104	-1.21%
$\epsilon = 0.7$	1.105	-1.11%	1.117	--	1.130	1.12%
$\epsilon = 1.0$	1.131	1.25%	1.144	2.41%	1.157	3.59%

*: based on the deviation from the nominal q''_{ind} with $B = 1.8 \text{ W/m}^2 \cdot \text{K}^{1.25}$ and $\epsilon = 0.7$.

Table 3.4. Comparison of finite difference nodal temperature and the finite element analyzed average temperature of the cross-section.

t (s)	Cross-section, x (mm)	Finite difference cross-section nodal temperature ($^{\circ}\text{C}$)	FEM average temperature ($^{\circ}\text{C}$)	Discrepancy	
				ΔT ($^{\circ}\text{C}$)	(%)
15.0	0	538.2	532.1	6.1	1.13%
	5.6	446.6	438.0	8.6	1.93%
	30	68.1	66.4	1.7	2.50%
20.0	0	635.2	627.9	7.3	1.15%
	5.6	537.6	527.1	10.5	1.95%
	30	101.2	97.7	3.5	3.46%
25.0	0	720.1	713.7	6.4	0.89%
	5.6	617.9	607.3	10.4	1.68%
	30	136.5	131.0	5.5	4.03%

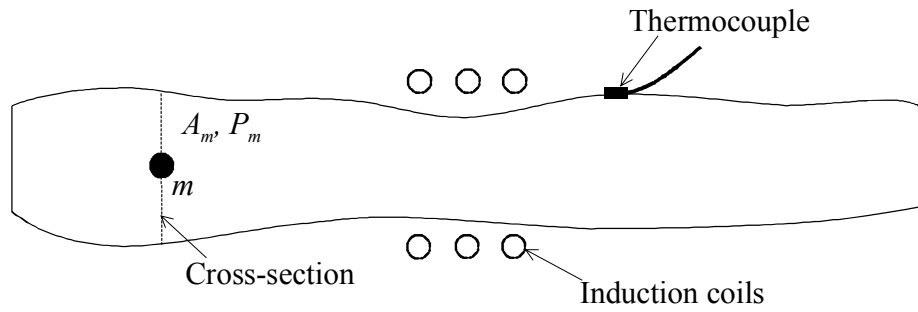


Fig. 3.1. Configuration of the induction heating a long workpiece and the cross-section represented by a node m with area A_m and perimeter P_m .

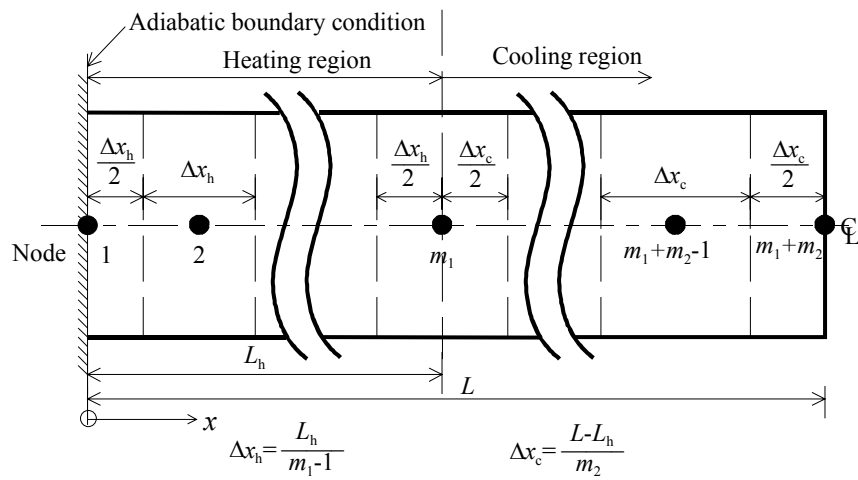


Fig. 3.2. Finite difference model and nodal points in a half rod.

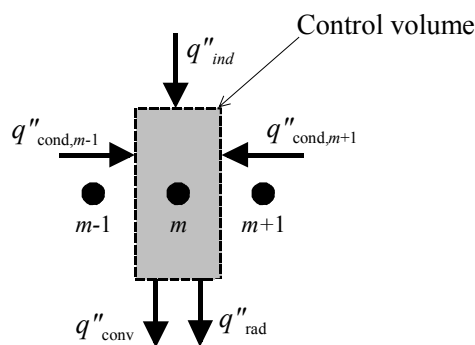


Fig. 3.3. Control volume at node m and the sources of heat flux.

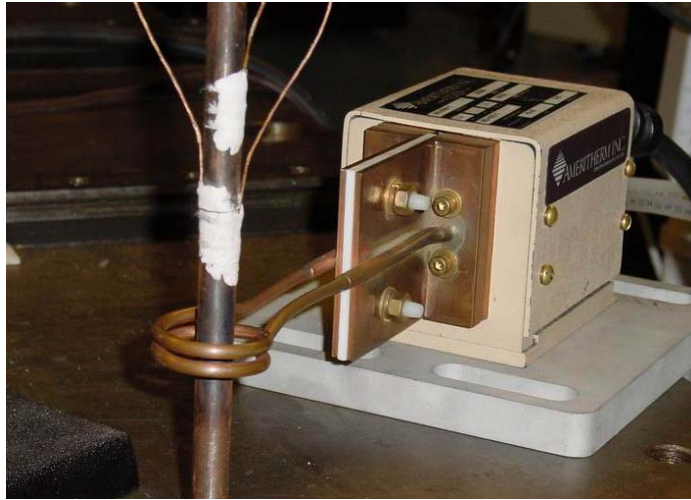


Fig. 3.4. Setup of rod workpiece, water-cooled induction heating coil, and thermocouples.

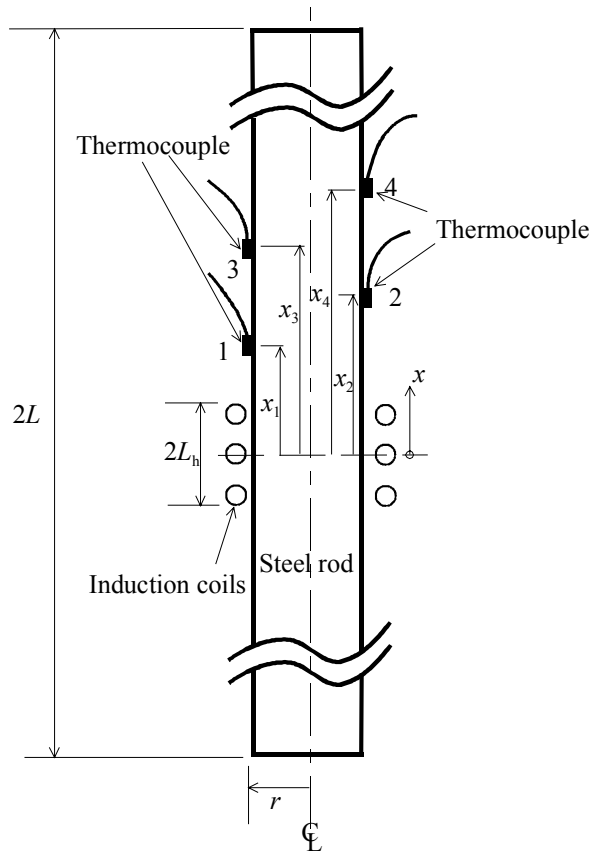


Fig. 3.5. Configuration of the induction heating experiment of the rod workpiece and thermocouple locations.

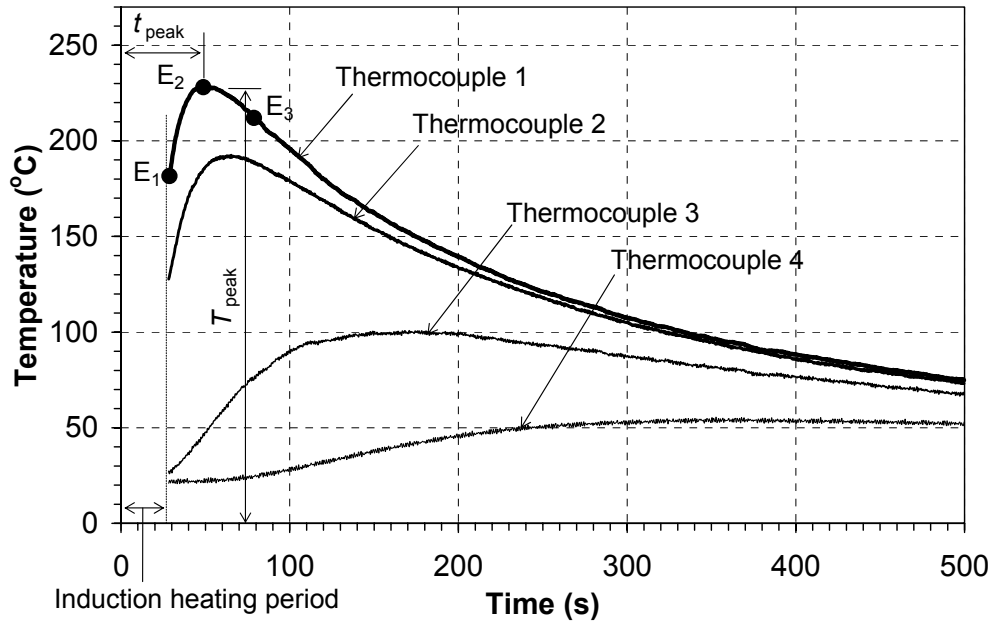


Fig. 3.6. Experimentally measured temperatures at four thermocouples for $t_h = 25$ s and the selection of data points for inverse heating transfer solution of induction heat flux.

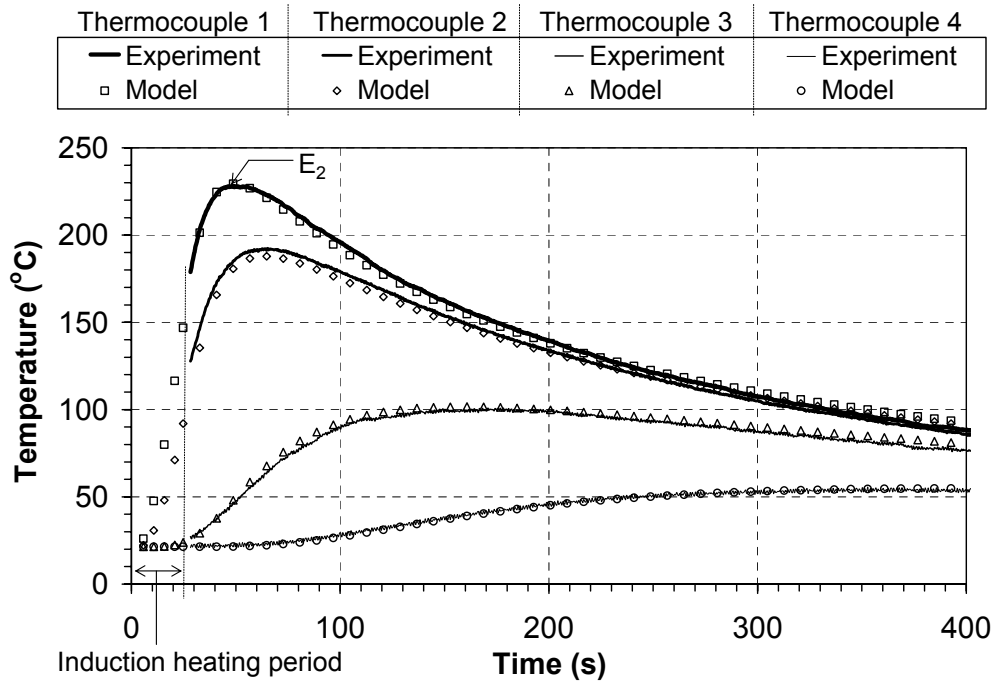


Fig. 3.7. Comparison of the measured and calculated temperature for $t_h = 25$ s.

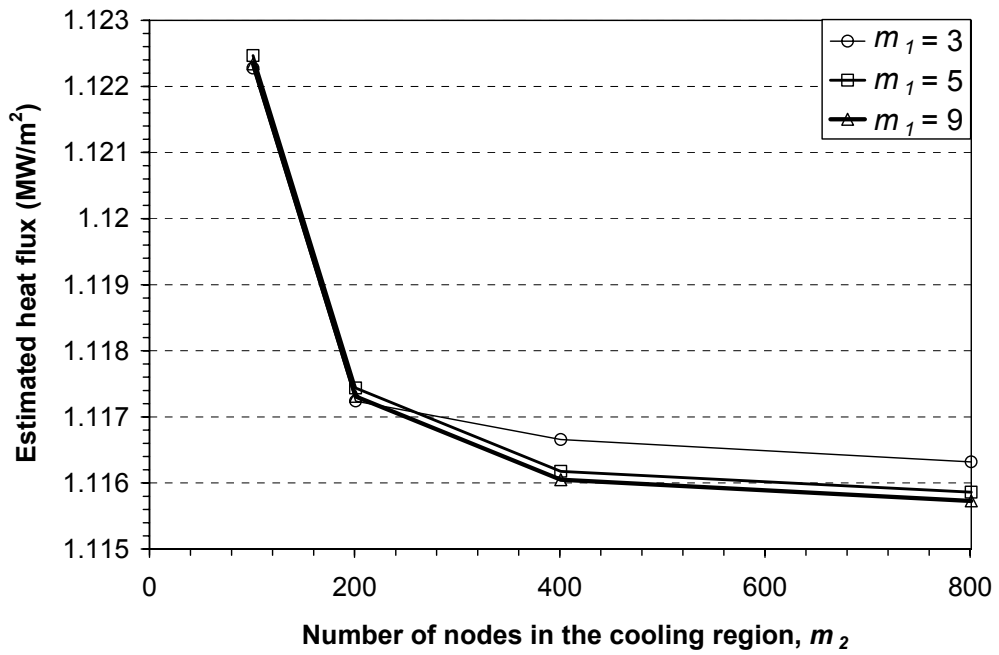


Fig. 3.8. Effect of grid spacing on the surface heat flux q''_{ind} .

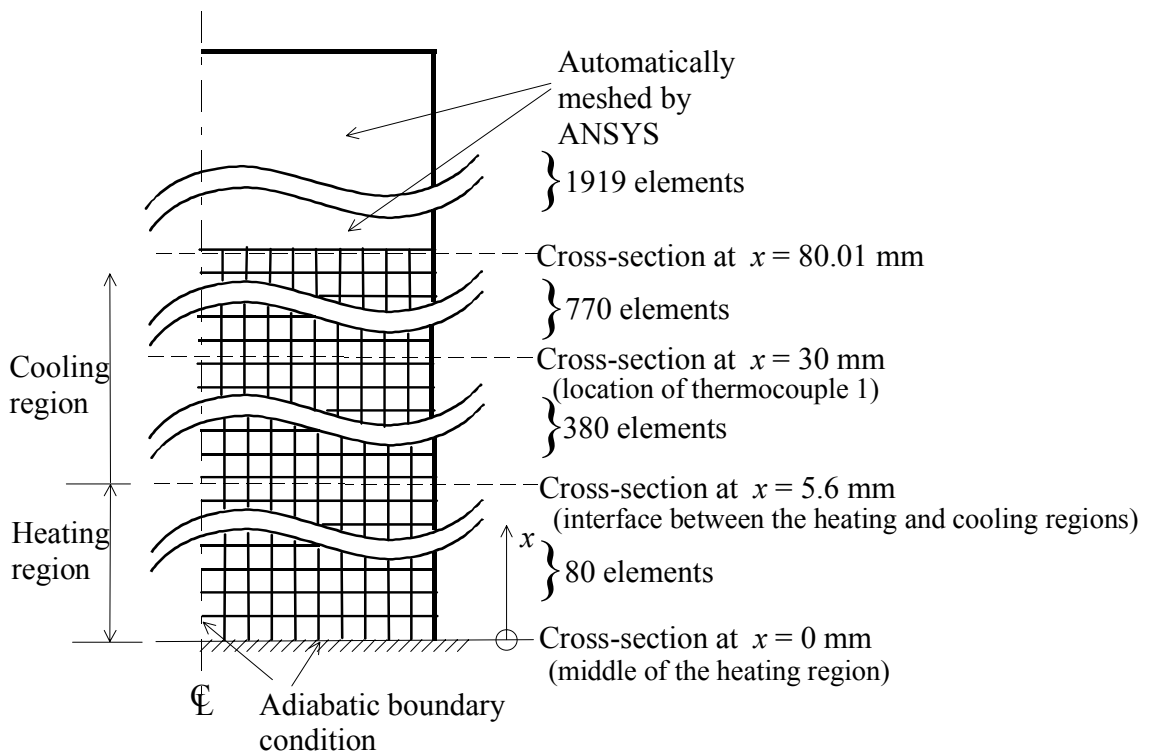


Fig. 3.9. FEM mesh and the three cross-sections.

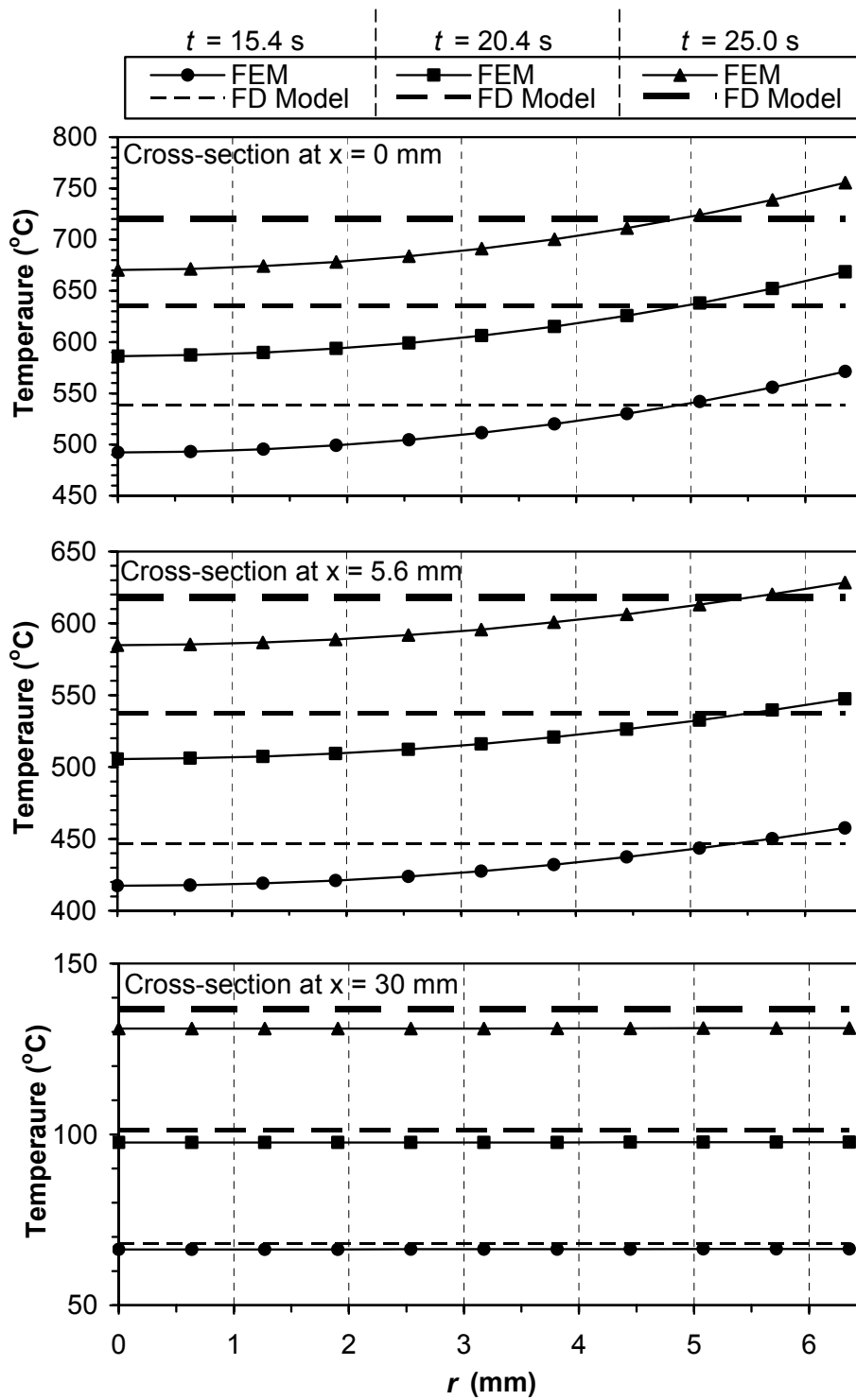


Fig. 3.10. Comparison of the finite element and finite difference analysis results for $t_h = 25$ s at three cross-sections.

CHAPTER 4.

DIFFERENCE THERMAL MODELING AND EXPERIMENTAL VALIDATION OF INDUCTION-HEATED TOOL

4.1. Introduction

Elastomers have the unique material properties of very low elastic modulus and high percentage of elongation before fracture. These properties make the effective material removal and precision machining of elastomers a technical challenge. The early research in elastomer machining was conducted by Jin and Murakawa [1]. Benefits of the high speed and high tool helix and rake angles to enable the efficient machining of elastomers were demonstrated. Elastomer machining using sharp woodworking tools and the effect of cryogenically cooled elastomer workpiece were investigated by Shih et al. [2]. With proper selection of tool geometry, process parameters, and fixture stiffness, effective material removal and generation of clean grooves in end milling were demonstrated. The investigation showed that the down-cut tool, good fixturing, and cryogenic cooling of the workpiece are beneficial for machining of elastomers.

A novel method using the induction-heating of the rotary tool is developed for machining of elastomers. This idea originates from the current practice of manual carving the tread for prototype tire manufacturing. A thin, sharp, and resistance-heated grooving blade is used for this operation. Heating the tool is critical. If the tool is not heated to a certain temperature, carvers are not able to cut grooves on the tire. The heat softens the elastomer materials ahead of the tool and allows it to penetrate the workpiece efficiently. In this chapter, induction heating is used to raise the temperature of a rotary tool. Experiments of heating the stationary and rotary tool are performed to investigate the effect of rotation on tool tip temperature for machining of elastomers. The finite

difference thermal model, developed in Chapter 3, is expanded to include the thermal insulator and applied to predict the temperature of induction-heated tool.

The induction heating experiment setup and test procedure are presented in following section. Experimental results are summarized in Sec. 4.3. The finite difference thermal modeling of the induction-heated tool and insulator is presented in Sec. 4.4. In Sec. 4.5, the modeling and experimental results are compared.

4.2. Experimental setup and test procedure

The configuration of induction-heated tool for machining of elastomers is shown in Fig. 4.1(a). The non-contact induction heating provides a fast, consistent heating to a specific region adjacent to the cutting flute. As shown in Fig. 4.1, a thermal insulator, made of low thermal conductivity Ti-6Al-4V, is used to reduce the heat transfer to the spindle.

Three sets of experiments, marked as Experiment A, B, and C, are performed to calibrate the contact thermocouple for the tool tip temperature measurement, study the effect of tool rotation on induction heat generation and convective heat transfer, and measure the tool temperature distribution for finite difference inverse heat transfer solution and validation of modeling results, respectively.

4.2.1. Experiment A

The goal of Experiment A is to calibrate the temperature measured by the contact and cement-on thermocouples. The contact thermocouple is used to quickly touch and measure the tool tip temperature after stopping the rotating tool. The tool tip temperature is an important process parameter for heated tool machining of elastomers. A slip ring can be used to transmit the voltage signal of thermocouples attached to the tool tip [3]. However, the thermocouple wire needs to route from the tool tip, through the heating coil to the slip ring near the spindle. Such configuration is not possible due to the heating of thermocouple wire inside the induction heating coil. In this chapter, a contact thermocouple (Omega type KMQIN-062E-6) with 0.7 mm diameter miniature tip is selected. The discrepancy between the contact and cement-on thermocouple

measurements does exist and requires a set of experiments to identify the calibration curve.

Fig. 4.2 shows the configuration of Experiment A. The tool is stationary and a cement-on thermocouple is attached to the tool tip. The double-flute, down-cut tool (Onsrud 40-series) with the same cutting edge geometry as the router tool with good performance for effective material removal in [2] is used. To adopt for induction heating, this new tool, as shown in Figs. 4.1(b) and 4.2, has a longer overall length of 127 mm and shorter flute length of 31 mm.

A type K cement-on thermocouple (Omega type CO1-K) is attached to the tool tip. The close-up view of the tool tip is shown in Fig. 4.3. Temperatures at the tip of the induction-heated stationary tool are measured simultaneously by the cement-on and contact thermocouples. As shown in Fig. 4.3(a), there are two symmetric surfaces, marked as Surfaces 1 and 2, at the tip of the double-flute tool. Due to the symmetry, temperatures on Surfaces 1 and 2 are expected to be the same. As shown in Fig. 4.3(b), a cement-on thermocouple is attached to Surface 1, while the contact thermocouple touches Surface 2. Three tests with the same duration of induction heating time, 10 s, and three induction heating power levels at 0.4, 0.5, and 0.7 kW were conducted to measure temperatures on Surfaces 1 and 2 simultaneously. Voltage signals from the cement-on and contact thermocouples are acquired using a PC-based data acquisition system with the 250 Hz sampling rate. The temperature data is averaged and recorded every 0.5 s. This temperature data-acquisition setup is also used for all tool heating experiments.

4.2.2. Experiment B

Experiment B studies the effect of tool rotation on heat transfer in the induction-heated tool. The tool was vertically held to the spindle of a vertical end milling machine. Tests were performed at 0 (stationary), 1100, 2000, and 2900 rpm to study the effect of spindle speed on the induction heat generation and convective heat transfer. Low spindle speeds are used for elastomer machining to avoid chip burning, which will be discussed in Chapter 5. The induction heating duration was 25 s and power level was about 0.7 kW for all tests. The induction coil was positioned in the flutes section at the tool tip. As shown in Fig. 4.2, a coordinate system with x -axis measuring from the tool tip in the

direction toward the spindle is defined. The position of heating region in the tool or the location of the induction coil is denoted as x_{IC} . In Experiment B, $x_{IC} = 0$ mm.

Process parameters in Experiment B are summarized in Table 4.1. A baseline test was first performed when the tool is stationary. The contact thermocouple recorded the tool tip temperature after the 25 s induction heating. Under the same setting of induction heating, three tests were conducted at 1100, 2000, and 2900 rpm to study the effects of tool rotation on induction heat generation rate. The rotating tool is quickly stopped 25, 50, and 100 s after the 25 s of induction heating. The contact thermocouple then touches the tool tip and measures the temperature. The calibration data in Experiment A is used to convert the measured temperature to tool tip temperature.

The effect of tool rotation on convective heat transfer is studied by comparing the tool tip temperature at different time durations (25, 50, and 100 s) of rotation. The induction heating time remains unchanged at 25 s. The change in temperature qualitatively reveals the increase in heat convection coefficient of a rotating tool.

4.2.3. Experiment C

The temperature distribution of the induction-heated stationary tool was measured in Experiment C. The experimental setup and configuration are shown in Figs. 4.4 and 4.5. Two type K thermocouples, marked as Thermocouples 1 and 2 with location x_1 and x_2 from the tool tip, respectively, were cemented on the tool. In this experimental setup, $x_1 = 79$ mm and $x_2 = 3$ mm. The induction heating duration was 10 s.

During the induction heating, the thermocouple temperature measurement is not possible due to the interference of electromagnetic field generated by the induction heating coil. The peak temperature of a thermocouple is used as the input for the inverse heat transfer solution based on the finite difference thermal modeling to find the induction heat generation rate. Experimental results are also used to validate temperature distribution estimated by the finite difference modeling.

4.3. Results of tool induction heating experiments

4.3.1. Results of Experiment A - calibration of contact thermocouple

Fig. 4.6 shows the calibration results of Experiment A. For all three tests, represented by different symbols, the contact thermocouple temperature, T_h , is lower than the cement-on thermocouple temperature, T_c . All data points show a linear trend. The regression analysis is used to find a line to model the relationship between T_h and T_c .

$$T_c = 1.70T_h - 0.97 \quad (4.1)$$

The T_c is about 1.7 times the T_h . The discrepancy between T_h and T_c is likely due to the combination of the following three reasons.

1. Thermal contact resistance: Thermal contact resistance [4] is determined by the contact area between the thermocouple tip and the tool. For the cement-on thermocouple, the 2.5 mm by 3 mm area of the tip fully contacts with the tool. For the contact thermocouple, only a small region of the 0.7 mm diameter spherical tip touches the tool. The contact area of the contact thermocouple tip is much smaller and the thermal contact resistance is higher.
2. Heat loss from the thermocouple tip to the ambient air: As shown in Fig. 4.3(b), the cement-on thermocouple tip is covered by a layer of cement with thermal conductivity of 1.15 W/m·K. The contact thermocouple tip is exposed directly to the ambient air and results in higher temperature gradient and more heat loss.
3. Uncertainty of contact position between the thermocouple tip and the tool: The variation of contact point on Surface 2, as shown in Fig. 4.3, during the experiment also contributes to the temperature variation.

Equation (4.1) is used to convert measured temperatures in Experiments B.

4.3.2. Results of Experiment B - effect of tool rotation

Results of Experiment B are shown in Fig. 4.7. The measured temperature of the stationary tool is the baseline data. During the 25 s heating duration, the electromagnetic

interference makes the thermocouple temperature measurement impossible. The measured temperatures are shown for t after 30 s. The time, t , is measured from the start of induction heating. It takes about 5 s from the end of induction heating for the contact thermocouple to touch the tool tip for temperature measurement.

For the stationary tool, as shown in Fig. 4.7, the temperature rapidly rises to 420°C shortly after the contact thermocouple touched the tool tip at $t = 30$ s.

At 1100 rpm, measured temperatures of the tool with the 25 s rotational time match closely with the stationary tool heated under the same induction heating setup. This indicates that the influence of tool rotation on induction heat generation and convective heat transfer is not significant. The lag time to reach the peak temperature is longer for tests with the rotating tool than the stationary tool. It is due to the time required to stop the tool and apply the contact thermocouple to touch the tool tip.

The same trend can be observed at 2000 rpm. The tool rotation does not significantly affect the induction heat generation and convective heat transfer.

At 2900 rpm, as shown in Fig. 4.7, the effect of the tool rotation on convective heat transfer can be recognized. A larger discrepancy of temperatures between the stationary tool and rotating tool can be seen. Such discrepancy is due to the higher convection coefficient caused by a faster tool rotational speed.

The effect of the duration of tool rotation on increasing the temperature discrepancy relative to the stationary tool can also be identified in Fig. 4.7.

4.3.3. Results of Experiment C – induction heating of a stationary tool

Fig. 4.8 shows measured temperatures at Thermocouples 1 and 2 from 0 to 200 s in Experiment C. The duration of induction heating is 10 s. The heat generated by induction heating transfers like a thermal wave from the heating region toward both sides of the tool. Thermocouple 2 is closer to the induction heating region than Thermocouple 1. Therefore, Thermocouple 2 has shorter time (83 s) to achieve higher peak temperature (168°C), marked as point P in Fig. 4.8. The peak temperature of Thermocouple 1, denoted as point S (100 s, 86°C), is used as the input for the inverse heat transfer solution of the heat flux generated by induction heating. The results of inverse heat transfer

solution and analysis of the temperature distribution of the tool will be discussed in Sec. 4.4.3.

4.4. Finite difference thermal modeling of an induction-heated tool

Explicit finite difference method is applied to model the tool temperature distribution with the thermal insulator and to estimate the surface heat flux, q''_{ind} , generated by induction heating. The finite difference thermal model, modeling results of a stationary tool, and comparison of the experimental and modeling results are discussed in the following sections.

4.4.1. Finite difference thermal model

The explicit finite difference formulation of an inverse heat transfer model to calculate the induction heat flux for a workpiece with the cross-section Biot number less than 0.1 has been developed in Chapter 3. Under small Biot number, the temperature in the cross-section is almost uniform. A single value can be used to represent the temperature of the cross-section in the finite difference formulation to solve the induction heat flux using the inverse heat transfer solution and to analyze the temperature distribution during heating and cooling. As shown in Fig. 4.5, the radius of the tool, r , is 6.35 mm. The width of the thermal insulator, w , is 4.75 mm. The tool material is M7 high speed steel with thermal conductivity (k) of 19.0 W/m·K [5]. The Ti-6Al-4V thermal insulator has thermal conductivity (k_s) of 6.6 W/m·K [6]. The Biot numbers of the tool and thermal insulator cross-sections are 0.0045 and 0.0049, respectively, under the convection coefficient of 6.8 W/m²·K, which is discussed in Chapter 3. These Biot numbers are both much smaller than 0.1. In this chapter, the finite difference method is further expanded to investigate the heat transfer in the tool with a thermal insulator.

As shown in Fig. 4.5, the tool is divided to three types of regions: insulation, heating, and cooling. The insulation region is represented by line ab with length L_{ins} . The heating region is represented by line cd with length L_h . Four cooling regions, marked as 1, 2, 3, and 4, have length L_{c1} , L_{c2} , L_{c3} , and L_{c4} , respectively. The cylindrical section of the tool, line ae , has a constant cross-section area A_b and perimeter P_b . The

flutes section of the tool, line eg , is further divided into the cooling region 3 (line ef) and cooling region 4 (line fg). The cooling region 4 has the constant cross-section area A_t and perimeter P_t . Cooling region 3 is a geometrical transition section. The cross-section area and perimeter are assumed to vary linearly from A_b and P_b to A_t and P_t , respectively.

4.4.1.1. Nodes in the heating region

Based on the energy balance method, explicit finite difference equations are developed for nodes in the heating region. As shown in Fig. 4.9(a), the tool is modeled as a line of series nodes. At node m , the control volume, cross-section area, and perimeter of the tool are V_m , A_m , and P_m , respectively. The energy exchange in control volume V_m is determined by the conduction between the node m and adjacent nodes $m-1$ and $m+1$ in the axial direction and the convection, radiation, and induction heat generation on the peripheral surface $P_m\Delta x$, where Δx is the width of the control volume. The conduction heat flux from node $m-1$ to m and from node $m+1$ to m in the axial direction is represented by $q''_{ca,m-1}$ and $q''_{ca,m+1}$, respectively. The symbol a in $q''_{ca,m-1}$ and $q''_{ca,m+1}$ indicates the heat flux in the axial direction. The convection and radiation heat flux on the peripheral surface of the control volume at node m is q''_{conv} and q''_{rad} , respectively. q''_{conv} and q''_{rad} can be calculated by the formulas described in Chapter 3. During induction heating, a uniform heat flux q''_{ind} is applied on the peripheral surface of the heating region. The energy balance equation of the control volume at node m is:

$$(q''_{ca,m-1} + q''_{ca,m+1}) \cdot A_m + (q''_{ind} - q''_{conv} - q''_{rad}) \cdot P_m \cdot \Delta x = \rho c \cdot A_m \Delta x \cdot \frac{T_m^{p+1} - T_m^p}{\Delta t} \quad (4.2)$$

where ρ and c are the density and specific heat of the tool material, respectively, Δt is the time increment, and T_m^p is the nodal temperature at node m and time step p .

4.4.1.2. Nodes in the cooling region

Eq. (4.2) with $q''_{ind} = 0$ is the energy balance equation for nodes in the cooling region.

4.4.1.3. Nodes in the insulation region

As shown in Figs. 4.9(b) and 4.9(c), the heat transfer in the insulation region is conducted in both axial and radial directions. The energy balance analysis is performed for node m in the tool and node m_s in the thermal insulator.

At node m in the tool, the energy exchange in control volume V_m , as shown in Fig. 4.9(b), is determined by the conduction between node m and adjacent nodes $m-1$, $m+1$, and m_s , marked as $q''_{ca,m-1}$, $q''_{ca,m+1}$, and $q''_{cr,m}$, respectively. $q''_{cr,m}$ is conducted in the radial direction, from node m to m_s , through the contact area $P_m \Delta x$ between the tool and the thermal insulator. The $q''_{cr,m}$ can be expressed as [4]:

$$q''_{cr,m} = \frac{2 \cdot (T_m^p - T_{m_s}^p) \cdot \pi \cdot \Delta x}{(\ln 2/k + \ln(\frac{P_m + P_{m_s}}{2P_m}) / k_s)} \quad (4.3)$$

where $T_{m_s}^p$ is the nodal temperature at node m_s and time step p .

The energy balance of the control volume V_m at node m is:

$$(q''_{ca,m-1} + q''_{ca,m+1}) \cdot A_m - q''_{cr,m} \cdot P_m \cdot \Delta x = \rho c \cdot A_m \Delta x \cdot \frac{T_m^{p+1} - T_m^p}{\Delta t} \quad (4.4)$$

At node m_s in the thermal insulator, as shown in Fig. 4.9(c), the energy exchange in the control volume V_{m_s} is determined by the conduction between the node m_s and adjacent nodes m_s-1 , m_s+1 , and m , marked as q''_{ca,m_s-1} , q''_{ca,m_s+1} , and $q''_{cr,m}$, respectively, and the conduction between the node m_s and surrounding surface, marked as q''_{cr,m_s} . For $q''_{cr,m}$ and q''_{cr,m_s} , the symbol r indicates the heat flux in the radial direction. The heat flux q''_{cr,m_s} is conducted through the contact area $P_{m_s} \Delta x$ between the thermal insulator and the surrounding surface, where P_{m_s} is the outer perimeter and Δx is the width of the control volume V_{m_s} at node m_s . The q''_{cr,m_s} is determined by the boundary condition on the contact area $P_{m_s} \Delta x$.

The boundary condition on the interface between tool and insulator is difficult to clearly define. Two boundary conditions, representing two extreme cases, are studied. One boundary condition assumes constant temperature (isothermal) and the other hypothesizes no heat flux (adiabatic) across the boundary.

If the contact surface remains at its initial temperature, T_{sp} , during the heating and cooling stage, the heat flux $q''_{cr,ms}$ is:

$$q''_{cr,ms} = \frac{2\pi \cdot (T_{ms}^p - T_{sp}) \cdot \Delta x \cdot k_s}{\ln\left(\frac{2P_{ms}}{P_m + P_{ms}}\right)} \quad (4.5)$$

For the adiabatic boundary condition, which assumes that the thermal insulator is a perfect insulator, $q''_{cr,ms} = 0$.

The energy balance of the control volume V_{ms} at node m_s is:

$$(q''_{ca,ms-1} + q''_{ca,ms+1}) \cdot A_{ms} + (q''_{cr,m} \cdot P_m - q''_{cr,ms} \cdot P_{ms}) \cdot \Delta x = \rho_s c_s \cdot A_{ms} \Delta x \cdot \frac{T_{ms}^{p+1} - T_{ms}^p}{\Delta t} \quad (4.6)$$

where ρ_s is the density and c_s is specific heat of the thermal insulator and A_{ms} is the cross-section area at node m_s .

4.4.2. Modeling results of the stationary tool

The induction heat flux q''_{ind} is solved by minimizing an objective function, which is the square of the discrepancy between the experimental measurement (point S in Fig. 4.8) and modeling result described in Chapter 3. In the experimental configuration shown in Fig. 4.5, the position of heating region $x_{IC} = 33.0$ mm. The length of region, $L_{c1} = 47.7$ mm, $L_{c2} = 2.0$ mm, $L_{c3} = 17.0$ mm, $L_{c4} = 14.0$ mm, $L_h = 11.3$ mm, and $L_{ins} = 35.0$ mm. The grid with 24, 1, 9, 7, 6, and 19 nodes is assigned in cooling regions 1, 2, 3, and 4, heating region, and insulation region, respectively. The grid spacing is about 2 mm in

all regions. For the tool used in this chapter, $P_b = 40$ mm, $P_t = 34$ mm, $A_b = 127$ mm², and $A_t = 71$ mm².

The experimentally measured temperature, thermocouple location, and material properties of the tool and thermal insulator are required inputs for the finite difference modeling. For the M7 high speed steel used for the tool, $\rho = 7950$ kg/m³ and $c = 460$ J/kg·K [5]. For the Ti-6Al-4V used for the sleeve, $\rho_s = 4428$ kg/m³ and $c_s = 580$ J/kg·K [6]. The peak temperature at Thermocouple 1, point S in Fig. 4.8 (100 s, 86.4°C), and the location of thermocouple 1, $x_1 = 79$ mm, are used as the input for the finite difference inverse heat transfer solution. The calculated q''_{ind} is 1.508 MW/m² under the isothermal boundary condition and 1.442 MW/m² under the adiabatic boundary condition. These two values are the upper and lower bounds for the estimated induction heat flux corresponding to two extreme boundary conditions on the contact area between the thermal insulator and surrounding surface. The adiabatic boundary condition assumes no heat loss through the boundary and results a higher tool temperature of two boundary conditions with the same induction heat flux in the heating region. Therefore, with the same temperature at Thermocouple 1 as the input for the inverse heat transfer solution, the isothermal boundary condition generates a larger estimated q''_{ind} than the adiabatic boundary condition.

4.4.3. Comparison of the experimental and modeling results

Based on two estimated values of induction heat flux q''_{ind} , two sets of temporal and spatial distribution of temperature on the tool are calculated. Results of finite difference modeling and experimental measurements at Thermocouples 1 and 2 are illustrated in Fig. 4.8. As expected, the experimental measurement and finite difference modeling temperatures match at point S, the input for the finite difference inverse heat transfer solution. The finite difference modeling is able to predict the temperature during the induction heating period ($0 < t < 10$ s). In this period, the temperature at thermocouple cannot be experimentally measured due to the electromagnetic interference. When $0 < t < 40$ s, the discrepancy between the finite difference modeling results under adiabatic and isothermal boundary conditions is negligible. The heat flux

across the insulation region is still small. Therefore, the effect of boundary condition on the temperatures at Thermocouples 1 and 2 is not significant. When $t > 40$ s, the effect of the boundary condition becomes more apparent.

At Thermocouple 1, when $40 < t < 100$ s, the estimated temperature under isothermal boundary condition is higher than that of adiabatic boundary condition due to the larger estimated induction heat flux q''_{ind} in the heating region. q''_{ind} is the input for the temperature distribution analysis of the finite difference modeling. However, when $t > 100$ s, the estimated temperature under isothermal boundary condition is lower than that under the adiabatic boundary condition. This is due to the effect that the heat loss conducted between thermal insulator and surrounding surface surpasses the influence of higher estimated induction heat flux.

At Thermocouple 2, when $t > 40$ s, the estimated temperature under isothermal boundary condition is always higher than that under the adiabatic boundary condition. This is due to the larger estimated q''_{ind} for isothermal boundary condition. Because Thermocouple 1 is much closer to the insulation region (Fig. 4.5), the effect of boundary conditions on the temperature at Thermocouple 2 is less significant than at Thermocouple 1.

At Thermocouple 2, the discrepancy between the experimental measurements and finite difference modeling is generally larger than at Thermocouple 1. The experiment shows the peak temperature at the tool tip (Thermocouple 2) occurs at 83 s. The finite difference modeling predicts the peak temperature at about 105 to 110 s. The geometry approximation of the complex flutes section and the use of constant thermal properties both contribute to this discrepancy. However, the experimentally measured peak temperature at Thermocouple 2, 168°C , is still close to the peak temperature range (162°C , 167°C) estimated by the finite difference modeling.

Experiment C described in Sec. 4.2.3 is conducted several times with different power settings. For each time, the induction heat flux is estimated by the inverse heat transfer solution and the temperature distribution and history are analyzed by the finite difference modeling. The estimated peak temperature range at Thermocouple 2 matches the experimental temperature measurement, which demonstrates the capability of the

finite difference thermal modeling to predict tool tip peak temperature. This is important to design the heating strategy for induction-heated tool machining of elastomers.

4.5. Conclusions

Experiments and finite difference modeling of the induction-heated tool was studied in this chapter. Experiments were conducted to study the heat generation and transfer in a rotating tool. A calibration line between temperatures measured by the cement-on and contact thermocouples was established. Tool rotation was illustrated to have insignificant effect on induction heat generation and convective heat transfer at spindle speed lower than 2000 rpm. In the following chapter the low spindle speed was adopted in the elastomer end milling experiments to avoid burning and smoking. Based on these observations, the temperatures of an induction-heated rotary tool could be estimated by the finite difference modeling of a stationary tool. The complete finite difference thermal modeling of the tool and insulator was developed to predict the tool temperature. Compared to the experimental measurements, the accuracy of predicted tool tip peak temperature was demonstrated.

More accurate finite difference modeling results can be achieved by applying better geometrical representation of the tool and using more accurate temperature-dependent properties of the tool material. Based on the finite difference thermal modeling developed in this chapter, the tool induction heating strategy can be developed for elastomer machining. Experimental results for elastomer machining tests are presented in the follow-up chapter.

References

- [1] Jin, M., and Murakawa, M., 1998, "High-Speed Milling of Rubber (1st Report) - Fundamental Experiments and Considerations for Improvement of Work Accuracy," *Journal of the Japan Society for Precision Engineering*, Vol. 64, No. 6, pp. 897-901.
- [2] Shih, A. J., Lewis, M. A., and Strenkowski, J. S., 2004, "End Milling of Elastomers – Fixture Design and Tool Effectiveness for Material Removal," *Journal of Manufacturing Science and Engineering*, Vol. 126, No. 1, pp. 115-123.
- [3] Bono, M., and Ni, J., 2002, "A Method for Measuring the Temperature Distribution along the Cutting Edges of a Drill," *Journal of Manufacturing Science and Engineering*, Vol. 124, No. 4, pp. 921-923.
- [4] Incropera, F. P., and Dewitt, D. P., 2002, *Fundamentals of Heat and Mass Transfer*, John Wiley & Sons, New York.
- [5] Tarney, E., 2003, Crucible Materials, *private communication*.
- [6] Boyer, R., Welsch, G., and Collings, E. W., 1994, *Materials Properties Handbook: Titanium Alloys*, ASM International, Materials Park, Ohio.

Table 4.1. Process parameters for Experiment B.

Spindle speed (rpm)	Heating duration t_h (s)	Duration of tool rotation (s)
0 (stationary)	25	0
1100	25	25, 50, 100
2000	25	25, 50, 100
2900	25	25, 50, 100

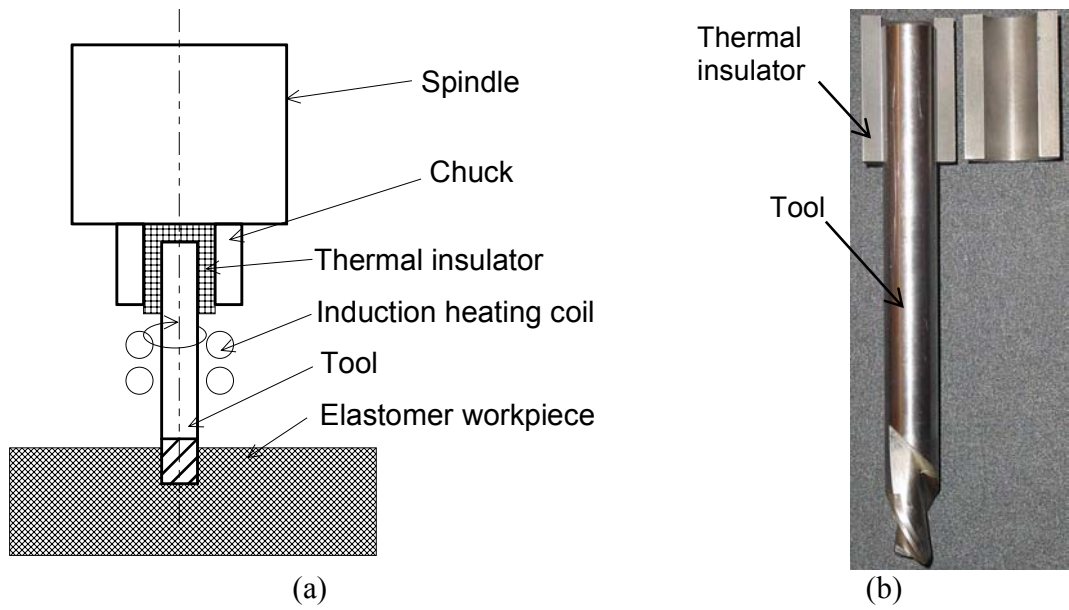


Fig. 4.1. (a) Induction-heated tool machining of elastomers and (b) the double-flute down-cut end mill and titanium thermal insulator.

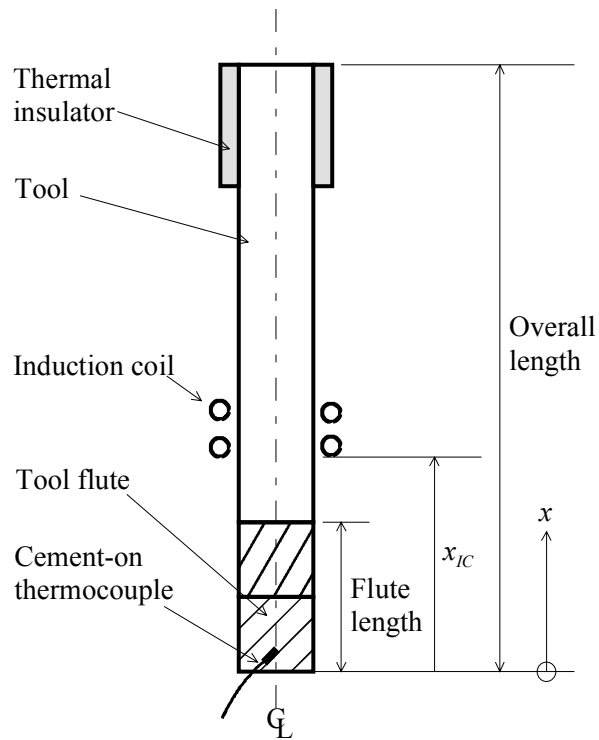


Fig. 4.2. Configuration of end mill, thermal insulator, water-cooled induction heating coil, and thermocouple.

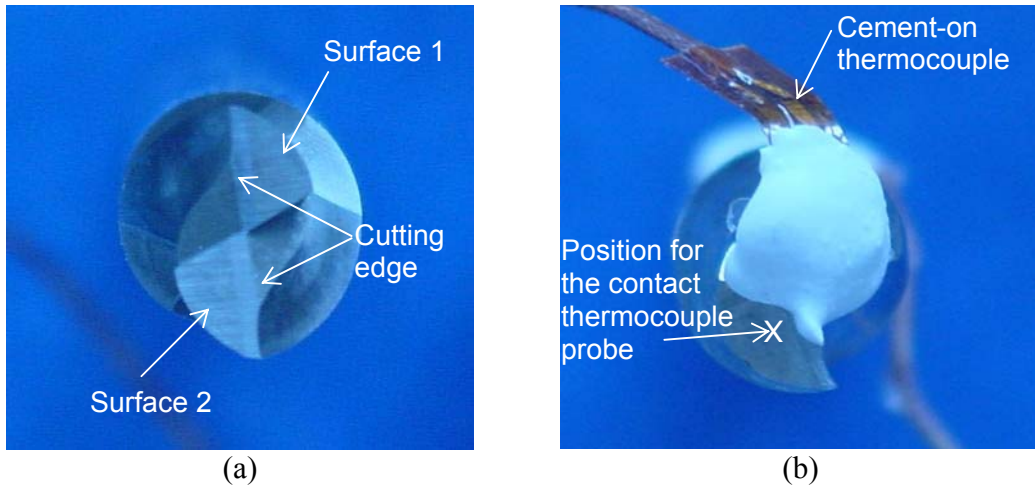


Fig. 4.3. Tool tip and thermocouple locations: (a) view of tool tip with two symmetric Surfaces 1 and 2, and (b) tool tip with the cement-on thermocouple attached to Surface 1 and the position for the contact thermocouple.

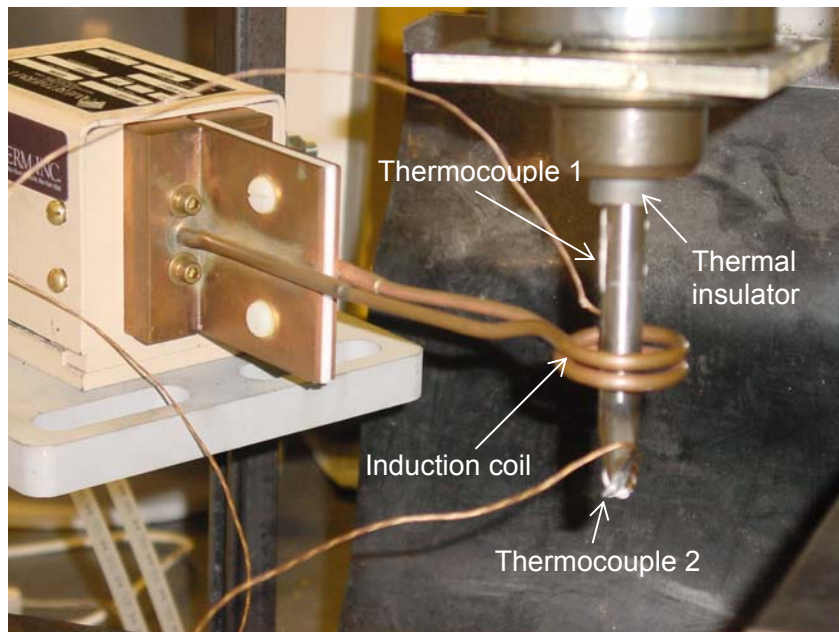


Fig. 4.4. Setup of tool, water-cooled induction heating coil, and thermocouples in Experiment C.

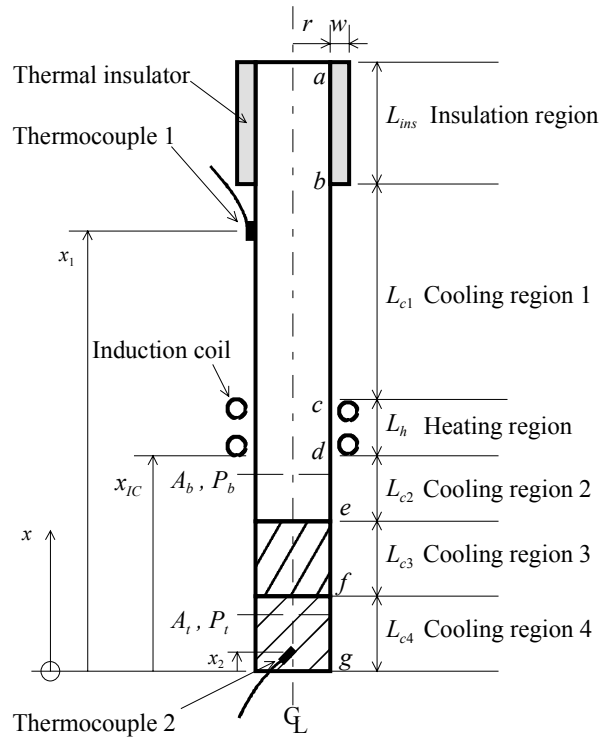


Fig. 4.5. Configuration of the induction heating in Experiment C.

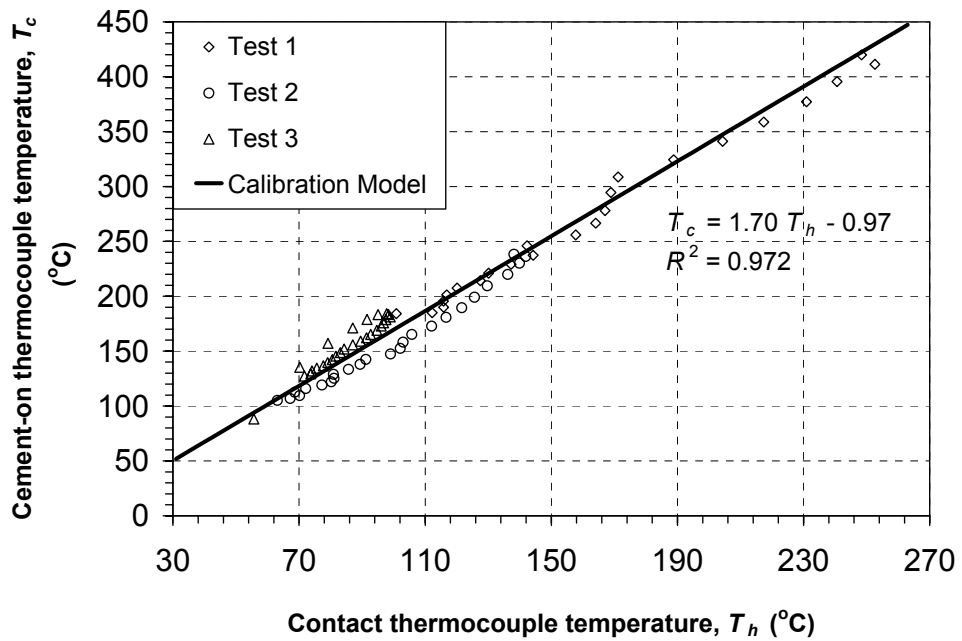


Fig. 4.6. Calibration for the contact thermocouple probe based on cement-on thermocouple.

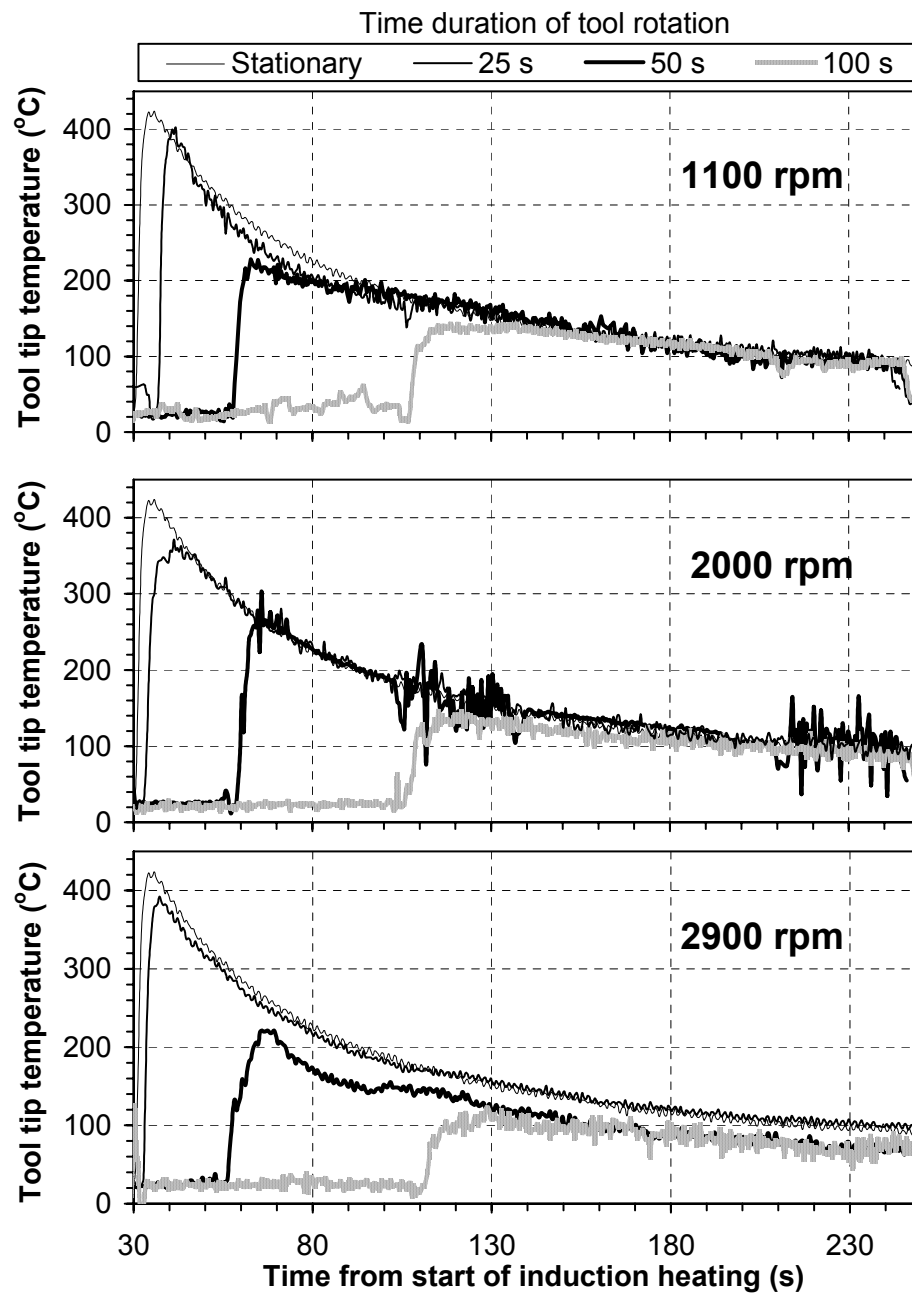


Fig. 4.7. Effect of tool rotation on the tool temperature (25 s duration of induction heating).

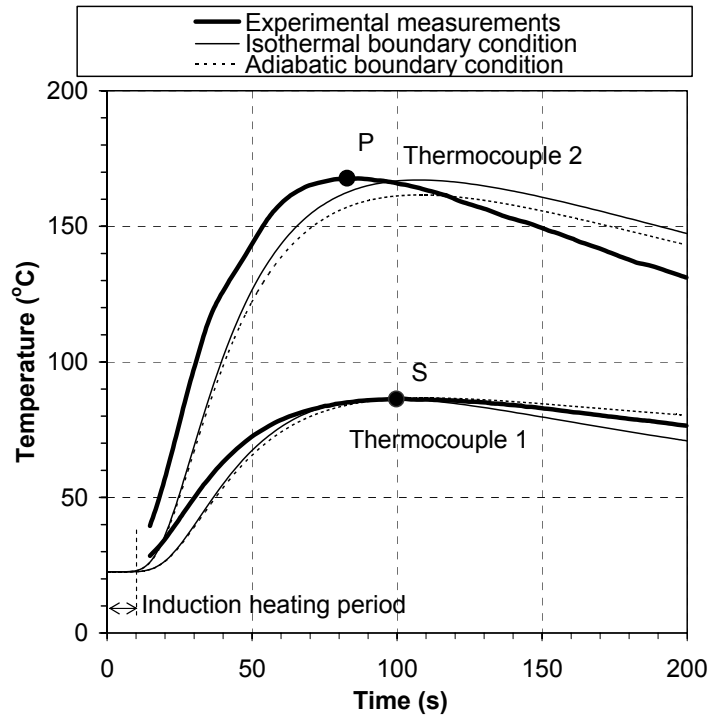


Fig. 4.8. Comparison of the measured and calculated temperature for heating duration as 10 s.

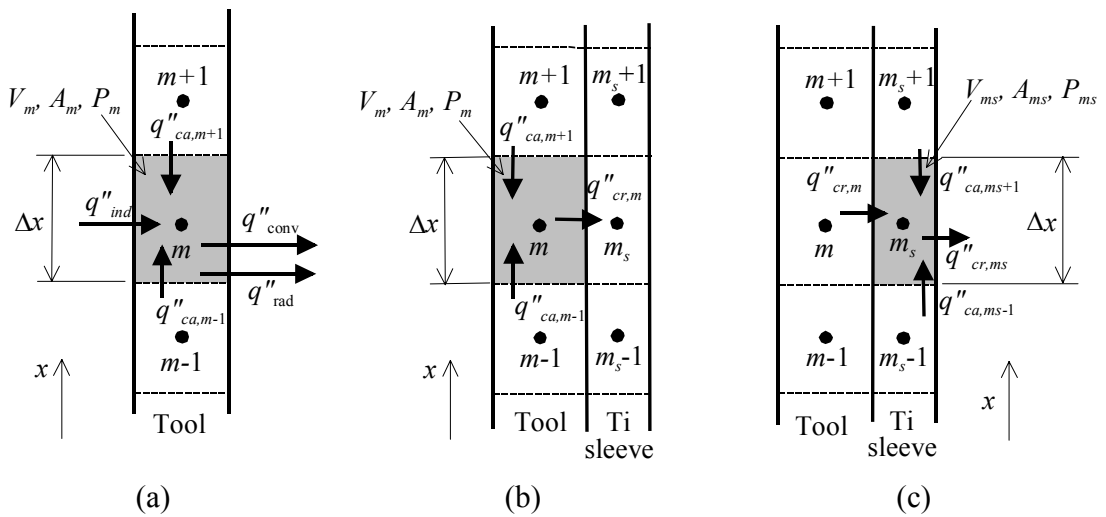


Fig. 4.9. Heat exchange between adjacent nodes in the tool and thermal insulator: (a) at node m in the heating region, (b) at node m in the insulation region, and (c) at node m_s in the insulation region.

CHAPTER 5.

CHIP MORPHOLOGY, CUTTING FORCES, AND MACHINED SURFACES IN INDUCTION-HEATED TOOL MACHINING OF ELASTOMERS

5.1. Introduction

Effective removal of the elastomer material by machining to generate the precise shape and good surface roughness of the workpiece is technically challenging due to the unique properties of very low elastic modulus and large elongation before fracture of work-material [1]. A series of elastomer end milling tests has been conducted and demonstrated benefits of the sharp, down-cut tool, cryogenically cooling the workpiece, and consistent workpiece fixturing on the effectiveness of work-material removal, chip morphology, and cutting forces [1,2]. Induction-heated tool described in Chapter 4 is a new approach that can potentially improve the precision and surface roughness for elastomer machining. High tool temperature can soften the elastomer workpiece in front of the cutting edge and may enable more effective tool penetration and chip formation.

Cutting speed is a key factor in elastomer machining. As observed by Jin and Murakawa [3], high cutting speed generates good surface roughness in elastomer machining. This observation is confirmed in this chapter. However, at high cutting speed, smoke is generated due to the burning of elastomer chips. It becomes an environmental and health hazard and limits the cutting speed in elastomer machining. Low but effective cutting speed is desirable for elastomer machining. Under this constraint, the induction-heated tool could be beneficial. In this chapter, effects of three key machining process parameters, the cutting speed, tool heating, and workpiece cooling, are investigated for the end milling of the KM rubber, a natural rubber compound provided by Michilen for automotive tire tread applications. The KM rubber

consists mostly of the natural rubber. Properties of the natural rubber compound can be used to represent the work-material [4].

The chip morphology in elastomer machining is unique. Material properties of the elastomer, such as the very low thermal conductivity and elastic modulus and the large elongation before fracture, all contribute to distinctively different shapes of machined chips. A four-step procedure, as shown in Fig. 2.2, has been proposed to classify the morphology of elastomer chips. Based on four classification steps, i.e., burning, straight or rough edge, curl or flat shape, and serrated or smooth surface, seven types of elastomer chip can be identified. In this chapter, this procedure was applied to classify elastomer chips generated in end milling tests.

The accurate measurement to quantify the roughness of machined elastomer surface is a technical challenge. Using the contact stylus method, fine features and asperities on the elastomer surface are deformed by the contact force. This has been discussed by Stupak et al. [5] using the profilometer to characterize the worn surface of rubber. Using the non-contact optical method, the low reflectivity of the surface is a problem. Elastomers for tire applications, like the workpiece used in this chapter, are usually black and have very low light reflectivity. Ganesan et al. [6] and Schaal and Coran [7] explored the quantitative measurement of elastomer surface by the optical image processing technique but did not correlate measured results to commonly used surface roughness parameters. In this chapter, the confocal scanning microscopy, which has been used extensively for the measurement of soft tissue and biological materials [8], was applied to study the roughness of machined elastomer surfaces. The height at a small, 1 μm diameter region can be determined by detecting the intensity peak of the laser light reflected from the surface. A confocal scanning microscope with 64 sensors for rapid measurement is used in this chapter. Roughness measurements using both the contact stylus profilometer and non-contact confocal microscopy are compared in this chapter.

Cutting forces provide the insight of the interaction between the tool and workpiece in machining. The research conducted in [2] shows that end milling of solid carbon dioxide cooled elastomers, compared to the room temperature workpiece, generated larger cutting forces. By studying the cutting forces, effects of three key

process parameters (cutting speed, tool heating, and workpiece cooling) are investigated. The groove width after end milling of elastomer is significantly smaller, about 22 to 32% less, than the tool diameter. This is due to the low elastic modulus and large deformation of the elastomer workpiece exhibited during machining. The correlation between the groove widths and cutting forces is studied. The elastomer workpiece can also vibrate during machining at a low frequency, likely also at a relatively large amplitude. Frequency analysis of the cutting forces can reveal the vibration of elastomer workpiece and correlate with the distance between machining marks.

The experimental setup, test procedure, and data analysis are presented in the following section. The size and morphology of elastomer chip are classified in Sec. 5.3. Cutting force analysis is presented in Sec. 5.4. The machined grooves are studied in Sec. 5.5. The measurement results and quantitative analysis of machined surfaces are discussed in Sec. 5.6.

5.2. Experimental setup, test procedure, and data analysis

5.2.1. Machine setup

The experimental setup for end milling of elastomers is shown in Fig. 5.1(a). The tool, a 12.7 mm diameter, 127 mm long, double-flute, down-cut high speed steel end mill (Onsrud 40-series), was driven by the spindle in a CNC vertical end milling machine. This is the same tool used in the induction heating experiments conducted in Chapter 4. The tool geometry has proven to be effective in the elastomer material removal in end milling [1]. A Ti thermal insulator was used to reduce the heat transfer to the spindle. A water-cooled induction heating coil surrounding the tool could be utilized to heat the rotating tool for elastomer machining.

Good fixture design is important for elastomer machining [1]. The fixture, as shown in Figs. 5.1(b) and 5.1(c), is designed to hold the plate-shape elastomer workpiece between the base and top plate. There are seven grooves on the top plate for seven end milling tests along these grooves. This fixture design can provide adequate and consistent structural support to the soft elastomer workpiece for end milling experiments. The fixture was mounted on a force dynamometer.

5.2.2. Experimental design

Eight elastomer end milling tests were conducted at two spindle speeds (1100 and 2900 rpm), two tool temperatures (with and without induction heating to 300°C tool tip temperature), and two workpiece temperatures (with and without cooling by solid carbon dioxide at -78°C) to study effects of three process parameters. The tool tip temperature at 300°C was proven beneficial for the effective elastomer machining in the preliminary tests using the induction-heated tool. The feed rate was 3 mm/s and depth of cut was 4 mm. All tests were conducted dry with no cutting fluid. As shown in Table 5.1, four sets of experiments, marked as Exp. VIII, IX, X and XI, are used to classify these eight cutting tests by the tool and workpiece temperatures. For each elastomer end milling test, chips were collected, cutting forces were recorded, width of grooves was measured, and machined surfaces were inspected.

5.2.3. Surface inspection

Comprehensive study of machined elastomer surfaces using the contact stylus profilometer, confocal scanning microscopy, scanning electron microscopy (SEM), and optical microscopy were performed in this chapter. The arithmetical average roughness, R_a , was selected as the parameter to represent the machined elastomer surface. The cut-off length for filtering the raw measurement data is critical to obtain representative and consistent R_a values. The upper and lower cut-off lengths of the Gaussian filter are applied to derive the roughness of the profile [9]. The conventional upper cut-off length of 0.8 mm is not suitable for machined elastomer surfaces due to the large distance between machining marks at low spindle speed. In this chapter, 2.5 mm upper cut-off length is selected to meet the general guideline to have about 10 surface high points within the upper cutoff length [10].

A Taylor-Hobson profilometer with the sharp 10 μm radius tip is utilized for the contact stylus measurement. Two 40 mm traces are conducted along and against the milling feed direction [5]. These two measurement results are averaged. The profilometer has a lateral resolution of 1 μm .

The Siemens SISCAN MC64 confocal scanning microscope with 440 μm measurement range and 0.5 μm height and 10 μm lateral resolutions is applied for the non-contact measurement of machined elastomer surfaces. This optical measurement device uses an infrared diode laser with 830 nm wavelength to scan 200 traces (6 mm long) in a 2 mm by 6 mm area. This confocal microscope has 64 sensors for fast and precise scanning measurement.

The low reflectivity of black elastomer material can cause the high frequency noise in confocal microscope measurements. A 6 mm long measurement on the elastomer surface machined in Experiment XI (with tool heating and workpiece cooling) at 2400 rpm is shown in Fig. 5.2(a) as an example. High spikes, which exceed the 440 μm measurement range, can be seen. The high frequency noise can be removed using software filtering methods.

Frequency domain analysis of all eight confocal microscope measurements shows a peak at about 20 μm wavelength due to the high frequency noise. The finite impulse response (FIR) low pass filter in MATLAB with the stop wavelength of 25 μm and pass wavelength of 50 μm is used to remove the high frequency noise. The measured data in Fig. 5.2(a) is processed using the FIR filter and results are shown in Fig. 5.2(b). The high frequency noise is removed.

Another method is using the Gaussian filter in OmniSurf, a surface texture software package produced by Digital Metrology Solutions. The lower cut-off length of the Gaussian filter is set at 25 μm to remove the high frequency noise. Omnisurf is used to analyze both the contact stylus and non-contact confocal microscope measurement data and extract the R_a value.

A Philips XL SEM was used to observe the machined elastomer surfaces.

5.2.4. Force analysis

A piezoelectric force dynamometer, Kistler Model 9257B, as illustrated in Fig. 5.1, was used to measure the three force components during elastomer end milling tests. The voltage signals from the dynamometer were amplified and acquired using a PC-based data acquisition system at 1000 Hz sampling rate. Calibration tests were conducted to find the conversion factor from voltage to force. The XYZ coordinate system used to

define the cutting force direction is shown in Fig. 5.3. The X-axis coincides with the feed direction. The Z-axis is along the rotating axis of the tool which is perpendicular to and pointing outward from the flat surface of elastomer plate.

F_x , F_y , and F_z are three end milling force components acting on the workpiece from the rotating tool. The F_x should generally be positive because of the tool feed direction. Due to the rotational direction of the tool, the F_y should be mostly negative. Since the tool pushes the workpiece in the negative Z direction, F_z should remain negative. Such trends have been demonstrated in [2] and also observed in this chapter. For each revolution of the double-flute tool, two peaks occurred in traces of force components F_x and F_y [2].

5.3. Chip size and morphology

Fig. 5.4 shows the optical micrographs of elastomer chips for Exps. VIII–XI. Four types of chips, B, RC, SCM, and RF, with the size ranging from 1-2 to 5-7 mm are identified. The uncut length and width of the chip is 19.9 and 4 mm, respectively, for the 12.7 mm diameter tool used in this chapter. The actual size of the chip is much smaller. This indicates the frequent breakage of chip during end milling.

At high temperature, the elastomer degrades and gasifies into smoke. The vulcanized natural rubber compound begins to degrade around 150 to 200°C [11]. This is lower than the 300°C tip temperature of the induction-heated tool. During cutting, the high specific energy in the chip generates localized high temperature, which burns a portion of the elastomer material, generates smoke, and creates the B type chip morphology with the melting surface texture. Higher chip temperature is expected at high spindle speed, induction-heated tool, and room temperature workpiece. This can be validated by observing the concentration of B type chip in Fig. 5.4.

The effect of cutting speed can be identified that, at 1100 rpm spindle speed, only the induction-heated tool has the B type chip. At 2400 rpm spindle speed, all four cutting tests have the burned, B type chip. Under the same tool feed rate, the high spindle speed reduces the maximum uncut chip thickness and increases the specific energy input to the elastomer chip. This promotes the chip burning and B type chip formation. All four tests

at 2400 rpm spindle speed also generate visible smoke during end milling tests. The effect of cryogenic workpiece cooling on B type chip generation is not as obvious as the spindle speed and tool heating. Close observation of chips can recognize that, although not obvious, less concentration of the B type chip for cutting the cryogenically cooled elastomer workpiece.

The RC and SCM types chip morphology can be seen in all cutting conditions except the induction-heated tool cutting without workpiece cooling (Exp. IX) at 2400 rpm spindle speed, which is the setup with the highest specific energy input to the elastomer workpiece. Under such cutting condition, the RF type chip, small chip size, and high concentration of B type chip are recognized. The elongation before fracture of elastomer is reduced at elevated temperature [12,13]. Also, at high strain rate, the elastomer becomes less ductile [13,14]. Both material properties contribute to more frequent chip breakage and facilitate the RF type of chip generation. Under the same initial tool and workpiece temperatures, higher concentration of small size chip can be found at the 2400 rpm spindle speed in all four Exps. VIII to XI. It is particularly obvious in Exp. IX.

5.4. Cutting forces

Fig. 5.5 shows three end milling force components, F_x , F_y , and F_z , and the frequency domain analysis of F_x and F_y in Exp. IX (induction-heated tool, no workpiece cooling) at 1100 rpm spindle speed. As expected, F_x remains mostly positive and F_y , and F_z remain negative during end milling [2]. The F_x and F_y show the significant cyclic variation due to the tool rotation while the F_z remains at a relative constant level of about -90 N. For each revolution of the tool (0.055 s), two peaks can be seen in F_x and F_y for the double flute tool [2]. Similar trend of F_x , F_y , and F_z can be observed for end milling at 2400 rpm. This is illustrated by an example of Exp. XI (induction-heated tool with workpiece cooling) in Fig. 5.6(a).

The frequency domain analysis of Exp. IX at 1100 rpm, as shown in Fig. 5.5(b), shows the peak frequency at 37.1 Hz, which is twice of the 1100 rpm spindle speed because of the double-flute tool. Another two peaks observed in F_y are at 18.6 Hz (the

1100 rpm spindle speed) and 6.8 Hz. As shown in Fig. 7(b), at 2400 rpm spindle speed, a peak at the same 6.8 Hz can also be identified along with 40.5 Hz (2400 rpm) and 81.0 Hz (twice the spindle speed for double-flute tool). Table 5.2 summarizes the frequency of the 1st, 2nd, and 3rd peaks of F_y for eight end milling tests. All eight tests, regardless of spindle speed, have the 1st peak frequency at about 7 Hz. This relatively low frequency is due to the vibration of the soft elastomer workpiece.

This low 7 Hz frequency vibration can be recognized in the time domain force traces in Figs. 5.5(a) and 5.6(a). In Fig. 5.5(a), high peaks of F_y are marked by the thick arrows. Spacing between these arrows is about every 6 peaks or 3 revolutions of the tool at 1100 rpm. This matches to the 7 Hz frequency. At 2400 rpm, the 7 Hz frequency corresponds to about 6 tool revolutions or 12 peaks between high peaks of F_y . This can also be recognized by two thick arrows in Fig. 5.6(a). The workpiece low frequency vibration has a significant effect on the machining mark or surface texture generation at 1100 rpm spindle speed. As will be presented by SEM micrographs of machined surfaces in Sec. 5.6, the distance between machining marks is affected by the workpiece low frequency vibration.

It is noted that there are discrepancies between the actual measured peak frequencies and speed settings: 1100 rpm (18.3 Hz) and 2400 rpm (40.0 Hz). This is due to the accuracy of the machine spindle speed control and also possibly affected slightly by the frequency analysis calculation.

Effects of spindle speed, tool heating, and workpiece cooling on the magnitude of the averaged peak cutting forces are presented in Fig. 5.7. The averaged peak cutting force components F_x , F_y , and F_z are calculated by averaging the absolute value of 120 consecutive peaks in 60 tool rotations [2].

The effect of spindle speed on cutting forces depends on tool heating condition. At high spindle speed, the uncut chip thickness is reduced, which is expected to decrease the cutting forces, and the strain rate is increased, which, in turn, will increase the cutting forces. With tool heating (solid symbols in Fig. 5.7), cutting forces F_x and F_y increase at higher spindle speed. This is likely due to the adhesion of elastomer work-material to the tool rake surface and changes of cutting edge geometry similar to the build-up edge in metal cutting [15]. With the combination of high cutting speed and heated tool, the

build-up edge for elastomer machining is created and results in high cutting forces. The build-up edge is visible on the tool cutting edge after end milling. This tool requires cleaning at the beginning of end milling tests. With no tool heating (open symbols in Fig. 5.7), minimal chip adhesion or no build-up edge was observed and lower cutting forces F_x and F_y can be seen at 2400 rpm spindle speed. Regardless of tool temperature and workpiece cooling, smaller F_z is generated at 2400 rpm spindle speed. At 1100 rpm spindle speed, tool heating does not change cutting forces significantly. The effect of tool heating on cutting forces becomes apparent at the high spindle speed.

On the workpiece cooling effect, higher cutting forces can be identified with cryogenically cooled workpiece. This is consistent with the observation in [2].

5.5. Machined grooves

Fig. 5.8 summaries optical pictures of the groove and bottom surface of machined elastomer workpiece in all end milling tests. The arc of machining marks with its curvature resembling the tool diameter can be recognized on bottom surfaces of the groove at low spindle speed (1100 rpm). At 2400 rpm, the curved machining marks can be seen only on the workpiece without cryogenic cooling. For the solid carbon dioxide cooled workpiece machined at 2400 rpm, the bottom surface of groove does not have clearly visible curved machining marks. Using SEM, machined surfaces will be further investigated in the following section.

Unlike the conventional end milling of metals, the groove width, W , ranging from 8.6 to 9.9 mm and listed in Fig. 5.8, is much narrower than the 12.7 mm tool diameter. This demonstrates the difficulty to generate a precise shape in elastomer machining. The elastomer workpiece is deformed by the cutting forces during machining and recovers afterward. This is illustrated in Fig. 5.9(a) by the picture of a hole generated at the end of a milling trace. While the tool is not moving but continuously rotating and retracting from the workpiece, a hole larger than the groove width but smaller than the tool diameter is generated. Fig. 5.9(b) shows relative size of the hole, tool, and maximum and minimum groove width machined in end milling tests. Process parameters significantly affect the groove width as well as the topography of two side surfaces on the groove.

Two side surfaces in the groove are distinctly different. The surface as the tool cuts into the workpiece, marked as the entry surface, is smoother than the opposite side, which is denoted as the exit surface. The exit surface is wavy and often has long residual burrs. Due to the waviness of exit surface, the groove width is measured at 10 locations. The averaged value is used to represent the groove width.

Depending on the cutting conditions, the groove width is only 68 to 78% of tool diameter. The deformation is mainly caused by the compression caused by the cutting force F_y on the workpiece in the Y direction during end milling. The groove width, W , vs. the average F_y of Exps. VIII to XI is shown in Fig. 5.10. The number next to the symbol indicates the spindle speed, either 1100 or 2400 rpm. The high spindle speed generates wider groove width in all four Exps. VIII to XI. The maximum groove width, about 9.9 mm, is generated under two cutting conditions at 2400 rpm with no workpiece cooling. Cryogenically cooling the workpiece (square symbols) increases the workpiece elastic modulus but generally does not create a wider groove. This contradicts to the intuitive thinking and is likely to be caused by the more effective material removal of the elastomer material, even at room temperature, using the sharp, down-cut router tool.

A linear trend can be recognized for data points in Fig. 5.10. The regression analysis is applied to fit a line to eight data points.

$$W = -0.07 \cdot F_y + 12.5 \text{ (mm)} \quad (5.1)$$

Equation (5.1) indicates that, as the force F_y approaches 0, the groove width W is 12.5 mm, which is close to the 12.7 mm tool diameter. The coefficient of 0.07 mm/N in Eq. (5.1) is the estimated compliance of workpiece in the Y direction under the experimental setup used in this chapter. Decreasing the workpiece compliance can help reduce the groove width variation. This affirms the previous finding of the importance of fixture design in elastomer machining [1].

5.6. Machined surfaces

Bottom surfaces of machined grooves in eight elastomer end milling tests, as shown in Fig. 5.8, are investigated in this section. Fig. 5.11 presents SEM micrographs on corresponding machined surfaces with detailed features such as curved machining marks, burrs, and residuals after burning. The distance between machining marks and surface roughness, measured using both contact and non-contact measurement methods, are discussed in the following sections.

5.6.1. Distance between machining marks

At 3 mm/s feed, the double-flute end mill has 82 and 38 μm maximum uncut chip thickness at 1100 and 2400 rpm spindle speed, respectively [16]. Ideally, if a chip is removed in every engagement of the cutting edge and workpiece, the distance between machining marks on the machined surface will reflect such value [17]. The actual distance, measured from SEM micrographs, between major machining marks is about 0.4 to 0.5 mm. It is much larger than the ideal value and indicates that, during the end milling, the tool cutting edges rub against the elastomer workpiece several times until a critical condition is reached to generate the chip. Between major machining marks, some minor machining marks can be seen. It reveals the source for chip generation during end milling.

At 1100 rpm, the 0.4 to 0.5 mm distance between machining marks, as indicated in Fig. 5.11, is about 6 times of the maximum uncut chip thickness (82 μm). The distance between three horizontal lines in Fig. 5.11 is 0.45 mm. About 6 engagements of the cutting edge with the workpiece, or 3 revolutions of the double-flute tool, will create a chip removal cutting action. Correspondingly, high peaks of F_y are observed at about every 6 peaks in Fig. 5.5(a). In one period of the workpiece 7 Hz low frequency vibration, which is about 0.14 s, the tool advances 0.43 mm in the feed direction. This value is close to the distance between machining marks and indicates that, at 1100 rpm spindle speed, the workpiece vibration is a key factor on the distance between major machining marks.

At 2400 rpm, machining marks can only be recognized on surfaces machined on workpiece with no cryogenic cooling. This matches to the observation in Fig. 5.8 using

the optical microscope. About the same distance (0.4 to 0.5 mm) between major machining marks can be seen as in the 1100 rpm. Under the same workpiece vibration frequency (7 Hz) and feed rate (3 mm/s), the tool advances the same 0.43 mm in the feed direction in one period of workpiece vibration. The effect of workpiece vibration on the distance between machining marks can also be identified on machined surfaces. There are many minor machining marks with much shorter spacing distance on surfaces machined at 2400 rpm. The more efficient cutting at high spindle speed and frequent chip breakage, which results the smaller chip size (shown in Fig. 5.4), contribute to the generation of many minor machining marks between major machining marks.

The height profile traces measured by the profilometer on machined elastomer surfaces, as shown in Fig. 5.11, are applied for the frequency domain analysis to inspect the appearance of major machining marks. Frequency analysis results are shown in Fig. 5.12. No obvious frequency peak occurs in the 2 to 2.5 mm⁻¹ range, which is corresponding to the 0.4 to 0.5 mm distance between major machining marks, for all machined elastomer surfaces. The frequency domain analysis cannot reveal the distance between major machining marks on machined elastomer surfaces as observed. The possible reason is on the limited resolution to capture the fine surface features on machined elastomer surface. The features exist and can be observed using SEM. However, a better surface profilometer needs to be developed for the measurement of machined elastomer surfaces.

5.6.2. Surface roughness

Two measurement methods, the contact profilometer and non-contact confocal microscopy, are utilized to measure the R_a of machined elastomer surfaces. Measurement results are summarized in Table 5.3. In confocal microscopy measurements, two sets of data with and without the FIR pre-filtering are presented to explore the effect of different high frequency noise filtering procedures.

High spindle speed can improve the surface roughness. This is demonstrated in both profilometer and confocal microscope measurements. The same trend has been reported by Jin and Murakawa [3]. It is obvious in Fig. 5.11 that the high spindle speed increases the deformation rate and enables more frequent chip breakage and efficient

cutting. The size of burrs is also much smaller on surfaces machined at 2400 rpm. Although high cutting speed can improve surface roughness, the smoke prohibits the high speed machining of elastomer in actual application. All tests at 2400 rpm have significantly visible smoke generated during machining.

The effect of workpiece cooling on surface roughness is not obvious. Unlike the distinctly different surface textures shown in the SEM micrographs in Fig. 5.11, which also have the profilometer measured R_a values listed, the surface roughness R_a is about the same for workpiece machined with and without cryogenic cooling.

At 1100 rpm, the tool heating can reduce surface roughness. This is important because the elastomer machining at high spindle speed (2400 rpm) is not feasible due to smoke. Tool heating becomes an enabling method for precision machining of elastomer with good surface roughness. The tool heating at 1100 rpm also generate large groove width, as shown in Fig. 5.10. This indicates that tool heating can enable more effective material removal and achieve better workpiece dimensional control at low cutting speed. For the carving of thread in prototype tire manufacturing, carvers use the heated, sharp blade to cut the elastomer at low speed. Heating the blade tool is critical to enable the cutting at a low speed. Similarly, induction heating the tool is important for low speed machining of elastomers.

Discrepancies exist between the profilometer and confocal microscope measurements. In general, the contact force at the stylus tip will deform the protruded fine features, such as burrs, on elastomer surface. Compared to the confocal microscope measurements, smaller R_a values are expected using the contact profilometer method. In Table 5.3, this is generally valid except on two surfaces machined at 1100 rpm without tool heating. As shown in Fig. 5.11, these two surfaces have large burrs. The burr may bend and block the view of confocal microscope to reach the bottom of valley on machined surface. The low light reflectivity inside the valley may also limit the accuracy of surface roughness measurement using the confocal microscope. Both will result low R_a than the actual value.

The confocal microscope measurements are analyzed using the OmniSurf software to calculate the R_a . The data processed by OminSurf can be pre-filtered using the FIR filter in MATLAB. Pre-filtering the data removes the noise as well as some fine

features on surface measurement profile. It consistently lowers the R_a value. Although the pre-filtering changes the R_a value, it does not alter the general trend observed on the effect of cutting speed, workpiece cooling, and tool heating for surface roughness.

5.7. Conclusions

This chapter investigated effects of cutting speed, tool heating, and workpiece cooling on machining of elastomers. Cutting speed was demonstrated to be critical. At high cutting speed, smoke was generated and became environmentally hazardous. At low cutting speed, the surface roughness was high and material removal was not effective, which resulted the narrow groove width in end milling. Induction heating the tool could improve the surface roughness and enable effective material removal for low speed machining of elastomers.

The low stiffness of elastomer workpiece affected the surface quality. Even using specially designed fixture to enclose every end milling cut, the low elastic modulus of elastomer inherently generated a 7 Hz low frequency vibration during machining. On machined surface, the distance between major machining marks was affected by the low frequency workpiece vibration.

Quantitative comparison of both contact stylus profilometer and non-contact confocal microscopy roughness measurements on machined elastomer surfaces were conducted. Both methods showed their limitations. The deformation of the fine surface features of elastomer using contact stylus resulted in lower R_a values compared to most of the confocal microscope measurements. Burrs on surface could block the view of confocal microscope to reach the bottom of valley. Low surface reflectivity inside the valley was also a problem. This chapter showed that the surface inspection of elastomers is still a technically challenging problem and requires further research.

Another future research area is the machining of precise three-dimensional shape of elastomer workpiece. The relatively small width of machined grooves, about 68 to 78% of the tool diameter, showed the difficulty to achieve good dimensional control of the elastomer workpiece. Induction-heated tool showed some improvement but was still

not adequate for precise dimensional control. Novel methods need to be developed to further advance the elastomer machining technology and application.

References

- [1] Shih, A. J., Lewis, M. A., and Strenkowski, J. S., 2004, "End Milling of Elastomers – Fixture Design and Tool Effectiveness for Material Removal," *ASME Journal of Manufacturing Science and Engineering*, Vol. 126, No. 1, pp. 115-123.
- [2] Shih, A. J., Lewis, M. A., Luo, J., and Strnkowski, J. S., 2004, "Chip Morphology and Forces in End Milling of Elastomers," *ASME Journal of Manufacturing Science and Engineering*, Vol. 126, No. 1, pp. 124-130.
- [3] Jin, M., and Murakawa, M., 1998, "High-Speed Milling of Rubber (1st Report) - Fundamental Experiments and Considerations for Improvement of Work Accuracy," *Journal of the Japan Society for Precision Engineering*, Vol. 64, No. 6, pp. 897-901.
- [4] Berger, P., 2001, Michelin Americas R&D Corp., *private communication*.
- [5] Stupak, P.R., Kang, J. H., and Donovan, J.A., 1990, "Fractal Characteristics of Rubber Wear Surfaces as a Function of Load and Velocity," *Wear*, Vol. 141, No. 1, pp. 73-84.
- [6] Ganesan, L., Bhattacharyya, P., and Bhowmick, A. K., 1996, "Quantitative Measurement of Roughness of Fractured Rubber Surfaces by an Image Processing Technique," *Journal of Materials Science*, Vol. 31, No. 11, pp. 3043-3050.
- [7] Schaal, S., and Coran, A. Y., 2000, "Rheology and Processability of Tire Compounds," *Rubber Chemistry and Technology*, Vol. 73, No. 2, pp. 225-239.
- [8] Vardaxis, N. J., 1999, "Confocal Scanning Laser Microscopy and Its Application in Biomedical Health Sciences," *Proceedings of SPIE - The International Society for Optical Engineering*, Vol. 3747, pp. 115-127.
- [9] Smith, G. T., 2002, *Industrial Metrology: Surfaces and Roundness*, Springer, London.
- [10] Whitehouse, D. J., 1994, *Handbook of Surface Metrology*, Institute of Physics Publishing, London.
- [11] Mark, J. E., 1996, *Physical Properties of Polymers Handbook*, American Institute of Physics, New York.
- [12] Harper, C. A., 1996, *Handbook of Plastics, Elastomers, and Composites*, 3rd Edition, McGraw-Hill, New York.
- [13] Hertz, D. L., 1979, "Mechanics of Elastomers at High Temperature," High Temperature Electronics and Instrumentation Seminar, Houston, Texas, Dec. 3-4.
- [14] Callister, W. D., 1996, *Materials Science and Engineering: an Introduction*, 4th Edition, John Wiley & Sons, New York.
- [15] Trent, E. M., and Wright, P. K., 2000, *Metal Cutting*, 4th Edition, Butterworth Heinemann, Massachusetts.
- [16] Kim, C., Bono, M., and Ni, J., 2002, "Experimental Analysis of Chip Formation in Micro-Milling," *Transaction of NAMRI*, Vol. XXX, pp. 247-254.

- [17] Sutherland, J. W., and Babin, T. S., 1988, "The Geometry of Surfaces Generated by the Bottom of an End Mill," Proceedings of NAMRC, Vol. 16, pp. 202-208.

Table 5.1. Tool and workpiece temperatures in four end milling experiments.

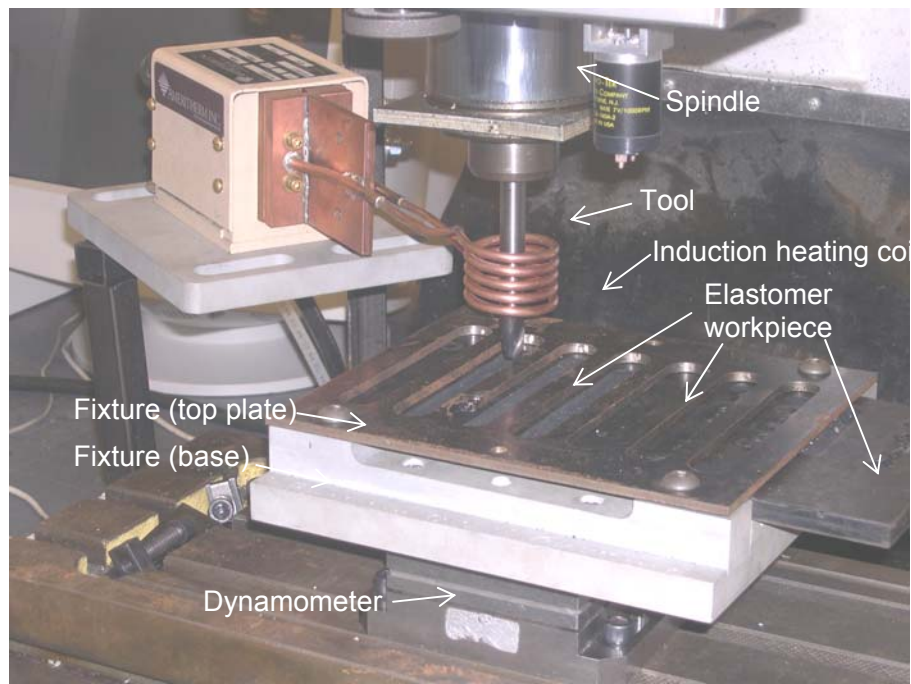
	Room temperature tool (23°C)	Induction-heated tool (300°C)
Room temperature workpiece (23°C)	Exp. VIII	Exp. IX
Solid carbon dioxide cooled workpiece (-78°C)	Exp. X	Exp. XI

Table 5.2. Peak frequency of F_y in elastomer end milling experiments.

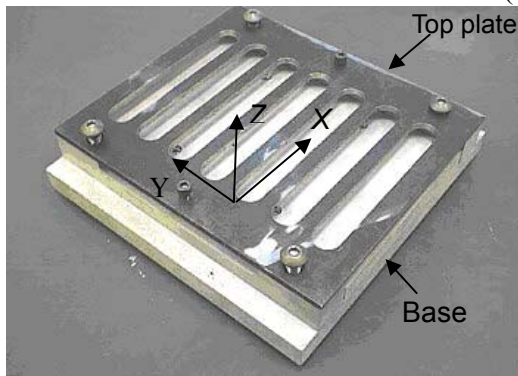
Spindle speed (rpm)	Workpiece temperature	Peak frequency (Hz)					
		Room temperature tool			Induction-heated tool		
		1st	2nd	3rd	1st	2nd	3rd
1100	Room temperature	7.1	18.6	36.9	6.8	18.6	37.1
	Solid carbon dioxide cooled	6.8	18.5	37.1	7.1	18.6	37.1
2400	Room temperature	6.8	40.5	81.4	7.1	40.8	81.3
	Solid carbon dioxide cooled	6.8	40.8	81.3	6.8	40.5	81.1

Table 5.3. Surface roughness R_a measured by the stylus and confocal microscopy.

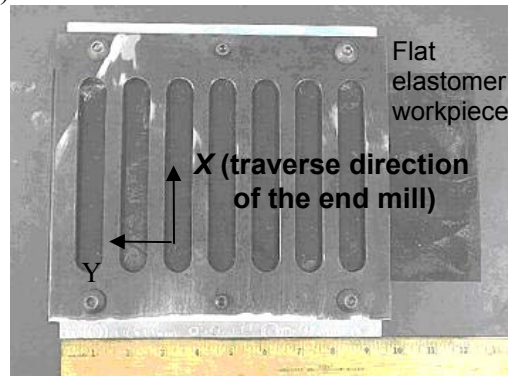
Spindle speed (rpm)	Workpiece temperature	Room temperature tool			Induction-heated tool		
		Profilometer	Confocal microscopy		Profilometer	Confocal microscopy	
			No FIR pre-filtering	With FIR pre-filtering		No FIR pre-filtering	With FIR pre-filtering
1100	Room temperature	81.4	74.9	65.8	56.7	71.3	64.9
	Solid carbon dioxide cooled	76.9	71.0	65.0	54.6	70.4	62.8
2400	Room temperature	36.2	60.6	54.0	40.8	65.0	58.4
	Solid carbon dioxide cooled	39.3	64.5	57.1	36.8	59.9	53.0



(a)



(b)



(c)

Fig. 5.1. (a) Experimental setup of elastomer end milling with tool induction heating, (b) fixture base and top plate with grooves, and (c) top view of the fixture with the elastomer workpiece in place.

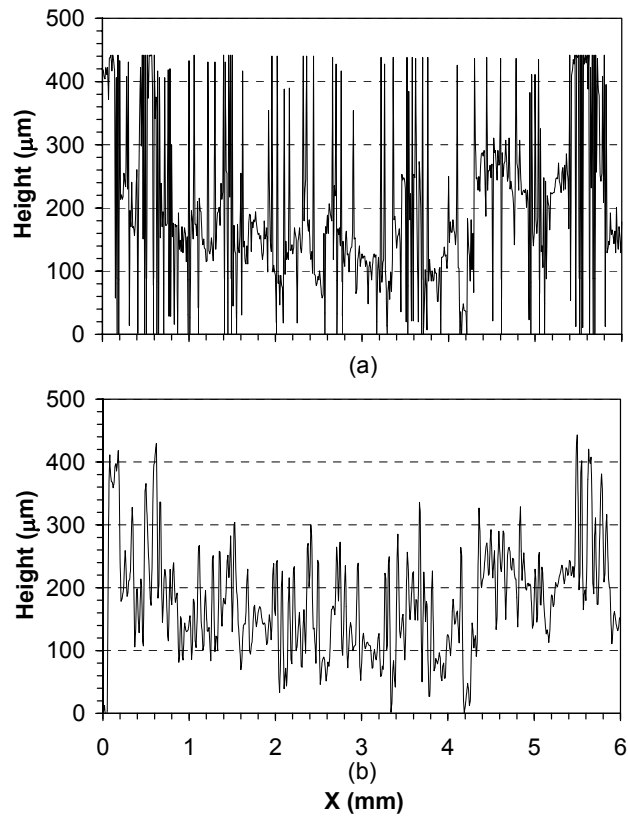


Fig. 5.2. Height profile of machined surface generated in Experiment XI at 2400 rpm: (a) the original height profile, and (b) the height profile with high-frequency noises filtered.

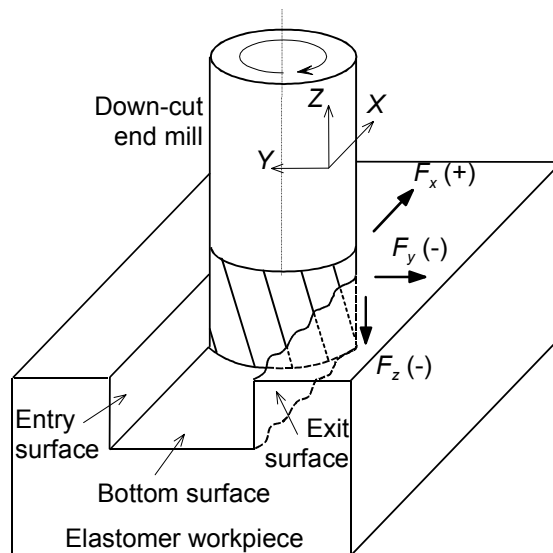


Fig. 5.3. End milling force components.

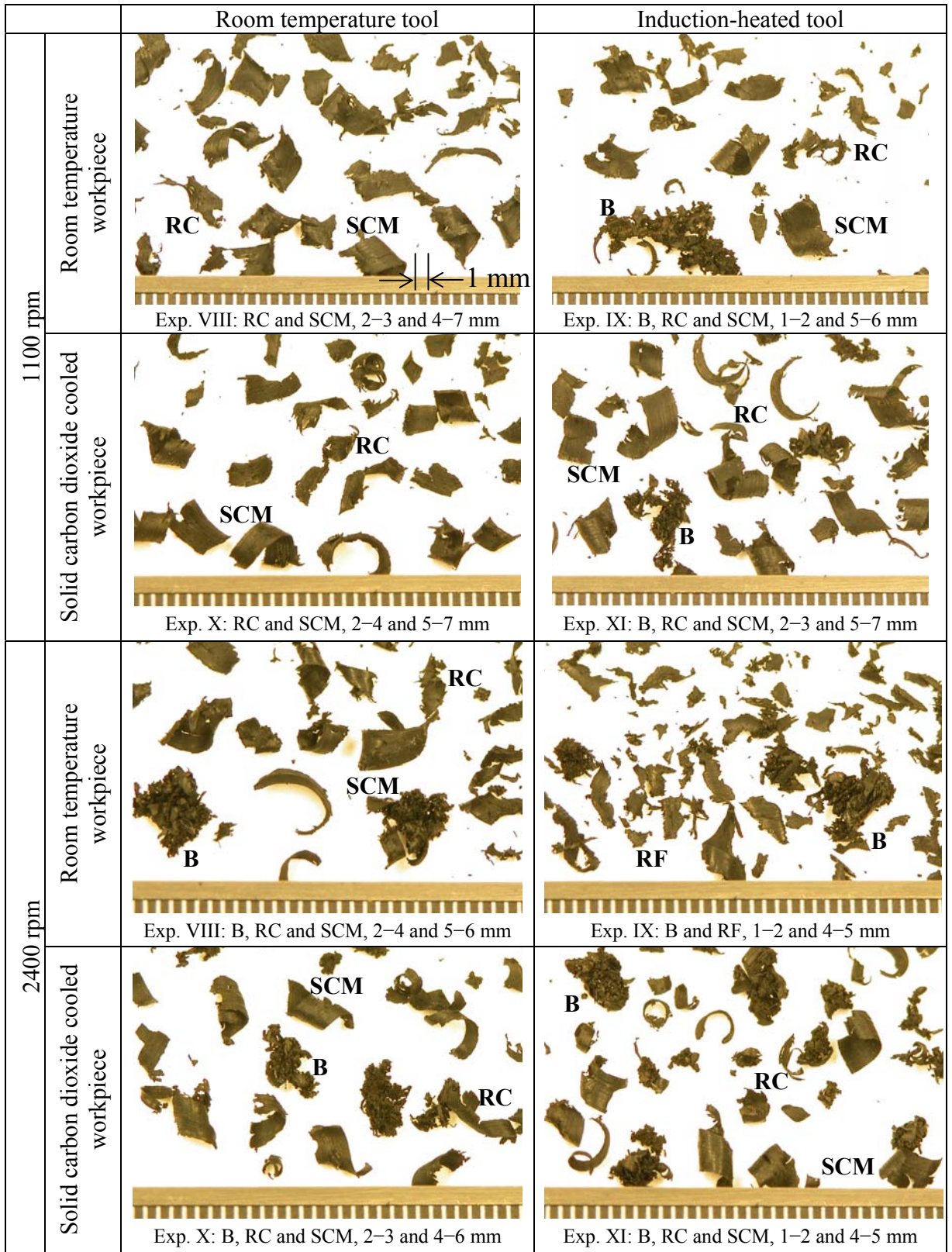
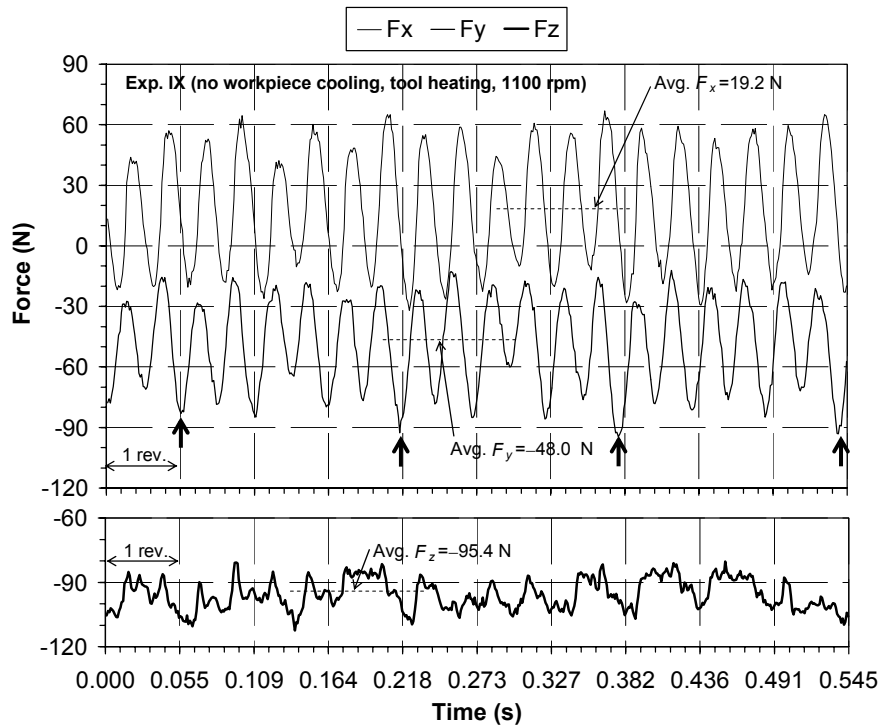
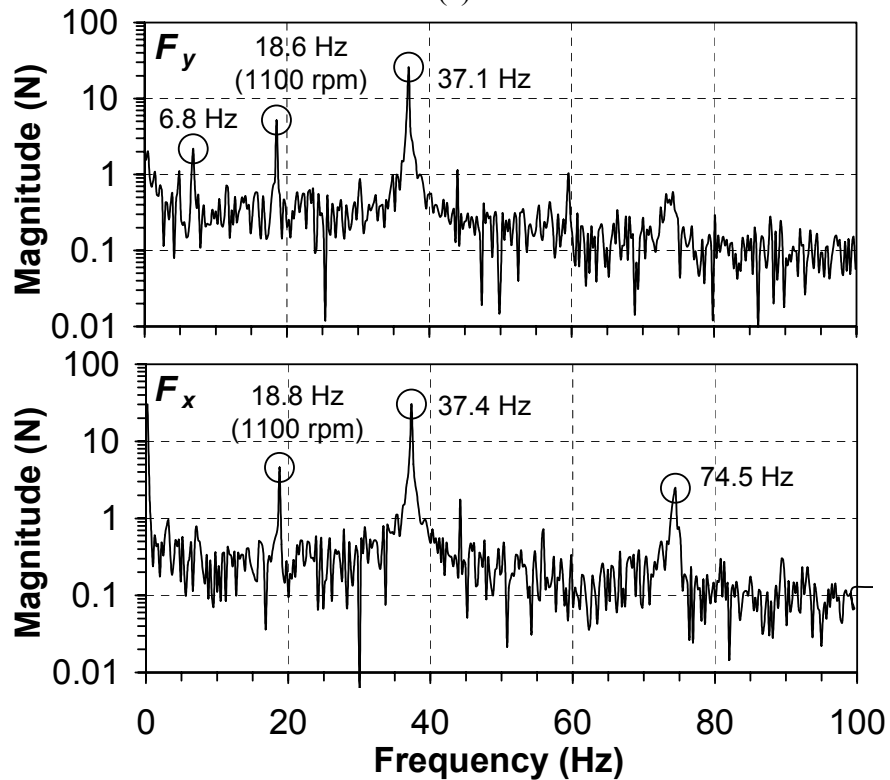


Fig. 5.4. Optical micrographs of elastomer chips.

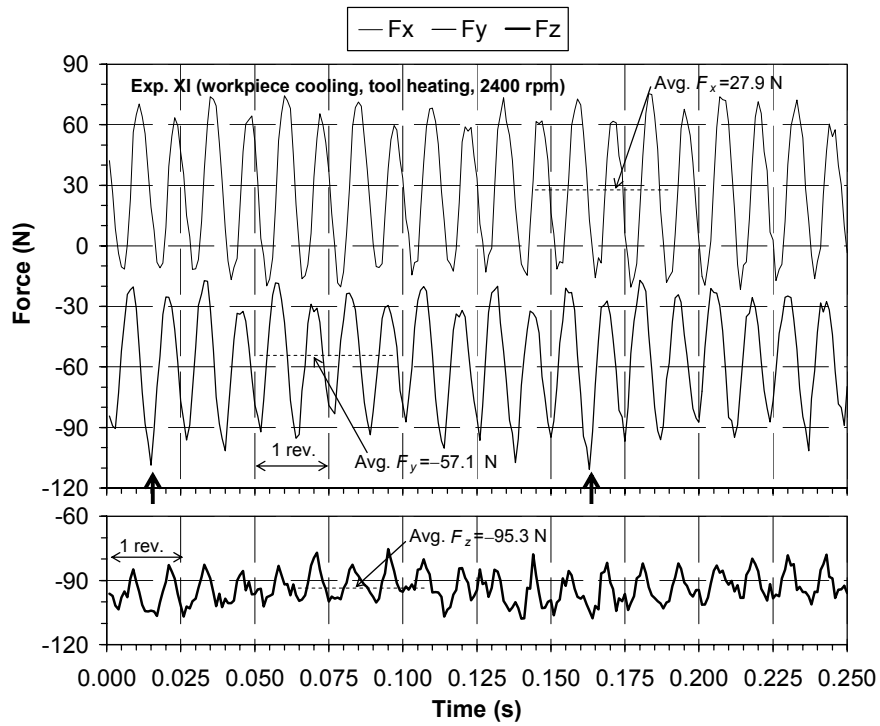


(a)

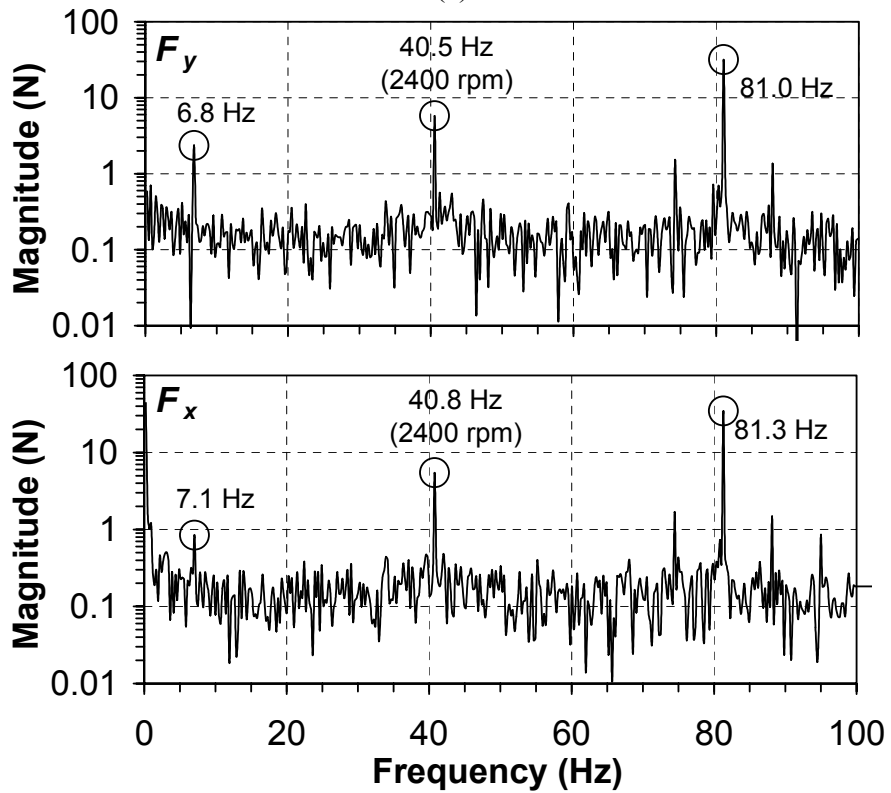


(b)

Fig. 5.5. Experiment IX (no workpiece cooling, tool heating, 1100 rpm): (a) three end milling force components vs. time, and (b) frequency domain analysis.



(a)



(b)

Fig. 5.6. Experiment XI (workpiece cooling, tool heating, 2400 rpm): (a) three end milling force components vs. time, and (b) frequency domain analysis.

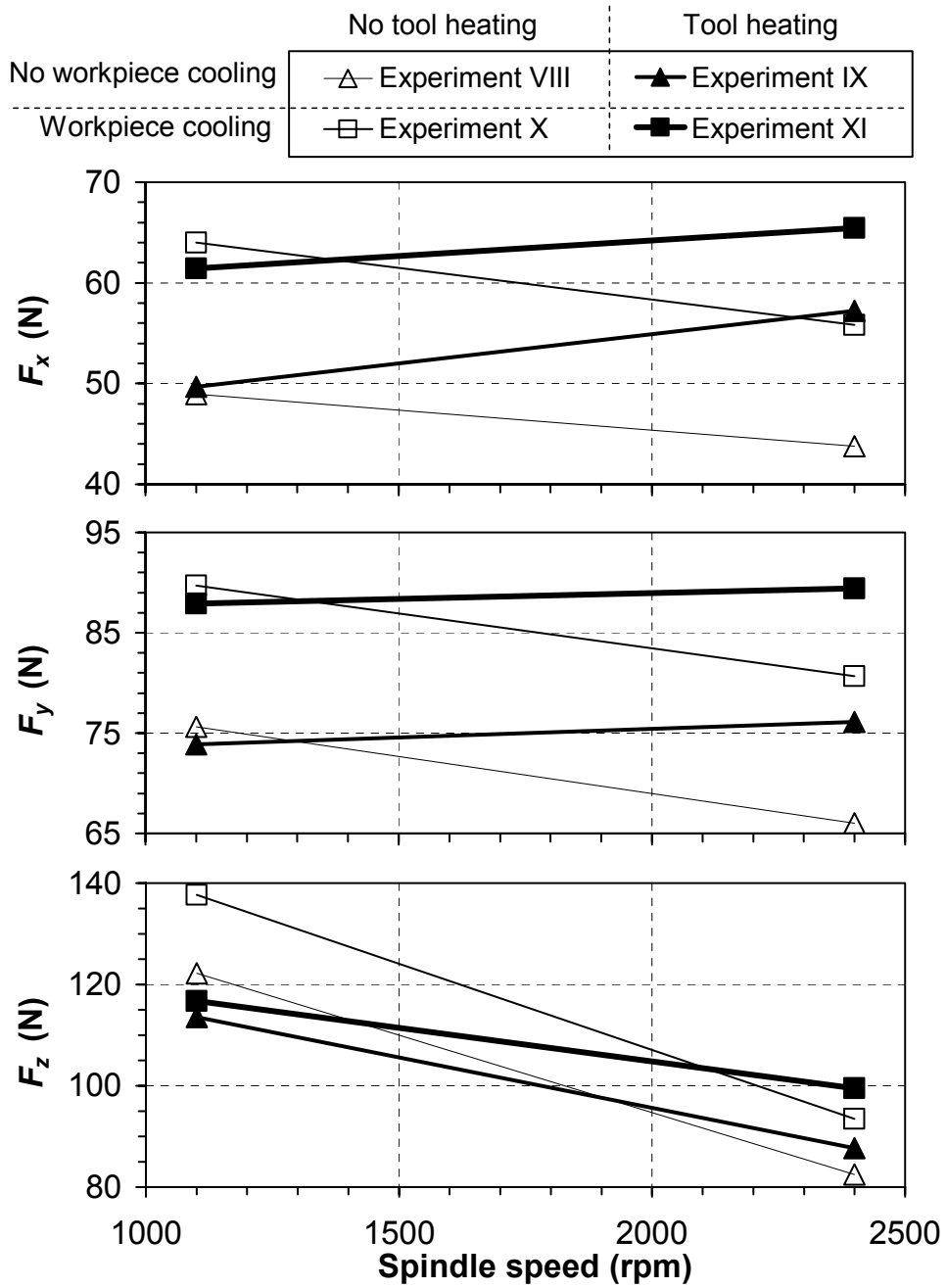


Fig. 5.7. Averaged peak values of end milling forces vs. spindle speeds.

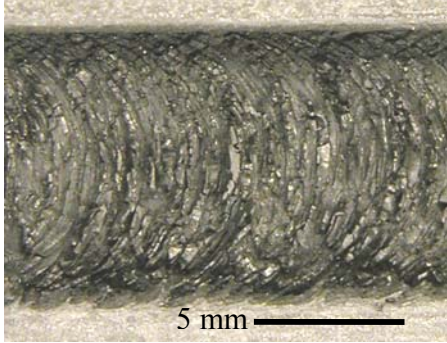
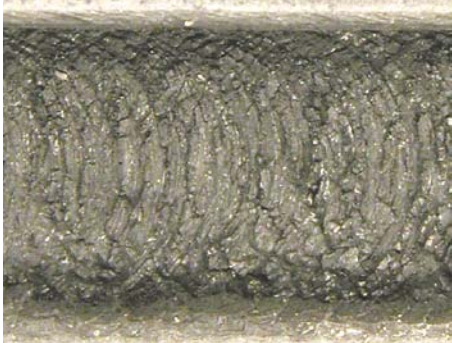
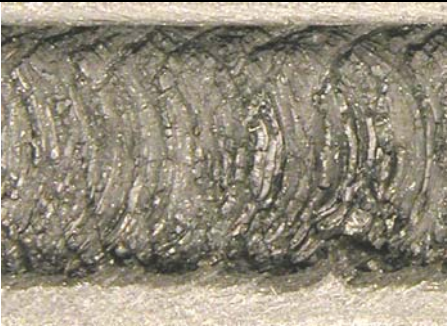
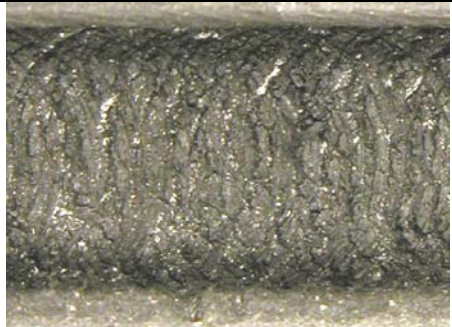
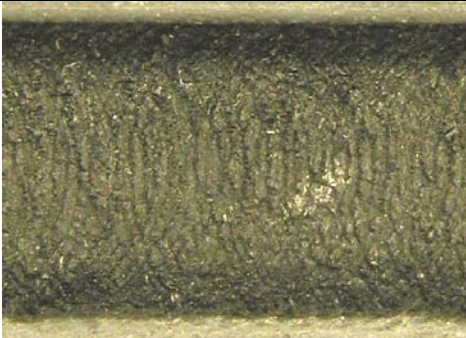
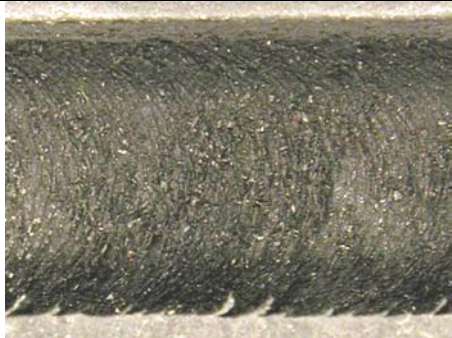
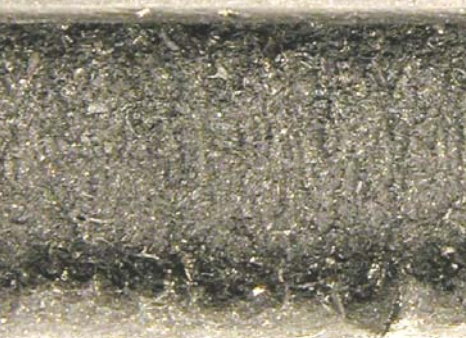
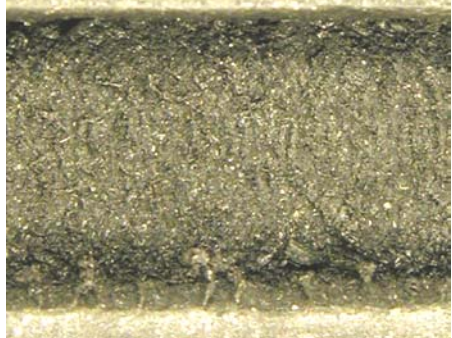
		Room temperature tool	Induction-heated tool
1100 rpm	Room temperature workpiece	 <p>Exp. VIII: W: 8.8 mm</p>	 <p>Exp. IX: W: 9.4 mm</p>
	Solid carbon dioxide cooled workpiece	 <p>Exp. X: W: 8.6 mm</p>	 <p>Exp. XI: W: 8.9 mm</p>
2400 rpm	Room temperature workpiece	 <p>Exp. VIII: W: 9.9 mm</p>	 <p>Exp. IX: W: 9.9 mm</p>
	Solid carbon dioxide cooled workpiece	 <p>Exp. X: W: 9.2 mm</p>	 <p>Exp. XI: W: 8.9 mm</p>

Fig. 5.8. Optical pictures of machined surface. (W is the groove width; the upper surface is the entry surface, and the lower side surface is the exit surface.)

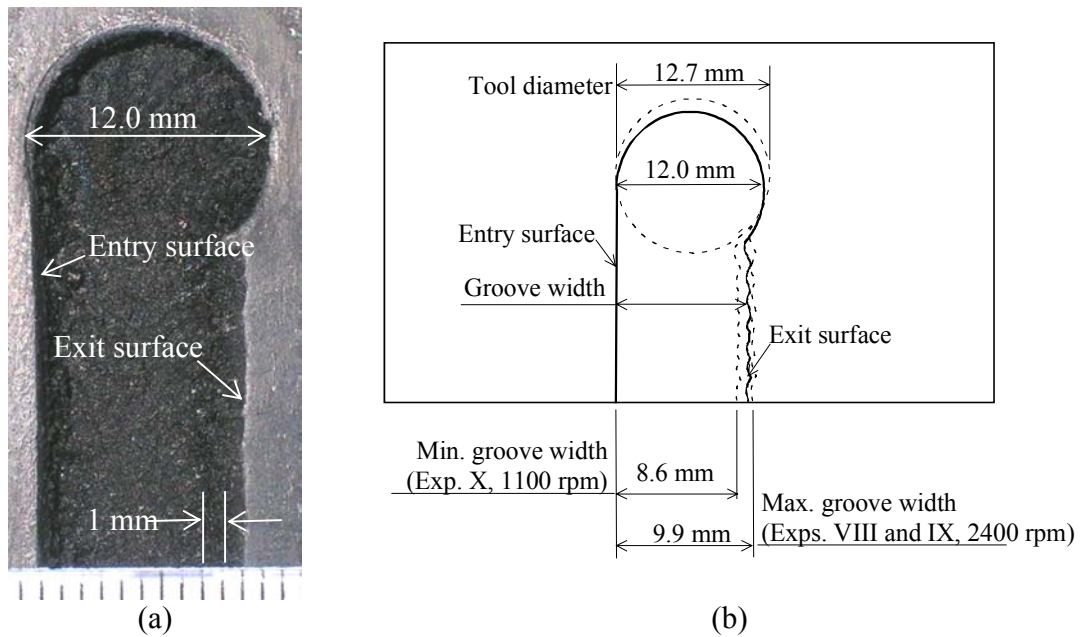


Fig. 5.9. Top view of the groove machined in Exp. VIII at 2400 rpm: (a) picture of the hole generated by retracting end milling tool, and (b) relative size of the tool, hole, and maximum and minimum groove width.

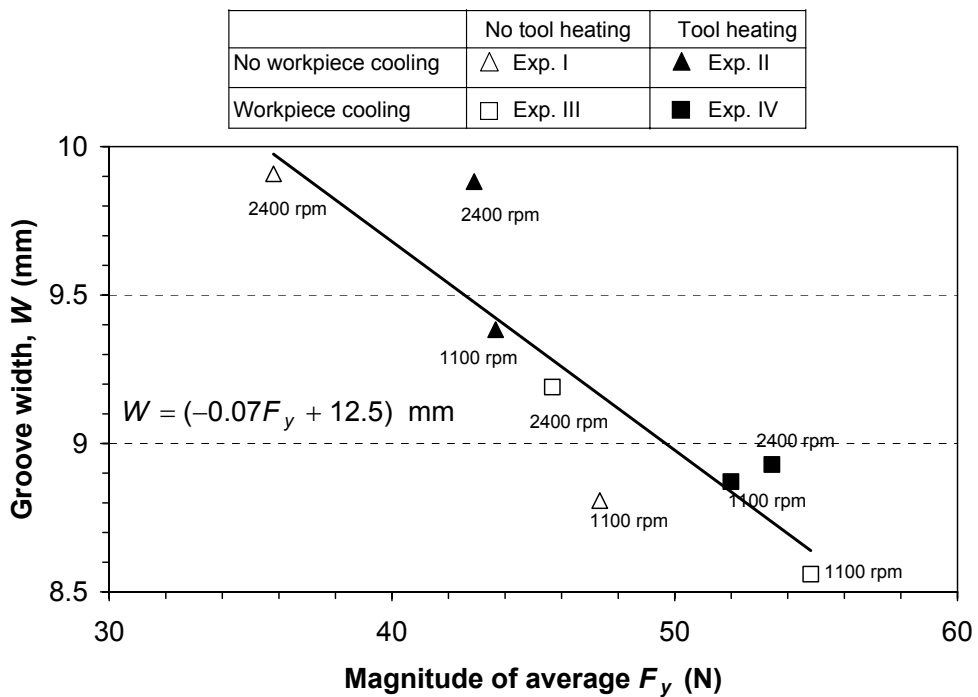


Fig. 5.10. Relationship between the groove width W and cutting force F_y .

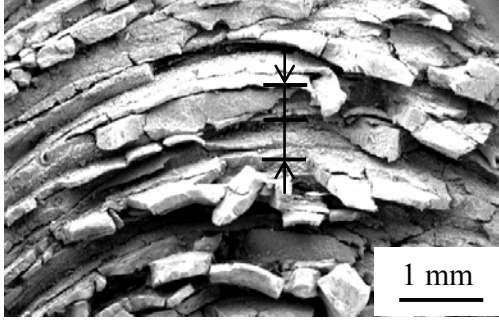
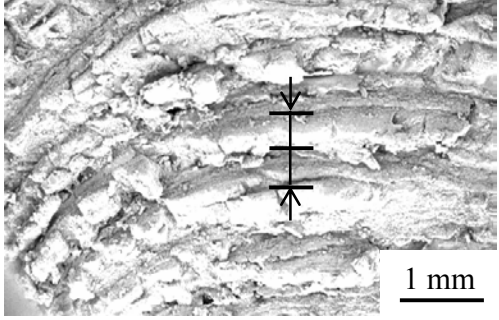
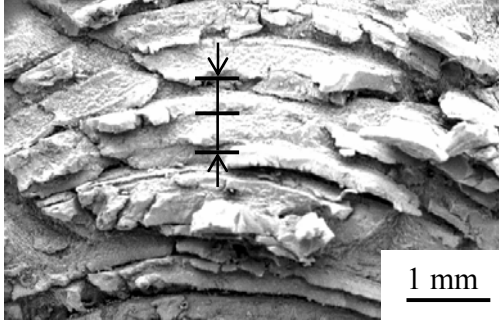
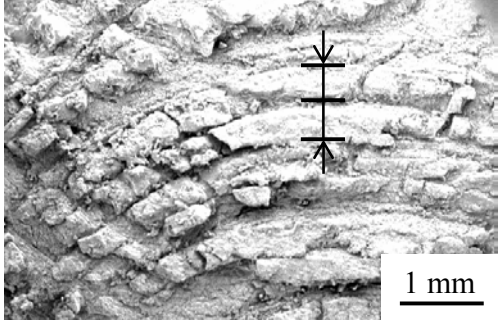
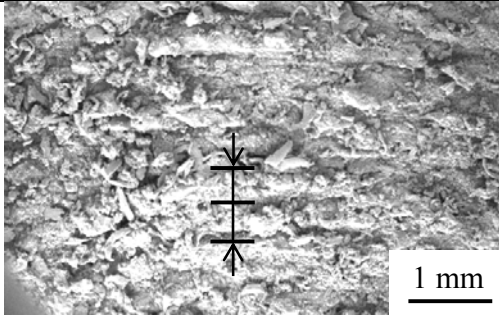
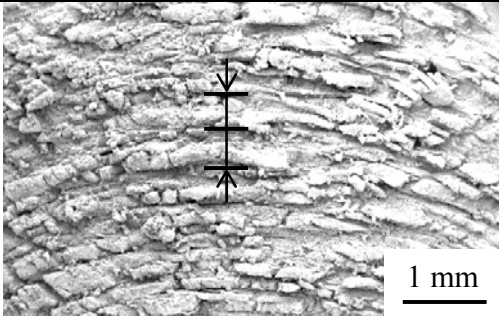
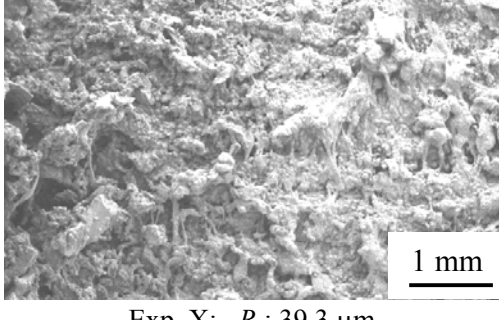
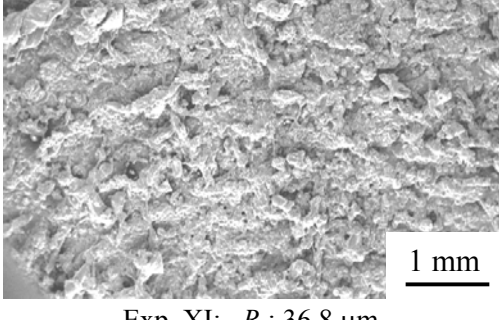
		Room temperature tool	Induction-heated tool
1100 rpm	Room temperature workpiece	 <p>Exp. VIII: R_a: 81.4 μm</p>	 <p>Exp. IX: R_a: 56.7 μm</p>
	Solid carbon dioxide cooled workpiece	 <p>Exp. X: R_a: 76.9 μm</p>	 <p>Exp. XI: R_a: 54.6 μm</p>
2400 rpm	Room temperature workpiece	 <p>Exp. VIII: R_a: 36.2 μm</p>	 <p>Exp. IX: R_a: 40.8 μm</p>
	Solid carbon dioxide cooled workpiece	 <p>Exp. X: R_a: 39.3 μm</p>	 <p>Exp. XI: R_a: 36.8 μm</p>

Fig. 5.11. SEM micrographs of machined surface. (R_a is measured by the contact stylus profilometer).

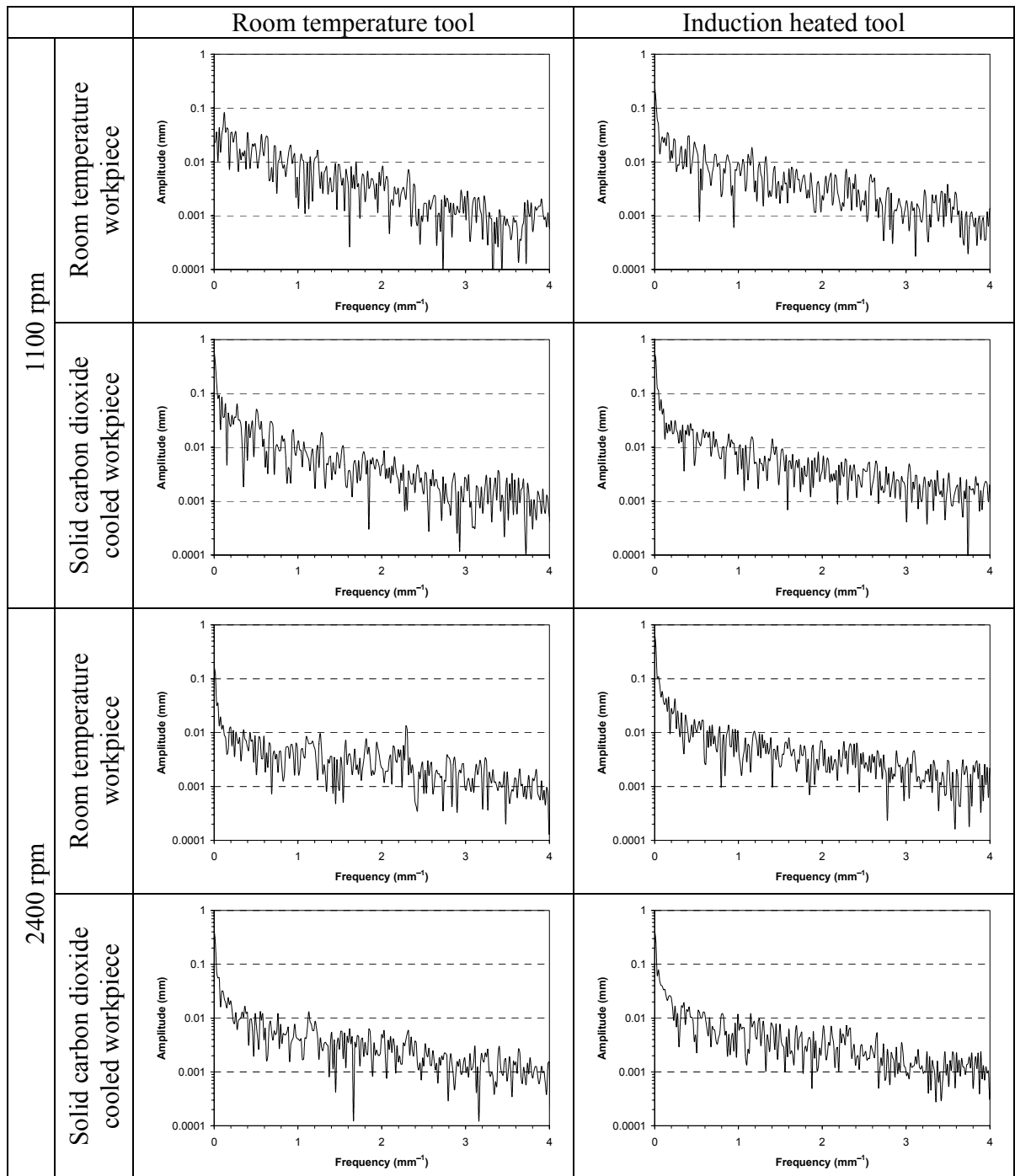


Fig. 5.12. Frequency domain analysis of machined elastomer surfaces.

CHAPTER 6.

CONCLUSIONS AND FUTURE WORK

6.1. Conclusions

In this study, the use of sharp tools, cryogenic cooling of workpiece, and induction heating of the tool for machining of elastomers was investigated. The chip formation, inverse heat transfer solution of induction heating, induction-heated tool for elastomer machining, forces in end milling of elastomers, and machined grooves and surfaces were studied.

A classification system that identifies elastomer chips based on their size and morphology was described. Optical pictures and SEM micrographs were used to examine and classify chips. A four-step procedure was developed and applied to classify the seven types of chips. Serrated chip formation with apparent adiabatic shear bands was observed for one end milling condition. The low thermal conductivity of elastomer was a possible cause for the observed shear band formation. Another type of serrated chip was found with surface wavy marks due to vibration of the workpiece.

In the study of inverse heat transfer solution of induction heating, the explicit finite difference formulation was developed to calculate the surface heat flux generated by induction of a long workpiece with low cross-section Biot number. Experiments of induction heating of a carbon steel rod were carried out. Measured temperature data provided not only the input for inverse heat transfer solution but also the validation of the finite difference model. The finite difference method and thermocouple temperature measurements were applied to estimate the induction heat flux and workpiece temperature. Compared to measured temperatures, the accuracy and limitation of proposed method was demonstrated. The finite element analysis showed significant difference in temperature variation in the cross-section during heating and also

demonstrated the feasibility to use a single nodal temperature to represent the average cross-section temperature in finite difference modeling. Sensitivity to the grid spacing, thermocouple location, and thermophysical properties were also studied.

Experiments and finite difference modeling of the induction-heated tool were studied. Three sets of experiments were designed to calibrate the contact thermocouple for the tool tip temperature measurement, study the effect of tool rotational speed on induction heat generation and convective heat transfer, and measure the tool temperature distribution for finite difference inverse heat transfer solution and validation of modeling results. A calibration line between temperatures measured by the cement-on and contact thermocouples was established. Tool rotation was illustrated to have insignificant effect on induction heat generation and convective heat transfer at spindle speed lower than 2000 rpm. A finite difference thermal model of the tool and insulator was developed to predict the distribution of tool temperature. The thermal model of a stationary tool could be expanded to predict the temperature distribution of an induction-heated rotary tool within a specific spindle speed range. Experimental measurements validated that the thermal model can accurately predict tool tip peak temperature.

The induction-heated tool and cryogenically cooled workpiece were investigated for end milling of elastomers to generate desirable shape and surface roughness. Effects of cutting speed, tool heating, and workpiece cooling on machining of elastomers were studied. Cutting speed was demonstrated to be critical. At high cutting speed, smoke was generated and became environmentally hazardous. At low cutting speed, the surface roughness was high and material removal was not effective, which resulted the narrow groove width in end milling. Induction-heated tool, if properly utilized, demonstrated to be beneficial for the precision machining of elastomer at low cutting speed with better surface roughness and dimensional control. The low stiffness of elastomer workpiece significantly affected the surface quality. Frequency analysis of cutting forces showed that, even using specially designed fixture to enclose every end milling cut, the low elastic modulus of elastomer inherently generated a 7 Hz low frequency vibration during machining. The low frequency workpiece vibration influenced the distance between major machining marks.

The study only demonstrates the ideas for effective machining of elastomers. Detailed information on the selection of process parameters for a specific material requires extensive experimental work and is beyond the scope of this study.

6.2. Future works

This research has identified the need for future studies in following four areas.

1. Precision machining of elastomer workpiece: In the elastomer machining tests conducted in this research, the relatively small width of machined grooves, about 68 to 78% of the tool diameter, showed the difficulty to achieve good dimensional control of the elastomer workpiece. Induction-heated tool can achieve some improvement but is still not adequate for precise dimensional control. Novel methods need to be developed to further advance the elastomer machining technology and application.
2. Specific energy input and heat transfer during machining: Visible smoke was generated at high spindle speed (2400 rpm). The criterion for the generation of smoke can be studied by investigating the specific energy input to elastomer chips and heat transfer between the tool and workpiece. With this criterion, feasible cutting condition can be selected for elastomer machining without smoke generated.
3. Roughness measurement methods for machined elastomer surfaces: In this research, quantitative comparison of both contact stylus profilometer and non-contact confocal microscopy roughness measurements on machined elastomer surfaces were conducted. Both methods showed their limitations. The deformation of the fine surface features of elastomer using contact stylus resulted in lower R_a values compared to most of the confocal microscope measurements. Burrs on surface could block the view of confocal microscope to reach the bottom of valley. Low surface reflectivity inside the valley was also a problem. This research showed that the surface inspection of elastomers is still a technically challenging problem and requires further research.

4. New materials for machining: The machining methods developed in this research can be applied for biomaterial materials, such as polymers and tissues for medical applications.